MASTER

Development and analysis of a µPIV system

Olieslagers, R.

Award date:
2006

Development and Analysis of a μPIV system

Student: R. Olieslagers
Supervisors: dr. ir. A.J.H. Frijns, ing. P.R Bloemen
Date: 10-Nov-2006
Report number: WET 2006.27

Technische Universiteit Eindhoven
Department of Mechanical Engineering
Division Thermo Fluids Engineering

Summary

As a result of the ever increasing demand for higher performance in modern micro electronics, the need arises for new cooling solutions to cope with the corresponding increase of heat generation. One of the optional cooling techniques, are microchannels in which a micro flow dissipates heat away from the electronic component. In order to optimize the heat transfer in the microchannel, understanding of the micro fluid phenomena is necessary. To visualize and study the micro fluid phenomena in a microchannel, a μPIV system is needed.

A μPIV system based on fluorescence microscopy is developed. This μPIV system is able to measure flow fields with a maximum velocity of 3.6 m/sec and a spatial resolution of 7.36x7.36x18 μm. In order to visualize the motion of the micro flow, fluorescent tracer particles with a peak sensitivity of 532 nm and peak emission of 612 nm are seeded in the flow. The μPIV system is designed to image a particle of 0.86 μm by 4 pixels. As a result of the low fluorescence intensity of the 0.86 μm particle, particles with a diameter of 2 μm are used. The use of particles with a diameter of 2 μm, results in particle images that are clearly recognizable over the electronic noise of the camera.

The analysis of the μPIV system showed that the visualization and illumination can be improved, by choosing a dichroic mirror with a higher reflectivity at the wavelength of the laser light and higher transmissivity at the wavelength of the fluorescent light. Furthermore it is possible to enhance the particle image quality, by using a camera with a higher quantum efficiency. Possible optical error sources such as, field curvature, pincushion and barrel distortion, vignetting are not present. With respect to the flow properties of the tracer particles is determined that the buoyancy force and Saffman lift force introduce velocities which are negligible compared to the mean velocity of the fluid flow. The time constant of the particle to a step in fluid velocity is of the order 10^{-7} sec.

The thermal analysis of the laser on a timescale of 1000 seconds, shows that the temperature of the microchannel device increases with 10K. By means of a numerical model is determined that a laserpulse of 5 nsec with an energy of 16 mJ results in a temperature peak of the order 1000 K in the first 6 μm of the microchannel device. When the illumination path of the μPIV system is optimized and the microchannel device gets illuminated by laserpulse of 16 mJ, it is most likely that the microchannel device gets damaged by the high temperature.
The velocity measurement in a straight microchannel and sinusoidal microchannel, show that the measured velocity field matches well with the analytic or numerical determined velocity field. However in the region near the microchannel wall, the velocity profiles deviate as a result of low visibility of the particles in this area and interrogation windows which overlap an area outside the microchannel device with no particles.

Samenvatting

Om het toenemend energie verbruik en daardoor steeds hogere warmte productie in de micro elektronica te reguleren zijn alternatieve methoden noodzakelijk om elektronische componenten te koelen. Een van de nieuwe methoden om deze elektronische componenten te koelen, zijn microkanalen. In deze microkanalen wordt een vloeistof stroming gegenereerd om de warmte weg te voeren van het elektronisch component. Ter optimalisatie van de koel capaciteit van deze microkanalen, is kennis van het gedrag van deze microstroming noodzakelijk. Om deze microstroming te kunnen visualiseren en uiteindelijk te bestuderen, moet een μPIV opstelling worden ontworpen.

Een μPIV-opstelling op basis van de fluorescentie technologie is ontworpen. Aan de hand van deze opstelling is het mogelijk om complete snelheidsvelden te meten met een maximale snelheid van 3.6 m/sec en een resolutie van 7.36x7.36x18 μm. Om de vloeistof stroom te visualiseren, zijn fluorescente deeltjes gebruikt met een piekgevoeligheid bij een golflengte van 532 nm en piekemissie bij een golflengte van 612 nm. De opstelling is zo ontworpen, dat een deeltje met een diameter van 0.86 μm wordt afgebeeld op 4 pixels. Door de lage fluorescentie intensiteit van een deeltje met een diameter van 0.86 μm, is gekozen om deeltjes met een diameter van 2 μm toe te passen. Als gevolg van de grotere deeltjes diameter, is de grijswaarde van het deeltje op de CCD gestegen en daardoor duidelijk te herkennen boven the elektronische ruis van de camera.

Uit de analyse van het μPIV is geconcludeerd dat het visualisatie en belichtingsdeel van de opstelling kan worden verbeterd, door een dichroitische spiegel te gebruiken die een groter deel van het laser licht reflecteert en groter deel van het fluorescente licht doorlaat. Verder kan het visualisatie deel verbeterd worden, door een camera toe te passen met een hogere licht gevoeligheid. Mogelijke optische fouten, zoals kromming van het focus vlak, positieve en negatieve beeld vervorming en "vignetting" zijn niet aanwezig. Uit een analyse naar de stromings eigenschappen van een deeltje komt naar voren dat de zwaartekracht en Saffman liftkracht een snelheid induceren, die verwaarloosbaar is vergeleken met de gemiddelde snelheid van de vloeistof. De tijd constante van een deeltje als reactie op een stap in de snelheid van de vloeistof stroming is 10^{-7} sec.

Aan de hand van een thermische analyse op een tijd schaal van 1000 seconden is bepaald, dat de temperatuur van het microkanaal maximaal met 10 K stijgt. Door middel van een numeriek model is aangetoond dat een laserpuls van 5 nsec en een energie van 16 mJ, een temperatuur stijging groter dan 1000 K kan veroorzaken. Indien de belichting van de huidige opstelling wordt geoptimaliseerd en uiteindelijk wordt belicht met laserpuls van 16 mJ, is het zeer waarschijnlijk dat het microkanaal beschadigt raakt door de hoge piek temperatuur.

Zowel een snelheidsmeting in een recht als sinusvormig kanaal tonen aan dat het gemeten snelheidsprofiel goed overeenkomt met analytisch en numeriek voorspelde snelheidsprofielen. Echter in het gebied kort bij de wand van het microkanaal is een afwijking tussen het gemeten en numeriek of analytisch bepaalde snelheidsprofiel waarneembaar. Deze afwijking wordt veroorzaakt door de slecht zichtbare deeltjes bij de wand en interrogatie gebieden die een deel buiten het microkanaal zonder deeltjes overlappen.

Acknowledgements

This thesis represents the study carried out during the graduation period of the master track "Mechanical Engineering". The graduation project is performed within the division Thermal Fluids Engineering at the Technical University of Eindhoven.
First of all I would like to thank Arjan Frijns and Paul bloemen for their supervision, answers to all different kind of questions, for keeping me on track and corrections to this thesis. Furthermore I would like to thank Geert Jan van Hoek and Henri Vliegen, for fabricating experimental parts which I needed to perform my experiments successfully. I would also like thank Eric Homburg for the delivered calibration sample and his advice to fabricate a sinusoidal microchannel device, Vincent Tiesinga for his help with numerical work and Jan Hasker for his help on computer and IT related issues.

Contents

Summary i

Samenvatting ii

Acknowledgements iv

1 Introduction 1
- 1.1 Project description . . . 2
- 1.2 Outline thesis . . . 2

2 Particle velocimetry 3
- 2.1 Introduction . . . 3
- 2.2 Theory μPIV . . . 3
- 2.3 Experimental set up . . . 5
- 2.4 Properties of the experimental set up . . . 6
  - 2.4.1 Requirements to perform μPIV . . . 6
  - 2.4.2 Particle image diameter . . . 7
  - 2.4.3 In plane resolution . . . 7
  - 2.4.4 Out of plane resolution . . . 8
  - 2.4.5 Dynamic range . . . 9
  - 2.4.6 Maximum unrestricted measurement depth . . . 9
- 2.5 Processing of particle images . . . 10
  - 2.5.1 Preprocessing . . . 10
  - 2.5.2 Cross correlation . . . 11
  - 2.5.3 Mapping procedure . . . 12

3 Analysis of the μPIV set up 13
- 3.1 Introduction . . . 13
- 3.2 Flow properties of the particle . . . 13
  - 3.2.1 Response time of a particle . . . 14
  - 3.2.2 Influence gravity . . . 14
  - 3.2.3 Influence lift force . . . 14
- 3.3 Illumination of the particle . . . 15
  - 3.3.1 Diffusor . . . 15
  - 3.3.2 Reflectivity dichroic mirror . . . 16
  - 3.3.3 Reflection at the particle boundary . . . 16
  - 3.3.4 Inhomogeneous illumination . . . 18

3.4 Visualization of the particle . . . 18
3.4.1 Influence particle diameter . . . 18
3.4.2 Transmission long pass filter and dichroic mirror . . . 19
3.4.3 Camera . . . 20
3.4.4 Particle visibility . . . 20
3.4.5 Distortion and magnification . . . 21
3.5 Conclusions . . . 22

4 Thermal analysis of the pulsating laser 23
4.1 Introduction . . . 23
4.2 Temporal radiation regimes . . . 23
4.3 Absorbance of laser intensity by matter . . . 24
4.4 Exponential temperature increase . . . 25
4.4.1 Temporal radiation regime . . . 26
4.4.2 Temperature measurement . . . 26
4.4.3 Numerical model of exponential temperature increase . . . 27
4.4.4 Results . . . 29
4.5 Temperature increase during laserpulse cycle . . . 30
4.5.1 Temporal radiation regime . . . 30
4.5.2 Negligible conduction model . . . 31
4.5.3 Transient 2D axis symmetric model . . . 32
4.5.4 Results . . . 33

5 Experiments 37
5.1 Introduction . . . 37
5.2 Flow regime . . . 37
5.3 Micro flow in a rectangular channel . . . 38
5.3.1 Analytic solution . . . 38
5.3.2 Measurement method . . . 38
5.3.3 Experimental results . . . 39
5.4 Micro Flow in a sinusoidal channel . . . 44
5.4.1 Numerical model . . . 44
5.4.2 Measurement method . . . 45
5.4.3 Results . . . 46
5.5 Conclusions . . . 50

6 Conclusions and Recommendations 51
6.1 Conclusions . . . 51
6.2 Recommendations . . . 52

Bibliography 53

A Tables 55

B List of Symbols 57

C PIV and PTV 60

D Specifications experimental components **62**
D.1 Laser pulse and camera sequence 62
D.2 Positioning system 63
D.3 Seeding 64
D.4 Calibration grid 65

E Particle image diameter and out of plane resolution **66**
E.1 Derivation 66

F Influence preprocess techniques **70**
F.1 Effect dynamic threshold and contrast enhancement 70

G Visibility **72**

H Optical analysis **74**
H.1 Refraction 74
H.2 Vignetting 75
H.3 Perspective error 75
H.4 Positive and negative image distortion 76

I Macro- to Microscale Heat Transfer **77**
I.1 Introduction 77
I.2 Lagging behavior 78
I.3 Temperature solutions for the different models 79
I.3.1 Spatial temperature distribution 79
I.3.2 Transient temperature solutions 80
I.4 Discussion 82

Chapter 1

Introduction

Over the past decade there has been increasing interest in understanding the fluid phenomena at the micrometer and nanometer length scale. The understanding of these micro fluid phenomena is important in a variety of research area, such as inkjet printers, micro chemical reactors, microchannels, flow of blood cells in capillary blood vessels. In order to investigate the micro fluid phenomena, a whole velocity field on micro scale has to be measured.

The PIV technique is a well established technique to measure velocity fields, but is limited to spatial resolutions of 0.2 to 1 millimeters. Micron resolution Particle Image Velocimetry [μPIV], uses the PIV technique to measure velocity fields on typical length scales of 100 microns and a spatial resolution of 1-10 microns. In the μPIV research, emphasis is placed on the development of an accurate and reliable velocity measurement method with a micron spatial resolution. In order to achieve micro scale velocity measurements, special recording and optical equipment, micro fluorescent particles and PIV software is developed.

Before μPIV was established, most experiments on micro scale were performed outside the microdevice. In these days the experiments consist of bulk flow measurements, such as flow rate and pressure drop measurements. The earliest work of using flow tracing particles to estimate the velocity field on micro scale was reported by Brody (1996). He used a mercury lamp to continuously illuminate 0.9 μm particles. The length of the particle streaks were used to measure the local velocity. Santiago et al. (1998) performed the first reported experiment, where the PIV technique was used to measure the whole velocity field on micro scale. A mercury lamp was used to continuously illuminate the 300 nm fluorescent particles. A shutter mechanism with an intensified camera were used to record particle images. The μPIV technique was extended further by Meinhart et al. (1999). Meinhart used a pulsed ND:YAG laser with a pulse width of 5 nsec to illuminate fluorescent particles with a diameter of 200 nm. The use of a pulsed light source resulted in the possibility to measure much higher velocity's and record smaller particles.

1.1 Project description

In the near future, electronic devices will produce more heat as a result of increasing demands. New appropriate cooling techniques are needed to guarantee high performance during a long life span. One of the optional cooling techniques are microchannels, in which a micro flow is generated that dissipates heat away from the electronic component. In order to optimize the cooling capacity of these microchannels, understanding of the micro fluid phenomena is necessary.
This thesis is about the development and analysis of a μPIV system to measure micro flow fields in microchannels. Regarding the development of a μPIV system, several aspects with respect to the illumination and visualization of the micro particles have to be solved. Some examples are, removal of interference and background light, alignment of the laser illumination with the optical visualization path, positioning of the microchannel device with high accuracy. Furthermore it is important to determine the specific properties of the developed μPIV system. Beside the development of the μPIV system, an analysis of the experimental components is required for further improvement of the μPIV system. Several aspects that have to be analyzed, are flow properties of the particle, homogeneity of the laser illumination, loss of fluorescence and laser light along the optical path, thermal influence of the pulsating laser. Accuracy and reliability of the μPIV system has to be studied, by comparing the measured velocity field with a well known analytic or numerical determined solution to a flow problem.

1.2 Outline thesis

This thesis includes a step by step approach of the design, analysis and first accuracy tests on the established μPIV system. In chapter 2, the development of the μPIV system is described. Attention is given to μPIV theory used to measure and calculate velocity fields, the design of the experimental setup with the function of the different components, expected properties such as spatial resolution and dynamic range. In chapter 3, the μPIV experiment consisting of fluorescent tracer particles, optics and recording equipment is analyzed. The optimization of the experimental set up is described and recommendations for further improvement are given. In chapter 4, the thermal analysis to determine the influence of the high intensive laser on the temperature of the microchannel device is described. A distinction is made between the exponential temperature increase of the microchannel device on a timescale of the order 1000 seconds and the temperature peaks during a laser pulse cycle. Chapter 5 is about the experiments performed to determine the accuracy and reliability of the μPIV system. The velocity field of a rectangular and sinusoidal microchannel determined by μPIV experiment, are compared to an analytic and numerical solution respectively. Finally chapter 6, gives the conclusions of this research and recommendations for future research.

Chapter 2

Particle velocimetry

2.1 Introduction

In this chapter, the process to determine the velocity field inside the microchannel device is described. First of all the principle of PIV and volume illumination, is discussed in section 2.2. Subsequently the experimental set up and the different components are explained in section 2.3. The properties of the experimental set up are calculated in section 2.4. Finally in section 2.5, information is given about the algorithm to calculate velocity vectors and techniques to enhance the particle images.

2.2 Theory μPIV

The μPIV technology, refers to the application of PIV on a length scale of 100 microns. The technique PIV is based on the recording of two successive images of flow tracing particles which accurately follow the motion of the flow. These images at time step t and t' are divided into sectors, the so called interrogation windows (figure2.1(a)). Over the particles located inside an interrogation window is determined the mean displacement, by means of cross correlation (see section 2.5.2). By taking the coefficient of the mean particle displacement and the time delay between two images, is calculated the mean velocity. This mean velocity is represented as a velocity vector at the center of the interrogation window. In order to illuminate and record two successive images with a very short time delay, a special PIV-laser (ND:YAG) and camera (Kodak Mega Plus ES1.0) are used. The exposure time of the camera and the puls signal of the laser related to the time, are presented in figure 2.1(b). The frequency by which an image pair can be recorded, is limited to the maximum frequency of the laser (15 Hz). The width of a laserpulse is 5 nsec and the time delay between two successive images (dt_{delay}) can be set to a minimum of 1 μsec. Due to this small time delay, the PIV technique is most suited to perform measurements with a high dynamic range when the mean physical particle displacement is of the order μm (appendix C).

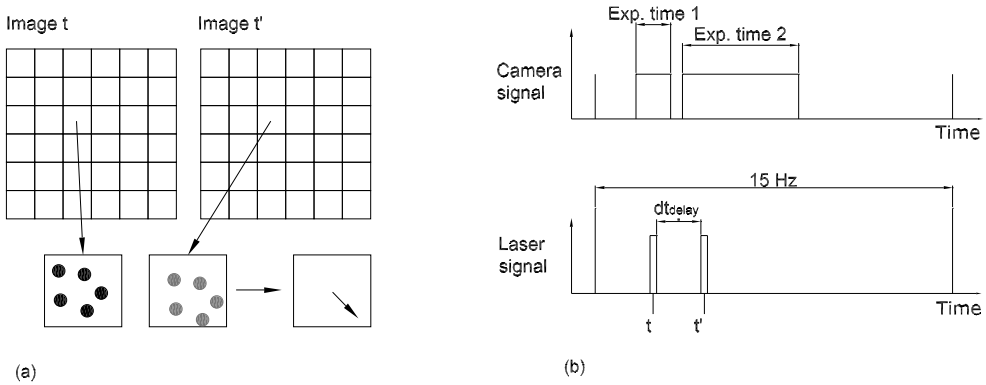

Figure 2.1: Camera and laser signal in time, in order to record two successive images at t and t' (a) (appendix D.1). Overview of an image pair each divided into interrogation windows, where a mean velocity vector is calculated at each interrogation window center (b).

Regarding the illumination of the particles, μPIV differs from conventional velocimetry measurement techniques. With the conventional particle measurement techniques, the particles are illuminated by means of a laser sheet. The particles which flow within the thickness of the laser sheet are recorded by a camera aligned perpendicular to the laser sheet (appendix C). Due to the small length scale of the microchannels it is almost impossible to form a laser sheet of a couple of microns thick and even more difficult to align the sheet with the object plane of an objective. Also optical acces from the side of the microchannel is most of the time not possible. Because of these reasons, volume illumination is applied instead of a laser sheet (see figure 2.2).

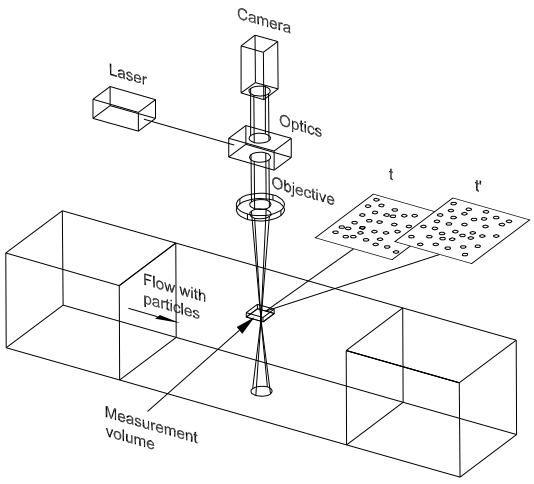

Figure 2.2: Typical experimental set up to perform μPIV in a microchannel.

The particles flowing in the measurement volume are illuminated by the laser and imaged by the camera from the same direction. To remove background light and reflected light from the microchannel geometry, particles in the microchannel geometry are commonly imaged by fluorescence microscopy instead of scattering. The principle of fluorescent microcopy and the optical technique used to record particles flowing in the measurement volume is explained in section 2.3.

2.3 Experimental set up

In order to visualize the microflow inside the microchannel device, fluorescent particles (R200, Duke Scientific) are seeded in the fluid. These fluorescent particles have a peak sensitivity and peak emission at a wavelength of 542 nm and 612 nm respectively. For the emission and excitation spectra of the fluorescent particles is referred to appendix D.3. These fluorescent particles are illuminated and visualized by the developed μPIV system. By means of a schematic overview of the experimental set up is explained the function of each component (figure 2.3).

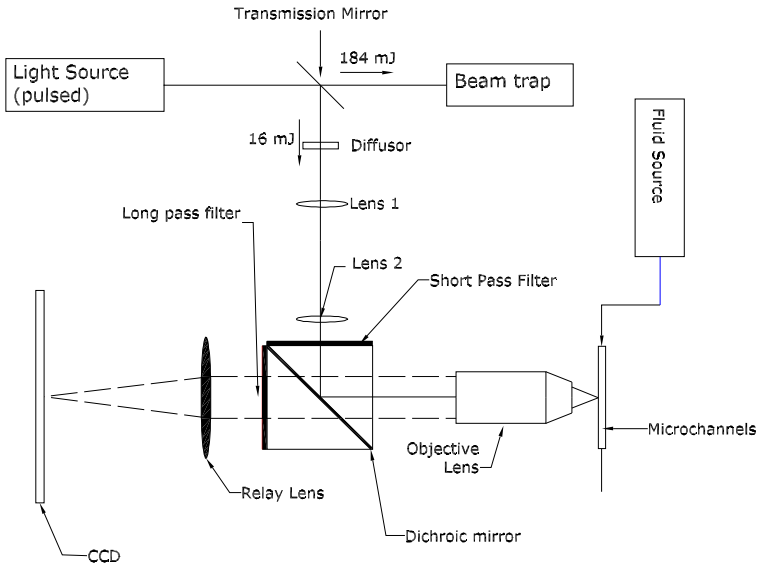

Figure 2.3: Experimental set up to illuminate and visualize the fluorescent micro particles seeded in the fluid flowing through the microchannel device. The solid line depicts the path of the laser light [532 nm] by which the micro particles are illuminated. The dashed line depicts the path of the red fluorescent light [612 nm] emitted from the fluorescent micro particles .

The fluorescent particles are illuminated by a pulsed monochromatic laser beam with a wavelength of 532 nm. The pulse signal related to time is given by figure 2.1 (a). This laser beam is reduced in energy from 200 to 16 mJ per pulse by a 92 % transmission mirror (078-0160, Molenaar optics), to prevent over-illumination of the seeding particles and damaging of the beam-forming optics. The resulting beam with an energy of 16 mJ per pulse is passed through a diffusor (DG-10-600, Thorlabs), which disturbs the monochromatic light of 532 nm to prevent interference due to monochromatic light rays traveling in opposite direction. Next the laser beam passes lens 1 and lens 2 and a short pass filter (FES0550, Thorlabs), which only allows wave lengths up to 550 nm to pass. The transmitted beam is reflected by a dichroic mirror (C1720MP02, Molenaar optics) in the direction of the objective (Zeiss LD 20x), which finally illuminates the fluorescent particles inside the micro fluid device. The red light emitted by particles which flow in the object plane of the objective lens, is delivered in the form of a parallel beam to the relay lens (Zeiss). This relay lens focusses the fluorescent light on the CCD. This CCD chip consists of an array of cells (pixels), which transform the absorbed light to an electric signal. For a 8 bit image the electric signal is scaled to 255 values, the so called

gray values. From these pixels with each a certain gray value the total image is build up. A long pass filter (FEL0550, Thorlabs) is positioned between the relay lens and the dichroic mirror, to prevent reflected green light and background light reach the CCD. The long pass filter only allows wavelengths above 550 nm to pass through.
A top view and cross section of the microchannel device in which the movement of tracer particles is recorded, is given in figure 2.4.

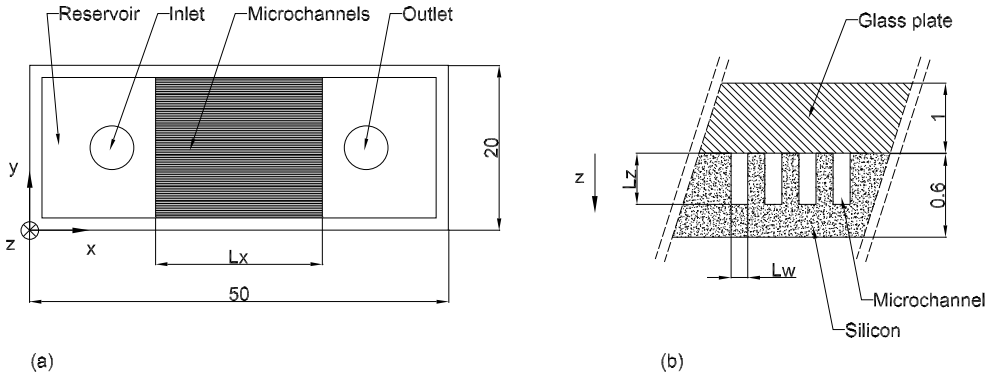

Figure 2.4: Top view (a) and cross section (b) of the microchannel device in mm.

The microchannel device consist of a silicon substrate with on top a glass plate, with a thickness of 600 μm and 1 mm respectively. In the silicon substrate an array of 75 microchannels is etched with a spacing of 100 μm between the microchannels. The microchannels have a depth L_z, width L_w and length L_x of 300 μm, 100 μm and 15 mm respectively. The microchannel device can be positioned with an accuracy of 10 μm in x, y direction and 1 μm in z-direction, by micron resolution translation stages (appendix D.2).

2.4 Properties of the experimental set up

In this subsection properties of the experimental set up are presented. The following properties are discussed: the in plane and out of plane spatial resolution, the dynamic range, the particle image diameter and the maximum unrestricted measurement depth. First of all the requirements to achieve successful μPIV measurements are presented. The derivation of the used equations is presented in appendix E.

2.4.1 Requirements to perform μPIV

For μPIV the following requirements must hold to achieve accurate measurements [12]:

- An interrogation window should contain between 4 and 8 particles, to obtain sufficient correlation.
- The in plane particle displacement should be no more than $\frac{1}{4}$ times the size of the interrogation window. Subsequently the out of plane of the particle displacement should be no more than $\frac{1}{4}$ times focal plane thickness [18].

- A minimal particle displacement of 2 pixels is recommended.
- The particle image diameter must be resolved by at least 3-4 pixels.

2.4.2 Particle image diameter

The fluorescent particles with a particle diameter of 0.86 μm are imaged on the CCD by an infinite corrected lens system, see figure 2.5. Fluorescent light from the particles at the left side passes subsequently water, glass and air and is finally imaged on the CCD. By the analysis in section H.1 is determined, that refraction due to different intermediate media has no influence on the magnification. The magnification for an infinite lens system can be calculated by taking the coefficient of the image focal distance [F_i] and object focal distance [F_o].

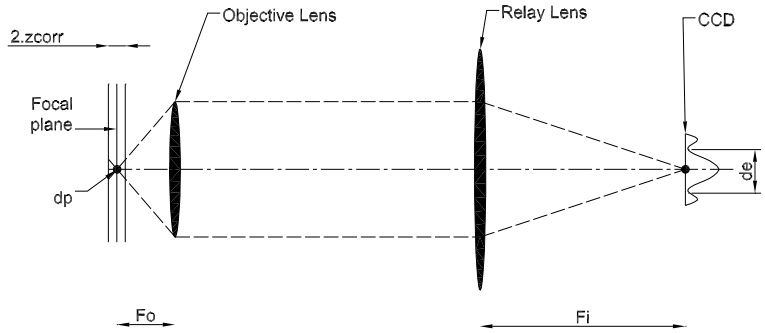

Figure 2.5: Schematic of the infinity corrected lens system, used to image the particles with a diameter of 0.86 μm on the CCD.

For the calculation of the in focus particle image diameter d_{e_∞} equation (2.1) is used, which is derived in appendix E. The values for the variables are presented in table A.3.

$$d_{e_\infty} = [1.49M^2\lambda^2((\frac{n_{air}}{NA})^2 - 1) + M^2 d_p^2]^{\frac{1}{2}} \quad = \quad 38.3\mu m \tag{2.1}$$

Where M is the magnification, λ the wavelength, n_{air} the refractive index of air, NA the numerical aperture, d_p the particle diameter. By dividing d_{e_∞} through the pixel size (9μm), is calculated that the particle image diameter d_{e_∞} is imaged on 4 pixels.

2.4.3 In plane resolution

The in plane resolution is determined by the physical dimensions of an interrogation window. To detect 4 to 8 particles inside an interrogation window, a window of 32x32 pixels is appropriate. The field of view (fov) of the experimental set up, is calculated by equation (2.2).

$$\text{fov} = \frac{\text{CCD area}}{M} = 450\text{x}450\ \mu\text{m} \tag{2.2}$$

The physical dimensions of an interrogation can be calculated according to equation (2.3).

$$\text{interrogation window} = \frac{32 \text{ pixels}}{1000 \text{ pixels}} \text{fov} = 14.4\text{x}14.4 \ \mu\text{m} \tag{2.3}$$

A window overlap of 50 % can be used, to obtain a higher spatial resolution. With an overlap of 50 %, the spatial resolution increases to 7.2x7.2 μm. Which means that 14 vectors are calculated along the width of a microchannel (100 μm).

2.4.4 Out of plane resolution

In figure 2.6 a schematic view is given of the volume illumination of a microchannel. Where L_z is the height of the microchannel, z_a the axial distance of an out of focus particle to the object plane and δ the thickness of the object plane.

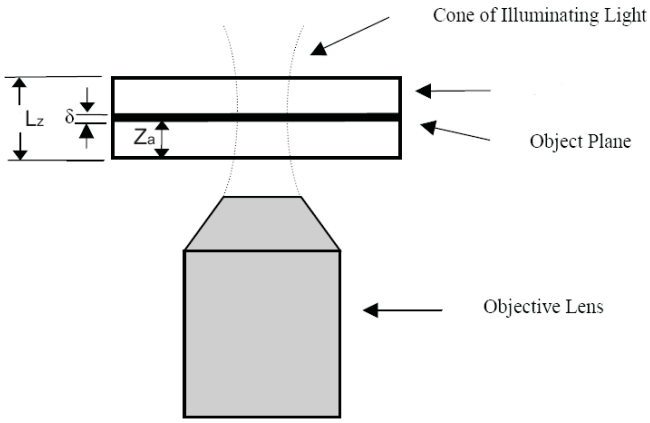

Figure 2.6: Schematic showing the volume illumination of a microchannel. The particles located within δ, flow in the object plane of the objective lens.

The particles within the thickness of the object plane δ, are sufficient in focus to produce visible images. Due to the geometric spreading, the particle image becomes larger and gets a lower intensity for an increasing axial distance z_a to the object plane. The out of plane resolution can be considered as the distance to the object plane where the particle is sufficient out of focus (z_{corr}) so that it hardly contributes to the signal peak of the correlation function. The relative contribution of an out of focus particle compared to an in focus particle, can be expresses as the coefficient of an in focus particle image diameter $d_{e_{\infty_{of}}}(z_a = 0)$ and an out of focus particle image diameter $d_{e_{\infty_{of}}}(z_a = z_{corr})$ to the forth power

$$\varepsilon = \frac{d_{e_{\infty_{of}}}(z_a = 0)^4}{d_{e_{\infty_{of}}}(z_a = z_{corr})^4} \tag{2.4}$$

Following the analysis of Wereley and Meinhart [23], z_{corr} is calculated for a relative contribution ε of 0.01. This means that a particle is considered out of focus, when the particle image diameter is 3 times larger as an in focus particle image diameter. The correlation depth for

the experimental set up is calculated according to equation (2.5), which is derived in section E.

$$z_{corr} = \frac{1}{2}[\frac{1-\sqrt{\varepsilon}}{\sqrt{\varepsilon}}(\frac{n_{air}^2}{NA^2} - 1)(d_p^2 + 1.49\lambda^2(\frac{n_{air}^2}{NA^2} - 1))]^{1/2} \tag{2.5}$$

The out of plane resolution of the experimental set up is equal to the $2z_{corr}$, which is equal to 13.2 μm. Considering the depth of the microchannel (300 μm), this means that the velocity can be measured at roughly 20 measurement planes .

2.4.5 Dynamic range

Beside the in-plane resolution, also the maximum displacement of a particle between two images is related to the size of the interrogation window. According to G.A.J van de Plas [12], the particle displacement should be no more than $\frac{1}{4}$ times the size of the interrogation window. If the particle displacement becomes higher than $\frac{1}{4}$ times the size of the interrogation window, it is very likely that particles visible in an interrogation window of the first image will no longer be present in a corresponding interrogation window of the second image. The maximum displacement of a particle [L_{max}] between two images is determined by equation (2.6).

$$L_{max} = \frac{1}{4}\text{interrogation window} = 3.6\ \mu\text{m} \tag{2.6}$$

With the help of equation (2.6) and the minimum time delay between two images [dt_{delay}], the maximum velocity in the micro channel [v_{max}] is calculated with equation (2.7).

$$v_{max} = \frac{L_{max}}{dt_{delay}} = 3.6\ \text{m/s} \tag{2.7}$$

According to an earlier study of van Eummelen 2004 [3] on forced internal heat transfer in microchannels, references are found of velocities up to 5.5 m/sec and a pressure head up to 3 bars.

2.4.6 Maximum unrestricted measurement depth

The maximum unrestricted measurement depth (z_{un}), is the maximum depth (z) measured from the top of the microchannel to the object plane where the light from the fluorescent particles is not restricted by the channel geometry. This maximum unrestricted measurement depth is calculated by equation (2.8).

$$z_{un} = \frac{L_w}{2\tan(\theta_{NA})} \tag{2.8}$$

Where L_w is the width of the microchannel, and θ_{NA} the angle of the extreme light ray to the optical axis determined by the numerical aperture of the objective lens. For the objective in

the experimental set up (NA=0.4) and a microchannel with Lw is 100 μm, the z_{un} (158 μm) and θ_{NA} (17.5°) is drawn in figure 2.7 (a). When the measurement depth, z, becomes higher as z_{un}, the extreme light rays from the fluorescent particles are restricted by the microchannel wall. This results in a decrease of the effective NA, because $\theta < \theta_{NA}$ (figure 2.7(b)).

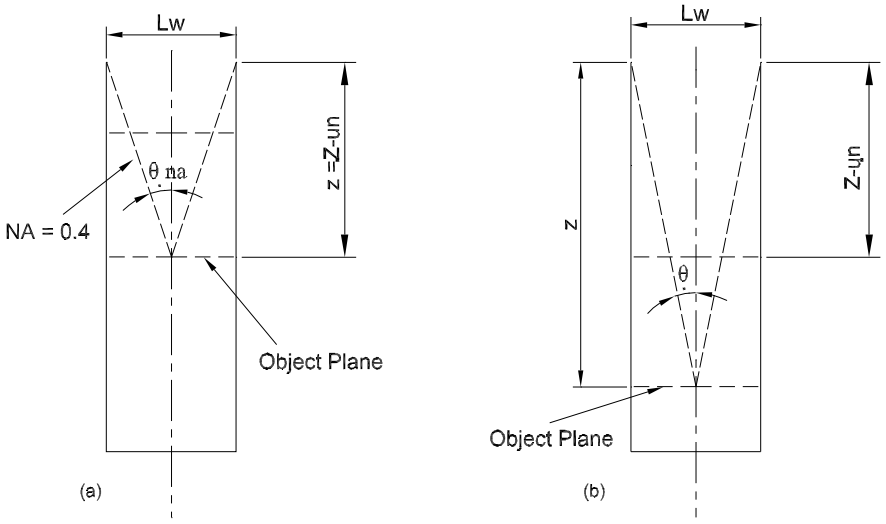

Figure 2.7: Extreme light rays for an object lens with NA=0.4, where z is equal to z_{un} (a). Extreme light ray path for an objective with NA=0.4, where the light rays are restricted by the channel geometry because $z > z_{un}$ (b).

2.5 Processing of particle images

After the particle images are recorded by the experimental set up, the recorded images are processed in order to get a vector field of the microflow. The preprocess techniques, contrast enhancement and dynamic background filtering are discussed in subsection 2.5.1. Subsequently information is given on the cross correlation algorithm and calibration of the experimental set up.

2.5.1 Preprocessing

As a result of the weak fluorescence signal of the particles, it is necessary to enhance the contrast of the particle image. The principle of contrast enhancement is explained by figure 2.8, which is a histogram of an image of 2 μm particles between two microscope glasses. According to the histogram in figure 2.8 (a), the lower (Lb) and upper bound (Ub) gray value is equal to 15 and 35 respectively. Which means that all fluorescent light of the particles and eventual noise is imaged with a gray value between 15 and 35. The particles can be visualized, by scaling the gray values between Lb and Ub to the whole 8 bit domain of 0-255 gray values. The gray values below Lb and above Ub in the original image are set to 0 and 255 respectively. The shape of the particle image is not influenced by contrast enhancement (appendix F.1)

The particle images recorded by the μPIV system, contain a certain level of background intensity due to light from out of focus particles. This level can be lowered, by choosing proper experimental parameters (see section 3.4.4). The background intensity which is still present can be removed by using a filter. One of the optional filters is a dynamic background filter [12]. This filter cuts of the peaks from the non-uniform background without changing the center position of the particle, see figure 2.8 (b). The influence of the background filter on the intensity of a particle is presented in appendix F.2.

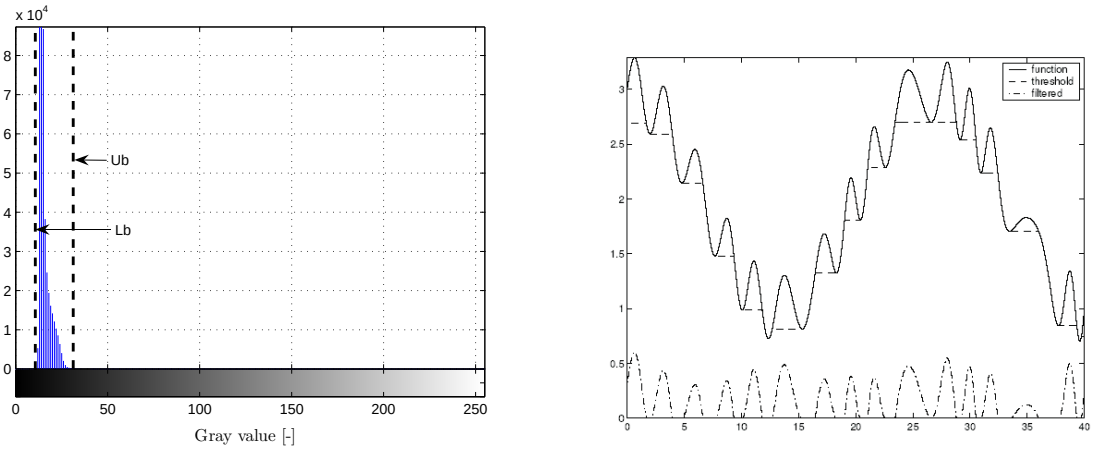

Figure 2.8: Gray value histogram of a 8 bit image with 2 μm particles between two microscope glasses (a). Effect of a dynamic background filter on an image with non uniform background intensity (b) .

2.5.2 Cross correlation

As mentioned in section 2.1, the cross correlation algorithm is used to generate a velocity vector at the center of each interrogation window. The cross correlation function at a certain interrogation spot is usually represented as [23]:

$$\Theta_k(m,n) = \sum_{j=1}^{q}\sum_{i=1}^{p} f_k(i,j)g_k(i+m,j+n) \tag{2.9}$$

Where $\Theta_k(m,n)$ represents the correlation to a certain displacement m and n, $f_k(i,j)$ and $g_k(i,j)$ represent the gray value distribution for the first and second interrogation window, k represents the number of the interrogation pairs with dimensions equal to $p \times q$.
By stepping through every possible displacement in m and n direction, it is possible to calculate the correlation signal corresponding to each displacement m and n, according to equation (2.9). In figure 2.9 an example of a 2D correlation plot is given. Subsequently the position, m_c and n_c, of the maximum correlation value is detected. The maximum value of this correlation value corresponds with the displacement of the particles in the interrogation window. By fitting the pixel gray values around the position m_c and n_c to a Gaussian function, it is possible to determine the sub pixel position of this center. Beside the correlation connected to particle displacement, some random correlations is present. These random correlations are caused by background noise, particles which are illuminated once because they are entering

and leaving the interrogation window and correlation of different particles. Next to the maximum correlation value, the second maximum value is stored. The ratio of the first and second maximum correlation signal, called the detectability [ϵ], gives an indication of the reliability of the displacement data [23].

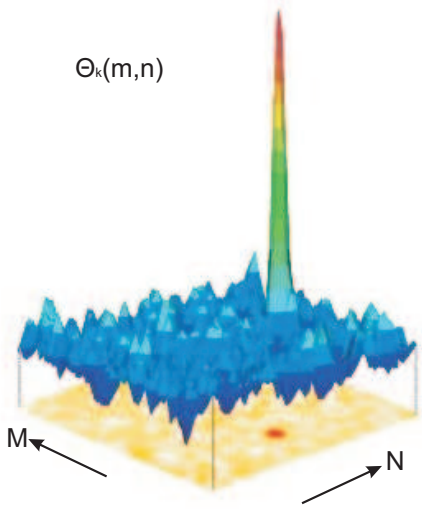

Figure 2.9: 2D cross correlation plot, with the displacement in m and n direction plotted against the correlation signal. [23]

2.5.3 Mapping procedure

The last step to realize a vector field of the micro flow, is mapping from the pixel coordinates ($\underline{x}$) to the physical coordinates ($\underline{X}$). Initially a linear mapping function is used, according to equation (2.10).

$$\underline{\mathrm{X}} = \underline{\mathrm{x}} \frac{\mathrm{fov}}{\mathrm{image\ array}} \tag{2.10}$$

The values for the field of view (fov) and image array are presented in table A.3. When the image is distorted by lens distortions or refraction of intermediate media, a more complex mapping function is needed. The design of a calibration grid which can be used to calibrate an image with a mapping function of the third order is presented in appendix D.4.

Chapter 3

Analysis of the μPIV set up

3.1 Introduction

In this chapter the analysis of the experimental set up and the flow properties of the particles is presented. The flow properties are determined to investigate whether effects as lift and buoyancy forces influence the in plane velocity measurement. The goal of this analysis, is to determine and improve the quality of the recorded particle images. Particle images with a higher quality will result in a more accurate velocity measurement. The analysis of the experimental set up consists of a section in which the illumination and visualization of the experimental set up is examined. Finally in section 3.5, the result of the complete analysis is summarized and some recommendation are given to improve the quality of the particle images.

3.2 Flow properties of the particle

In order to obtain accurate μPIV measurements, the particle must follow the flow accurately. To get an impression of the particle flow characteristics the influence of the buoyancy force, lift force and the respons of a particle to a step in the velocity is calculated. The flow characteristics of the particle are studied, for a stationary Poiseuille flow with only a velocity component in x direction. Neglecting the basset history force (flow is stationair) and added mass force, the motion of the particle is described by the Stokes drag law [18].

$$\mathrm{m_p}\frac{\mathrm{d}\underline{\mathrm{u}}}{\mathrm{dt}} = 3\pi \mathrm{d_p}\mu\{\underline{\mathrm{u}} - \underline{\mathrm{u_p}}\} + (\mathrm{m_p} - \mathrm{m_f})\underline{\mathrm{g}} \tag{3.1}$$

where $\underline{u}$ is the fluid velocity vector, d_p the particle diameter, μ the dynamic viscosity of water, $\underline{\mathrm{u_p}}$ the particle velocity vector, $\mathrm{m_p}$ the mass of the particle, $\mathrm{m_f}$ the mass of fluid displaced by the particle, t the time and g the gravity constant.

3.2.1 Response time of a particle

After injection of a particle in the flowing medium, some time for the particle is needed to flow with the same velocity as the medium. The Stokes drag law in x-direction is solved, to compute the time constant τ of the particle respons.

$$U_p = U(1 - e^{\frac{-t}{\tau}}) \tag{3.2}$$

$$\text{with} \quad \tau = \frac{d_p^2 \rho_p}{18\mu} \tag{3.3}$$

where U_p the velocity of the particle in x-direction, U the velocity of the fluid in x-direction, d_p is the particle diameter, ρ_p the density of the polystyrene particle (1050 kg/m^3). The time constant, τ, for a particle with a diameter of 2 μm is 10^{-7} sec. This response time is small enough for any realistic fluid flow in the microchannel.

3.2.2 Influence gravity

The Stokes drag law in y-direction is used to investigate the influence of gravity on a micro particle, in a stationary uniform flow.

$$(m_p - m_f)\underline{g} - 3\pi\mu d_p V_p = 0 \tag{3.4}$$

For a 2 μm particle with $m_p = 4.4 \cdot 10^{-15}$ kg and $m_f = 4.2 \cdot 10^{-15}$ kg, the particle velocity in y-direction is $1.1 \cdot 10^{-5}$ cm/sec. This velocity is negligible compared to the mean fluid velocity in x-direction (2.5 cm/sec).

3.2.3 Influence lift force

In order the investigate the effect of the lift force on the particle motion an extra term is added to equation 3.2.3, which represents the Saffman lift force on a spherical particle for low Reynolds numbers [10].

$$(m_p - m_f)\underline{g} - 3\pi\mu d_p V_p + \frac{6.36\mu}{4}||\underline{u} - \underline{u_p}||d_p^2\sqrt{\frac{1}{\nu}|\frac{dU}{dy}|} = 0 \tag{3.5}$$

For a Poiseuille flow with a mean velocity of 2.5 cm/sec, the mean velocity gradient between y=0 and y=10 μm is 1365 sec^{-1}. When a particle in this region experiences a relative velocity $|\underline{u} - \underline{u_p}|$ equal to 1 % of the mean velocity in y direction U_{mean}, the Saffman lift force directing to the center of the flow becomes equal to $6 \cdot 10^{-14}$ N. By putting the value of the buoyancy force ($2 \cdot 10^{-15}$N) and Saffman lift force ($6 \cdot 10^{-14}$N) in equation 3.5, the particle velocity in y direction V_p is calculated to be $3 \cdot 10^{-4}$ cm/sec.

3.3 Illumination of the particle

In this section, the intensity decrease along the optical path and the inhomogeneity of the laser illumination is investigated. Therefore a closer look is taken to the light path from the laser source to the illumination of the particles, depicted in figure 2.3. In this section the following components are discussed, the diffusor, the short pass filter, the dichroic mirror and the fluorescent particles. Finally the homogeneity of the laser illumination is investigated by a fluorescent sample.

3.3.1 Diffusor

A diffusor is placed at the start of the optical path to prevent interference. This diffusor transmits light under a range of angles to the optical axes with a certain intensity, see figure 3.1.

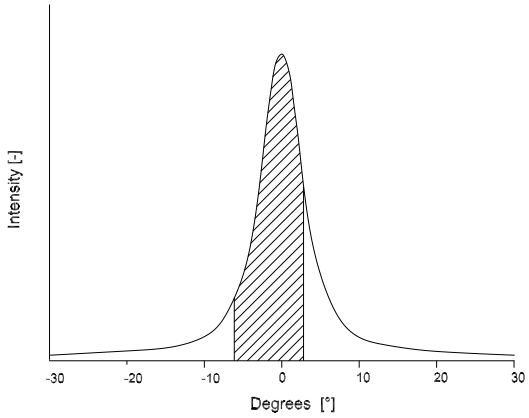

Figure 3.1: Transmitted light intensity behind the diffusor, as function of the angle to the optical axis. The hatched area represents the amount of intensity which is gathered by the optical lens system depicted in figure 3.2

Because the fluorescence intensity of the particles is dependent on the magnitude of the illumination, it is important that most of the light transmitted by the diffusor is gathered by the optical system consisting of lens 1, lens 2 and the objective lens. The schematic position of these lenses is depicted in figure 2.3. By means of the software package "Winlens" the optical path is determined for the used lens configuration, see figure 3.2.

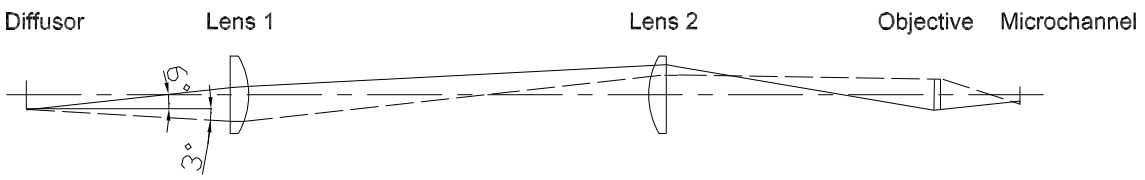

Figure 3.2: Optical path of the extreme light rays at the outside position of the diffusor, with an angle of 6° and 3° to the optical axis.

On the left side the diffusor is drawn with at the boundary the two extreme rays which are just captured and used to illuminate the microchannel device. The angle of these two rays to the optical axis is 3° and 6° for the dashed and solid ray respectively. This means that all laser intensity between the angle 3° en 6° (equal to hatched are in figure 3.1) is captured and used to illuminate the microchannel. By dividing the hatched area through the total area beneath the intensity curve in figure 3.1, is determined that 65 % of the incoming laser light is gathered by the lenses. This is a worst case value, because laser rays that pass the diffusor through the middle are captured over a larger range of angles.

3.3.2 Reflectivity dichroic mirror

Before the laser bundle reaches the microchannel device, it passes subsequently through a dichroic mirror and a low pass filter (figure 2.3). The low pass filter, filters out all wavelengths above 550 nm. The dichroic mirror reflects the green laser bundle into the direction of the microchannels. In figure 3.3 the reflectivity of the dichroic mirror is presented, as function of the wavelength. The reflectivity is determined by a monochromator (ORIEL 77400 Multispec spectograph).

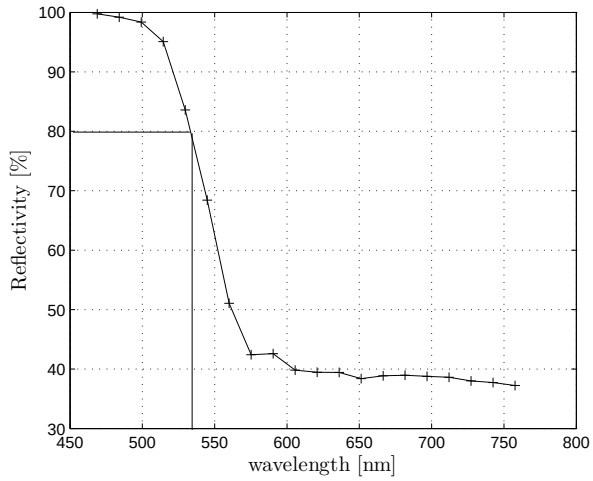

Figure 3.3: Reflectivity of the dichroic mirror as function of the wavelength.

The vertical line drawn in figure 3.3, depicts the reflectivity of the dichroic mirror (80 %) at the wavelength of the laser bundle (532 nm). This means that 20 % of the laser intensity, is transmitted and does not reach the microchannel device. To increase the fluorescence intensity which depends on the illumination intensity, it is recommended to replace the dichroic mirror with a mirror which reflects 100 % of the laser light at a wavelength of 532 nm. According to specification of the dichroic mirror, it has a high reflection at the wavelengths 488 to 532 nm.

3.3.3 Reflection at the particle boundary

Due to the different refractive indices of water ($n_{water} = 1.33$) and the fluorescent particles ($n_{particle} = 1.59$), some laser light is reflected at the boundary of the particles. This reflection of laser light results in a decrease of the fluorescence intensity.

To make an estimation of the average reflection at the particle boundary, the reflection as function of the incident angle [A1] is calculated for 0 to 90 degrees. The incident angle is the angle between perpendicular plane and the laser ray. By Snell's law [6], the refracted angle A2 of the laser ray to the perpendicular plane is calculated (see equation (3.6)).

$$n_{water} \sin(A1) = n_{particle} \sin(A2) \tag{3.6}$$

By means of the angles A1 and A2 and the Fresnel equations for reflection [6], the reflection R $\perp$ and R $||$ as function of the incident angle A1 is calculated (see figure 3.4). Where R $\perp$ and R $||$ stands for the reflection of the electromagnetic light wave with a vector parallel (E_1) and a perpendicular vector (E_2) to the plane of incident.

$$R \perp = \frac{n_{water} \cos(A1) - n_{particle} \cos(A2)}{n_{water} \cos(A1) + n_{particle} \cos(A2)} \tag{3.7}$$

$$R || = \frac{n_{particle} \cos(A1) - n_{water} \cos(A2)}{n_{water} \cos(A2) + n_{particle} \cos(A1)} \tag{3.8}$$

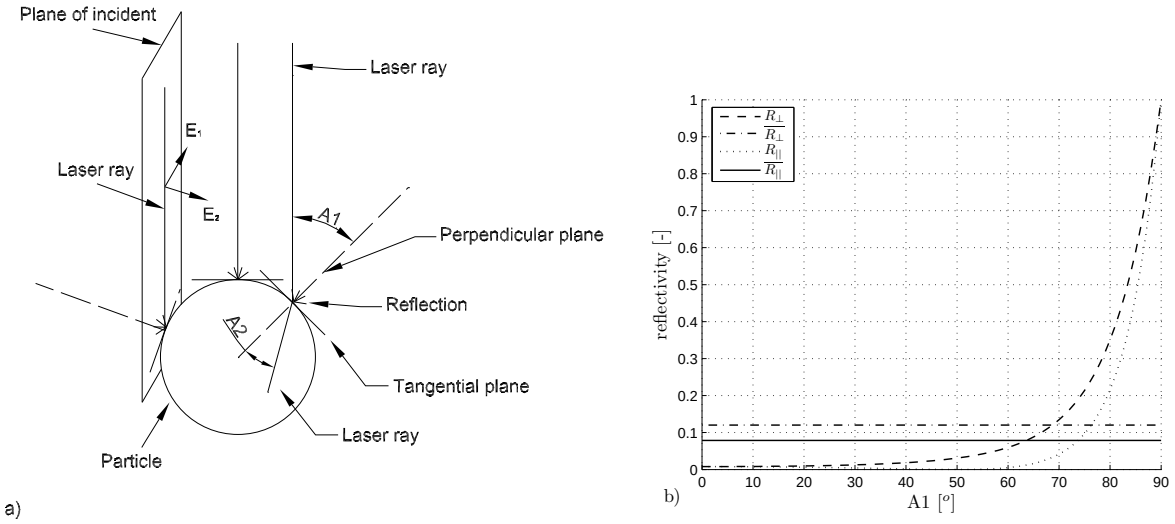

Figure 3.4: Schematic of reflection at the boundary of a particle, depicting the incident angle, perpendicular plane, tangential plane and plane incident of the laser ray a). Reflectivity plot along the boundary of the micro particle for increasing angles of incidence b).

The average reflection for the parallel $[\overline{R\ ||}]$ and perpendicular electromagnetic light wave $[\overline{R \perp}]$, are 8 % and 12 % respectively.

3.3.4 Inhomogeneous illumination

To investigate the illumination distribution, a microscope glass coated with a fluorescent dye (Lumogen Rot 305) is illuminated by the ND:YAG laser. As a result of this laser illumination the fluorescent dye will emit red light. When the intensity of laser bundle is inhomogeneous it will be recognized as an inhomogeneous pixel gray value distribution. Where the pixel gray value (0-255), is a quantity of the absorbed fluorescent light. In figure 3.5 an image of the fluorescent sample is presented, for a inhomogeneous (a) and optimized laser illumination (b). As a result of a decreased distance between the dichroic mirror and the objective (figure 2.3), a homogeneous laser beam distribution is achieved.

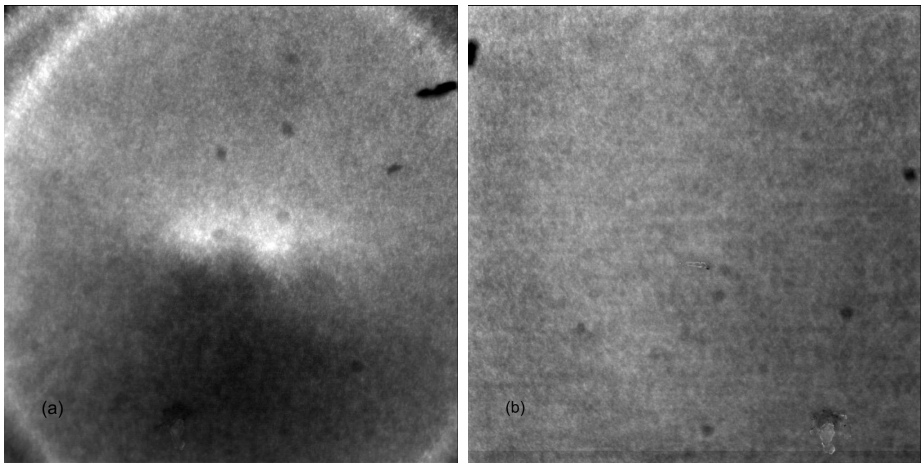

Figure 3.5: Image of the absorbed fluorescent intensity for a first (a) and optimized (b) μPIV illumination.

3.4 Visualization of the particle

In this section the experimental parameters are investigated which influence the quality of the particle image. The quality of the particle image is dependent on several aspects such as, the fluorescence intensity absorbed by the CCD, the quantum efficiency of the camera, the visibility of the particles, the optical quality of the image.

3.4.1 Influence particle diameter

To verify whether the particles generate enough light to become visible over the background noise of the camera, a visualization test is carried out with 0.86 μm and 2 μm particles. The particles lie in a film layer between two microscope glasses which is illuminated by the laser. In figure (a) and (b), the images of the particles with a diameter of 0.86 μm and 2 μm are presented. The contrast is enhanced with an upper and lower bound gray value of 10 and 30 in each image. As is seen from image 3.6, the particle with a diameter of 0.86 μm is hardly resolved over the electronic noise of the camera. The mean gray value of the particle image and electronic noise of the camera are 17 and 14 respectively. This noise is mainly generated by the dark current of the camera. Due to thermal effects, electron hole pairs are generated which can not be distinguished from those generated by the photoelectric effect. When a 2 μm instead of 0.86 μm particle is used, the mean particle image gray value increases from 17

to 22. Unlike the 0.86 μm particles, the particles with a diameter of 2μm can be resolved over the noise of the camera. For the first μPIV tests 2 instead of 0.86 μm particles are used, because of the higher gray value with respect to the electronic noise. The particle with a diameter of 2 μm is imaged on 6 pixels.

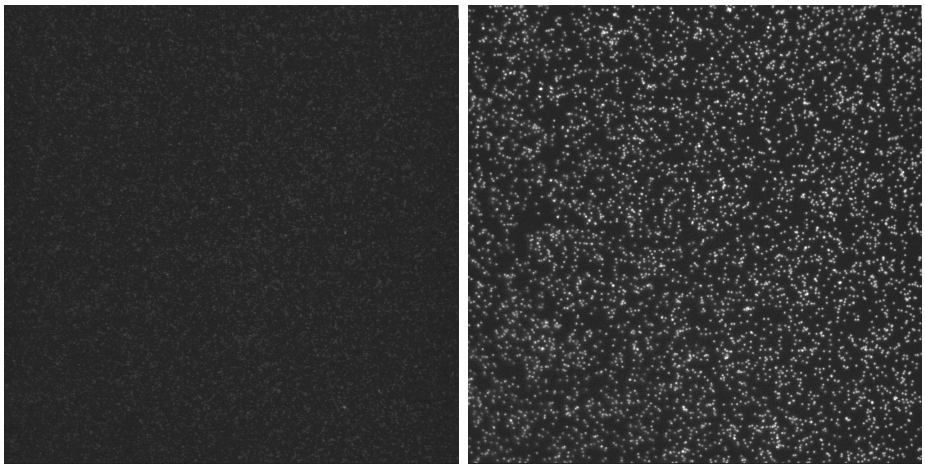

Figure 3.6: Image captured by the experimental set up in figure 2.3, of respectively 0.86 μm (left) and 2 μm particles (right) between two microscope glasses.

3.4.2 Transmission long pass filter and dichroic mirror

Before the emitted fluorescent light with a wavelength of 612 nm reaches the CCD it passes subsequently through a dichroic mirror and a long pass filter. The long pass filter and dichroic mirror filter out all the wavelengths beneath 550 nm, to prevent that background light or reflected green light from the laser reaches the CCD. In figure 3.7 the transmission of the long pass filter and dichroic mirror is presented as function of the wavelength.

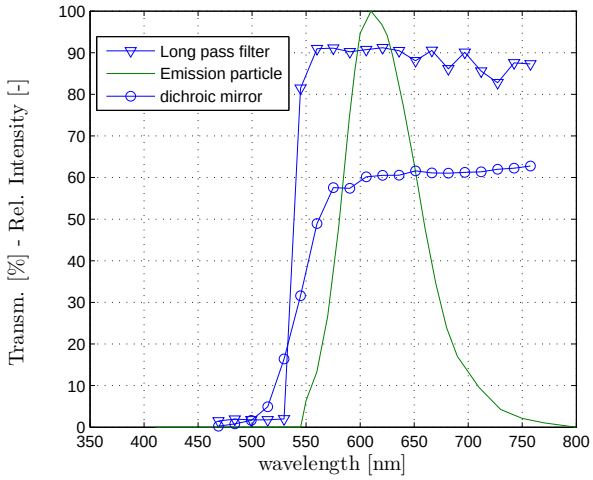

Figure 3.7: Transmission of the dichroic mirror and long pass filter compared with the emission curve of the fluorescent particle as function of the wavelength.

These transmission curves are determined by a monochromator (ORIEL 77400 Multispec spectograph). According to figure 3.7, the transmission ratio of the dichroic mirror and long pass filter is approximately 60 and 90 %, at the peak emission wavelength of the particle (612 nm). According to specification of the dichroic mirror, it has a high transmission at the wavelengths 633 to 830 nm. To increase the quantity of fluorescent light which reaches the CCD, it is recommended to replace the dichroic mirror by a dichroic mirror with a higher transmission ratio at a wavelength of 612 nm.

3.4.3 Camera

The efficiency of the transformation of light intensity to an electric signal for a CCD, is defined as the quantum efficiency. For the Kodak ES 1.0 camera (used during the μPIV experiment), the quantum efficiency at the fluorescence wavelength (612 nm) is equal to 25 % [8]. For fluorescence microscopy with in general low light intensities, special cameras are available with a quantum efficiency near 65 % at a wavelength of 612 nm. The application of a camera with a higher quantum efficiency leads to particle images with a higher gray value. This will result in a better detection of the particle images over the dark current of the camera.

3.4.4 Particle visibility

To obtain high quality velocity data, the μPIV experiment must be designed in such way that particles that flow in the object plane of the objective can be observed over the background light produced by out of focus particles. The ability to observe in focus particles over the background light is determined by the visibility [V]. The visibility is the coefficient of the emitted light intensity of an in focus particle $I(0,0)$ and the background light intensity emitted by out of focus particles I_b [23], see equation (3.9). For the derivation of the equation, see appendix G.8.

$$V = \frac{I(0,0)}{I_b} = \frac{2d_p^3 M^2 \beta^2 (f_o - z)(f_o - z - L_z)}{3V_{fr} L_z f_o^2 (M^2 d_p^2 + 1.49 M^2 \lambda^2 ((\frac{n_{air}}{NA})^2 - 1))} \tag{3.9}$$

With β the parameter which defines the edge of the particle image ($\beta^2 = 3.67$) and z the distance from the top of the microchannel to the object plane. The influence of the following parameters on the visibility is investigated, the numerical aperture NA, the particle volume fraction V_{fr}, the depth of the microchannel L_z and the particle diameter d_p. The investigated parameters are presented in the following dimensionless form

$$NA^* = \frac{NA}{NA_{ref}} \quad ; \quad V_{fr}^* = \frac{V_{fr}}{V_{fr_{ref}}} \quad ; \quad L_z^* = \frac{L_z}{L_{z_{ref}}} \quad ; \quad V^* = \frac{V}{V_{ref}} \quad ; \quad d_p^* = \frac{d_p}{d_{p_{ref}}} \tag{3.10}$$

With the following values for the reference values's, $NA_{ref} = 0.4$, $V_{fr_{ref}} = 0.533$, $L_{z_{ref}} = 150$ μm, $V_{ref} = 1.85$, $d_{p_{ref}}$=2 μm. In figure 3.8 the dimensionless parameters NA^*, V_{fr}^*, d_p^* and L_z^* are plotted against the dimensionless visibility V^*.

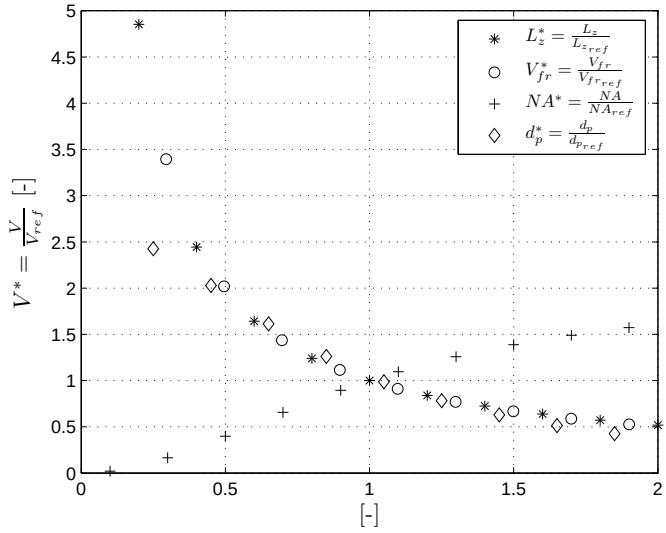

Figure 3.8: Influence of the dimensionless parameters NA^*, V_{fr}^*, L_z^* and d_p^* (horizontal axis) on the dimensionless visibility of an in focus particle (vertical axis).

For a given set of recording optics, the visibility can be increased by decreasing the depth of the microchannel or by decreasing the particle volume fraction. Disadvantage of decreasing the particle volume fraction for a fixed particle diameter, is that the in plane velocity measurement can become less accurate due to interrogation windows with a low particle density. When the particle concentration is fixed, the visibility can be increased by increasing the numerical aperture or by decreasing the particle diameter. Decreasing the particle diameter leads to a lower fluorescence signal of the particle. Therefore the step to smaller particles will only be an option when the visualization and illumination of the experimental set up is optimized. Increasing the numerical aperture has the drawback that the unrestricted measurement depth decreases. The best option to increase the visibility of the experimental set up is to decrease the microchannel depth to the unrestricted measurement depth (150 μm). A velocity measurement with an object plane below the unrestricted measurement depth, will become inaccurate due to the low visibility of the in focus particles as a result of the decreasing NA (section 2.4.6).

3.4.5 Distortion and magnification

An image of a substrate with equidistant positioned grades is taken, to investigate whether any type of distortion is present and whether the magnification of the infinite corrected lens system is indeed 20x. The grates with an intermediate distance of 8 μm are positioned horizontally and vertically to determine the magnification and distortion in both directions (figure 3.9). When positive or negative distortion is present, especially the grades at the outside of the image will have a curvature form. The images in figure 3.9 (a) and (b), show no positive or negative distortion (appendix H.4). Field curvature, recognizable as an object which is only in focus at the center or at the outside of the image, is also not present. The image intensity does not decrease from the center to the outside, which means that vignetting (appendix H.2) has no influence.

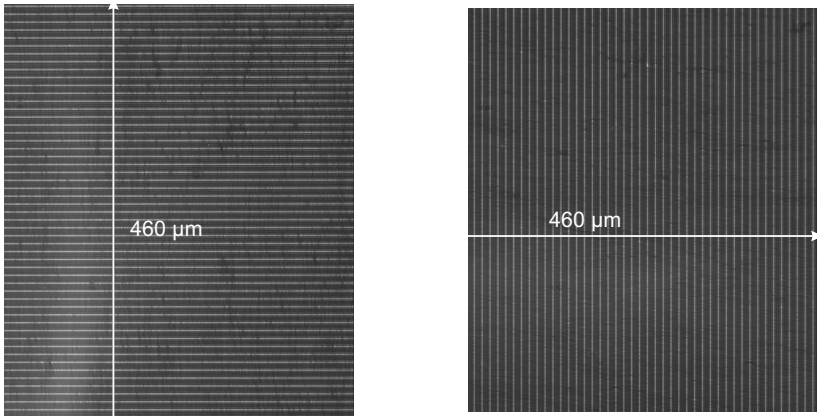

Figure 3.9: Horizontal and vertical grating with a spacing of 8μm between the grates. The grating is used to determine the magnification and image distortion of the infinite corrected lens system.

3.5 Conclusions

A first step to an improved visualization of the particles, is accomplished by using particles with a diameter of 2 μm in stead of 0.86 μm. The mean gray value of the particle image is due to this action increased from 17 to 22. Due to the higher ratio of the particle gray value with respect to the electronic noise of the camera (gray value is 14), it is possible to perform μ PIV measurements with the 2 μm particle. The particle images will be better recognized over the electronic noise if a camera is used with a quantum efficiency of 65 % instead of 25 % (at a wavelength 612 nm). Loss of laser intensity due to the diffusive properties of the diffusor is reduced to maximum 35 %. The transmittance and reflectance of the dichroic mirror is tested by means of a monochromator (ORIEL 77400 Multiscpec spectograph). The dichroic mirror transmits 20 % of the laser light and reflects 40 % of the fluorescent light. The illumination and visualization efficiency of the experimental set up, can be improved by using a dichroic mirror which reflects all laser light and transmits all fluorescent light. The best option to improve the visibility of the experimental set up, is to decrease the channel depth to the unrestricted measurement depth of 150 μm. On long term the step to smaller particles is recommended to increase the visibility of the particles. In order to clearly detect the low fluorescence signal of the smaller particles, the illumination and visualization of the experimental set up has to be improved first. The homogeneity of the laser illumination is improved by a substrate with fluorescent dye and has a standard deviation of 17 at a mean intensity of 142 (gray value). The optical quality of the experimental set up is determined by an image taken from a grating. This image proves that no positive and negative distortions, vignetting and field curvature are present. The field of view of the experimental set up is 460x460 μm. As a result of buoyancy force working on the particle, the particle experiences a velocity of $1.1 \cdot 10^{-5}$ cm/sec in the direction of the gravity. When the relative velocity between the particle and fluid is equal to 1 % of the mean fluid velocity in x-direction, the particle experiences a velocity in y-direction equal to $3 \cdot 10^{-4}$ cm/sec. Both velocities are negligible compared to the mean velocity in x-direction (2.5 cm/sec). The respons time of a particle is equal to 10^{-7} sec.

Chapter 4

Thermal analysis of the pulsating laser

4.1 Introduction

In this chapter the influence of the pulsating laser on the temperature of the micro channel device is investigated. The exponential temperature increase of the micro channel device on a time scale of 10^3 sec is determined, while no water flows through the micro channel device. On basis of the numerical model and exponential temperature measurement, a numerical model is developed which predicts the temperature peaks during a laser pulse cycle depicted in figure 2.1(a). This temperature increase is determined, in order to investigate whether the high intensive laser pulse damages the microchannel device when the illumination path of the μPIV system is optimized. To describe heat transfer on small and higher order timescales, different temporal radiation regimes are defined ([19] and [4]). Also physics describing absorption of laser intensity, are treated.

4.2 Temporal radiation regimes

In short pulse laser applications, the characteristic time scale of the laser pulse may be of the order or less than the intrinsic characteristic time scales of the heat transport mechanisms. To set up an appropriate model a distinction between temporal radiation regimes is defined [19]. The important time scales needed to make a distinction between the regimes are the process time scale [t_p], the diffusion time scale [t_d], the relaxation time for phonon scattering [τ_{phonon}] and the propagation time scale [t_c]. The characteristic time scales are calculated by:

$$\mathrm{t_d} = \mathrm{L}^2/\alpha \quad ; \quad \tau_{\mathrm{phonon}} = \frac{3\alpha}{\mathrm{v}^2_{\mathrm{phonon}}} \quad ; \quad \mathrm{t_c} = \frac{\mathrm{L}}{\mathrm{c}} \tag{4.1}$$

where L is the characteristic length scale of the model, α the thermal diffusivity, c the speed of light in silicon, $\mathrm{v_{phonon}}$ the speed of a phonon.

Regarding the characteristic time scales presented above, the following selection of temporal radiation regimes are made:

- Classical Regime: Heat transfer in a medium obeys Fourier's law for conduction and Beer's law for radiation. A heat transfer problem falls into this category if the process time is much larger compared to the other characteristic time scales.
- Nonclassical Conduction Regime: Heat transfer in a medium is either negligible or has to be modeled by an appropriate macro or micro scale model (see Appendix I, for different macro and micro scale models). A heat transfer problem belongs to this radiation regime if the process time is equal or smaller than the diffusion time.
- Transient Intensity Regime: Absorbance of radiation can not be modeled by Beer's law. A heat transfer problem falls into this regime if the process time is equal or smaller than the propagation time.
- Relaxation Time Regime: In this regime the material properties cannot be considered the same as the classical properties. A heat transfer problem belongs to this regime if the process time is equal or smaller than the relaxation time.

Keeping in mind these defined temporal radiation regimes, an appropriate model is selected to compute both the temperature increase during one laser pulse cycle and exponential temperature increase on a third order time scale.

4.3 Absorbance of laser intensity by matter

When laser light with a certain intensity reaches a surface, in this case silicon, it is partially reflected and absorbed by the surface material (see figure 4.1)

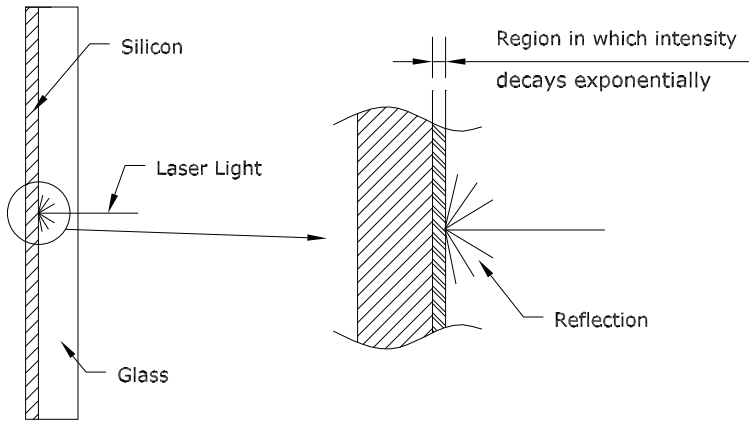

Figure 4.1: Side view of the silicon micro channel device, representing the reflection of a laser pulse and μm-region in which the laser intensity decays exponentially.

The amount of laser intensity which is absorbed at the silicon surface, α_{si}, is calculated by the Fresnel equations (4.2) [17].

$$\alpha_{si} = 1 - (\frac{n_{glass} - n_{si}}{n_{glass} + n_{si}})^2 = \ 0.78 \tag{4.2}$$

Where n_{glass}(1.5) and n_{si} (4.15), are the refractive index of glass and silicon. The exponential intensity decay of laser light in matter, is described by Beer's law for radiation (4.3).

$$I(z) \ = \ \alpha_{si} \ I_o \ e^{(-\alpha_{coeff_{si}} \ z)} \tag{4.3}$$

$$I_o \ = \ \frac{4E_{pulse}}{\pi d^2_{pulse} dt_{pulse}} \tag{4.4}$$

Where $\alpha_{coeff_{si}}$ is the silicon absorption coefficient [$7.85 \cdot 10^5$ m^{-1}] at a wavelength of 532 nm [9], I_o the intensity of the laser pulse calculated according to equation (4.4), E_{pulse} the energy of a single laserpulse [16 mJ], d_{pulse} the diameter of the laserspot [is variant from 2 mm to 16 mm] and dt_{pulse} the pulse width of a laserpulse [5 nsec].
The absorption of laser intensity along the z-axis A(z), which is directed normal to the silicon surface is calculated by

$$A(z) = -\frac{dI(z)}{dz} = \alpha_{si} \ \alpha_{coeff_{si}} \ I_o \ e^{(-\alpha_{coeff_{si}} \ z)} \tag{4.5}$$

The absorbed laser intensity, in the form of photons, leads to a temperature increase of matter by substructural interactions as phonon scattering for semiconductors and phonon-electron scattering for metals.

4.4 Exponential temperature increase

The exponential temperature increase, which results from heating the micro channel device by a pulsating laser for a period of 10^3 sec is investigated by a 3D numerical model and a temperature measurement. The exponential temperature increase is determined for the worst case situation, when no laser intensity is lost during the beam path inside μPIV-experimental set up (see figure 2.3).

4.4.1 Temporal radiation regime

Before a model is set up to predict the exponential temperature increase on a timescale of the order 10^3, the heat transfer problem is classified regarding the different temporal radiation regimes in section 4.2. For the exponential temperature increase with L equal to the height of the silicon substrate [0.6 mm] and t_p equal to the time constant of the exponential temperature curve [O(10^3)sec], holds:

$$t_d = 4 \text{ msec} \;\; ; \;\; t_p = O(10^3) \text{ sec} \;\; \rightarrow \;\; t_d << t_p \tag{4.6}$$

Because the diffusion time is much smaller compared to the process time, is chosen to model heat transfer by the classical diffusion equations.

4.4.2 Temperature measurement

Firstly a temperature measurement is carried out, to determine the exponential temperature increase in case no laser intensity is lost along the optical illumination path of the μPIVsystem. This is done by positioning the sample with the teflon holder just after 92 % transmission mirror (2.3). For a schematic of the set up used to measure the exponential temperature, see figure 4.2.

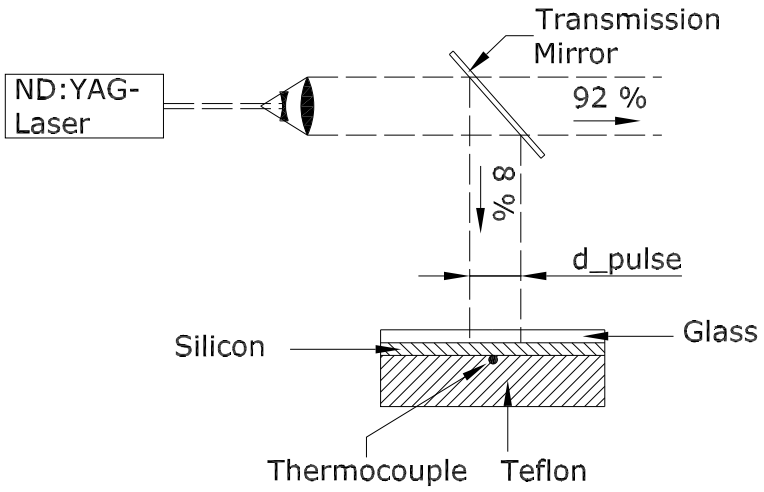

Figure 4.2: Schematic of the experimental set up, used to measure the exponential temperature increase on a time scale of 10^3 sec due to the heat input by a pulsating laser.

The laser beam passes a negative and positive lens, a 92 % transmission mirror and finally reaches the silicon surface. At the silicon surface the laser intensity gets partially reflected and absorbed. The absorbed laser intensity, leads to an exponential temperature increase, which is measured by a K-type thermocouple and logged by Virtual bench logger 2.6. During this measurement the temperature is logged for a period of 1400 seconds while laser pulses heat up the micro channel device. The thermocouple is attached between the sample and the insulating teflon block. Thermal contact resistance between thermocouple and sample is minimized by using thermal conductivity gel. Ambient temperature rises with 1.5 K, due to

the heat generation of the pulsating ND:YAG laser and PC's in the lab. For the temperature measurement two types of samples are used, namely:

1. Micro channel device, which is used during the μPIV-experiment
2. Silicon plate with glass cover, representing the model geometry by which the micro channel device is modeled in section 4.4.3.

The results of both measurements are presented and compared with numerical results in section 4.4.4.

4.4.3 Numerical model of exponential temperature increase

To compute the exponential temperature increase of the micro channel device, a 3D Transient Model [model A] is set up with the finite element package COMSOL. The micro channel device is modeled by a silicon plate and a glass cover with equal dimensions. For an overview of the geometry and the numbering of boundary conditions, see figure 4.3.

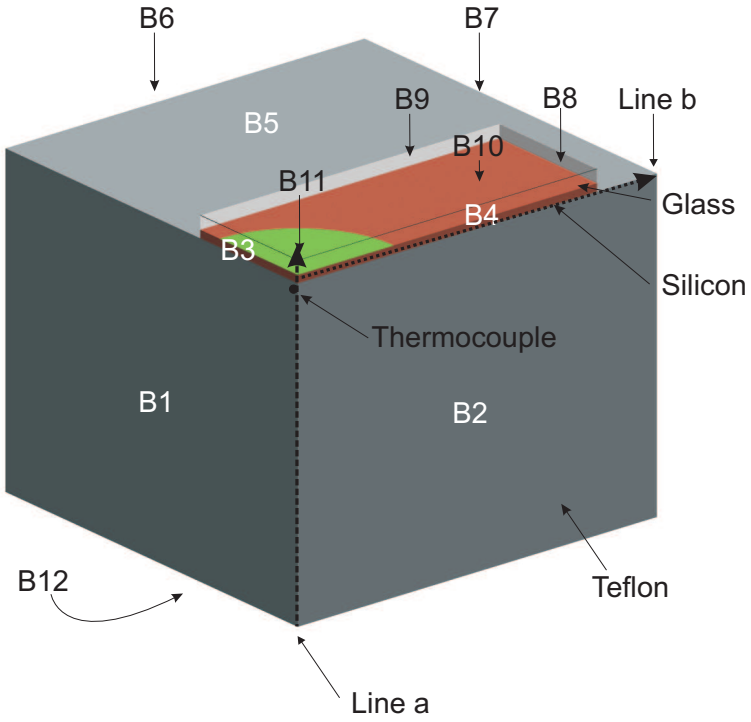

Figure 4.3: Geometry and boundary condition numbering of the 3D Numerical COMSOL model, used to compute the exponential temperature increase on a timescale of 10^3 sec .

The geometry of the model consists of a teflon block (60 mm $*$ 60 mm $*$ 24 mm), silicon plate (50 mm $*$ 20 mm $*$ 0.6 mm) and a glass cover (50 mm $*$ 20 mm $*$ 1 mm). The describing equations are solved by making use of triangular quadratic La Grange elements. To reduce the number of elements and computation time, only a quarter of the problem is modeled by making use of x and y symmetry axis. The linear system solver GMRES with incomplete LU-preconditioner is used for the time iteration process.

The 3D-model is described with the heat equation:

$$\rho c_p \frac{\partial T}{\partial t} = k\nabla^2 T + Q \tag{4.7}$$

Where T is the temperature, t the time, Q the heat source, ρ the density, c_p the heat capacity and k the conductivity of Teflon, Silicon and Glass. The values of these thermal properties can be found in table A.1. The average heat input of the pulsating laser on the silicon surface, is prescribed as a heat flux [I_{3D}] on boundary 11.

$$I_{3D} = \frac{4(E_{pulse} n_{pulses} f_{laser})}{\pi d_{pulse}^2} = 2.4 \cdot 10^3 \text{ W/m}^2 \tag{4.8}$$

Where E_{pulse} is the energy of a single laser pulse [16 mJ], n_{pulses} is the number of pulses during one laser pulse cycle [2 pulses], f_{laser} the frequency of the laser [15 Hz] and d_{pulse} the diameter of the lasers spot before the beam is directed inside the experimental set up [16 mm].

The following conditions are prescribed for the 3D model:

1. The x and y axis symmetry (B1 to B4) , $-k\frac{\partial T}{\partial n} = 0$
2. Radiation and convection (B5 to 10), $-k\frac{\partial T}{\partial n} = h(T - T_\infty) + \epsilon\sigma(T^4 - T_\infty^4)$
3. Heatflux I_{3D} at B11, $n(k_1 T_1 - k_2 T_2) = I_{3D}$
4. Constant temperature at B12, $T = T_\infty$
5. Initial condition at teflon block, glass and silicon plate, $T(0) = T_\infty$

Where h is the heat transfer coefficient [5-10 W/m^{2}K], ϵ emission coefficient for silicon, glass and teflon (appendix A.1), σ the Stefan Boltzman constant [$5.67 \cdot 10^{-8}$], T_∞ the ambient temperature [298 K].

4.4.4 Results

Model A is validated by comparing the numerical results with the temperature measurement on both samples. Note that two parameters, the absorption factor and the heat transfer coefficient, are not known exactly. Therefore the absorption factor and heat transfer coefficient are varied, to determine the influence of these two parameters on the exponential temperature curve, see figure 4.4

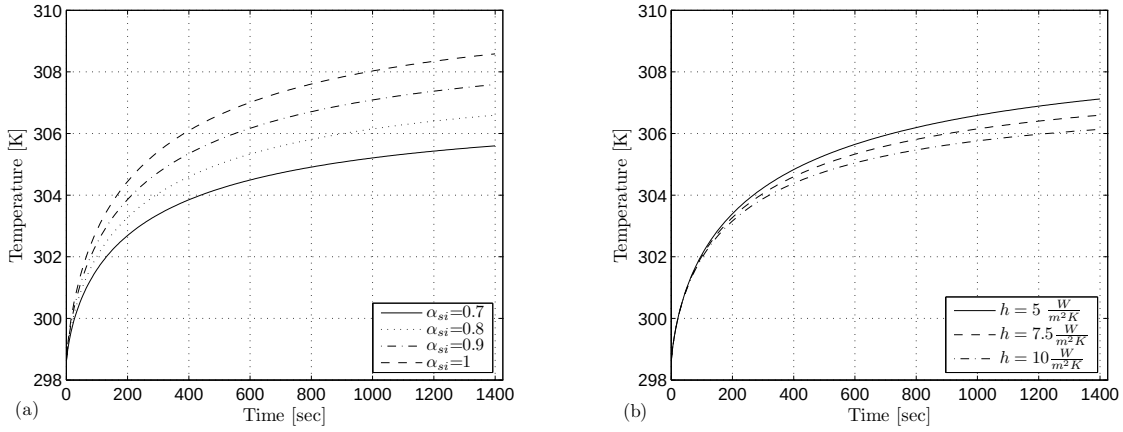

Figure 4.4: Exponential temperature increase for cases in which α_{si} is varied from 0.7 to 1, while keeping h constant at 7.5 W/m^{2}K. (a). Exponential temperature increase for cases in which h is varied from 5 to 10 W/m^{2}K, while keeping α_{si} constant at 0.8 (b)

Although the temperature curves in the both simulations have not reached equilibrium it is possible to determine the influence of the heat transfer coefficient and absorption factor on the temperature increase ΔT [$\Delta \mathrm{T} = \mathrm{T}(1400) - \mathrm{T}(0)$] and initial temperature increase $[\frac{\partial \mathrm{T}(0)}{\partial \mathrm{t}}]$. The simulations in figure 4.4 (a) show that the temperature increase and initial temperature increase are proportional dependent on the absorption factor α_{si}. The simulations in figure 4.4 (b) show that the heat transfer coefficient only has a small effect on the temperature increase. When the heat transfer coefficient is increased from 5 to 10, ΔT decreases from 8.5 K to 7.5 K. From this simulations it is concluded that the absorption factor has the largest influence on both ΔT and $[\frac{\partial \mathrm{T}(0)}{\partial \mathrm{t}}]$.
Therefore the absorption factor is variated in order to fit the numerical and measured exponential temperature curve (figure 4.5). From figure 4.5, it is clear that the result of the simulation with $\alpha_{\mathrm{si}} = 1$ and $\mathrm{h} = 7.5$ W/m^{2}K, matches well with the measurement on the microchannel. Although the good fit, it has to be noticed that an absorption factor of 1 is physically overestimated. Some part of the laser light, always gets reflected by the silicon and glass surface. An explanation for the large absorption factor is an ambient temperature increase during the measurement, not incorporated in the model. In case the ambient temperature increases during the measurement, it will result in a higher stationary temperature leading to an overestimated absorption factor in the numerical model.

Also the different exponential temperature curve between both temperature measurements, has to be noticed. A cause for the increased exponential curve belonging to the microchannel device, can be the anti-reflective working of the microchannels or the presence of a small layer of low conductive glue between the glass cover and microchannel substrate.
By means of the model A and the exponential temperature measurement, it is determined that the temperature of the microchannel device increases with 10 K over a time of 1000 sec.

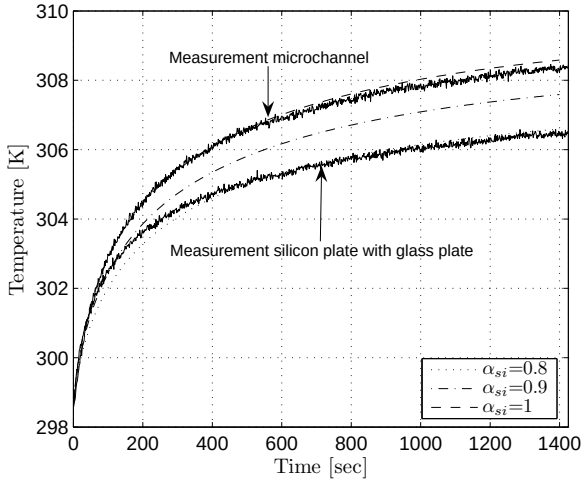

Figure 4.5: Measured and numerical determined temperature curve, where the α_{si} is varied from 0.8 to 1 and h is kept constant at 7.5 W/m^{2}K

4.5 Temperature increase during laserpulse cycle

Another point of interest is the temperature increase during the laserpulse cycle (figure 2.1(b)). Considering the temporal radiation regimes, a negligible conduction model and a numerical 2D axis symmetric model [Model B] are set up to predict the temperature during a laserpulse cycle. Finally the influence of the laserspot size on the temperature peak during the laserpulse is investigated. By the predicted temperature peak, it is examined whether measures have to be taken to prevent that the microchannel device is damaged when the illumination intensity increases due to the optimization of the optical illumination path of the μPIV system.

4.5.1 Temporal radiation regime

Firstly is determined the radiation regime on basis of the characteristic times. The diffusion time for model b, stays unchanged compared to the model which describes the exponential temperature increase (4 msec). The process time, however, is equal to the duration of the laserpulse (5 nsec). Because the process time is much smaller than the diffusion time, model b falls into the regime of non classical conduction. Which means that heat transfer can either be modeled by a CV wave model, phaselag model or classical diffusion model. In order to investigate these models, the predicted temperature solution as a result of a femtosecond laserpulse is compared for the different models in appendix I. On the basis of this study is determined that all models predict the same maximum temperature at the end of the

laserpulse. Also is found that the classical diffusion predicts the highest temperatures during the cooling down period and that a thermal disturbance (laserpulse) not propagates as a wave in semiconductors. Because the diffusion equations are standard incorporated in the COMSOL finite element package and the temperature peak during the laser illumination is of primary concern, is chosen to use the classic diffusion equations.

4.5.2 Negligible conduction model

A first estimation of the temperature peak during a laserpulse equal to 5 nsec, is made by assuming that there is not enough time for the absorbed heat to be spread by thermal diffusion. This means that all heat generated by the laser, results in a temperature increase of a circular volume with a certain depth z_{end} and a width equal to the laserspot diameter. The depth of the circular subdomain, z_{end}, is determined as the position at which the laser intensity I(z) in equation (4.3), has been decreased to 1 % of its maximum value I_o

$$\frac{I(z_{end})}{I_0} = 0.01 \quad ; \quad z_{end} = -\frac{\ln(0.01)}{\alpha_{coeff_{si}}} = 6\ \mu m \tag{4.9}$$

Because heat transport by conduction can be neglected it is seen that equation (4.7) reduces to equation (4.10). Where Q is replaced by equation (4.5), which describes heat absorbance in matter according to Beers' law.

$$\rho c_p \frac{\partial T}{\partial t} = \alpha_{si}\ \alpha_{coeff_{si}}\ I_o\ e^{(-\alpha_{coeff_{si}}\ z)} \tag{4.10}$$

In figure 4.6 the temperature over the first 6 μm of the silicon substrate is plotted, after a laserpulse of 5nsec.

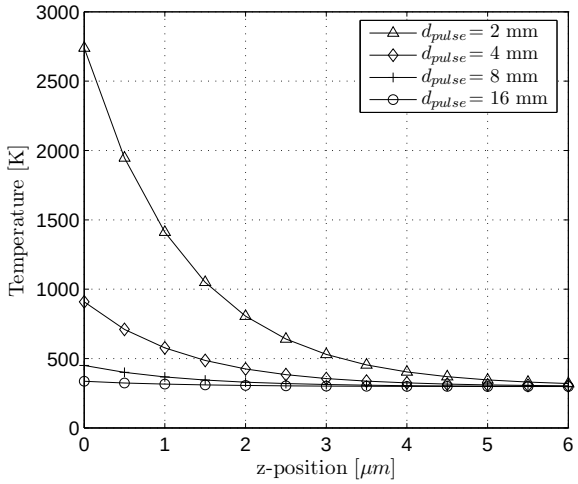

Figure 4.6: Temperature plotted along the z-axis after a laserpulse of 5 nsec, for the negligible conduction analysis. The laser diameter is increased from 2, 4, 8, to 16 mm, to relate the laserspot size to the maximum temperature increase.

As follows from figure 4.6 the peak temperature is strongly dependent on the laserspot diameter. When the laserspot diameter increases from 2 to 16 mm, the temperature at z=0 (top surface silicon substrate) decreases from 2740 K to 340 K.

4.5.3 Transient 2D axis symmetric model

Next to the negligible conduction analysis a 2D axis symmetric model defined as model B in section 4.5, is made. Model b has a 2D-axis symmetric geometry which approximates the geometry of the model A (figure 4.3). Because of the large amount of elements needed to compute the high temperature gradient during a laserpulse cycle, a 3D numerical geometry is not useful. The surfaces at which convection and radiation are prescribed, are equal in size for model A and B . This ensures a nearly equal stationair temperature, which is needed to validate model b in section 4.5.4. The outline of the 2D axis symmetric problem, with the numbering of the surfaces and boundary conditions is presented in figure 4.7.

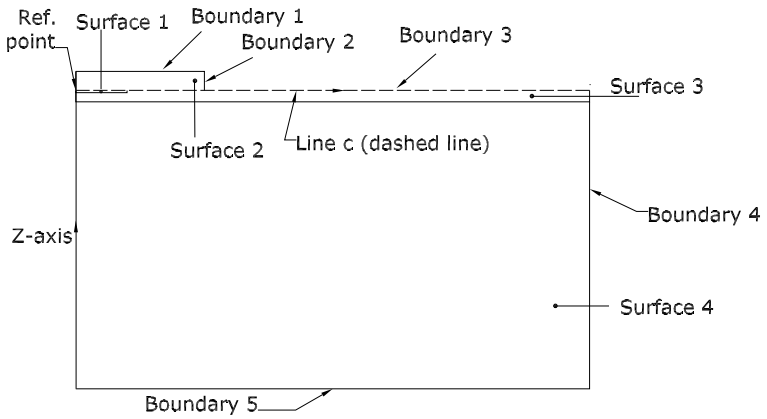

Figure 4.7: Outline of 2D axis symmetric model with boundary and surface numbering, used to predict the temperature during a laserpulse cycle.

where surface 1 represents the area in which the laser intensity is absorbed according to equation (4.5), surface 2 represents the glass cover, surface 3 represents the silicon plate, surface 4 the insulating teflon block at the back of the silicon plate. The diameter of the teflon block and silicon plate with glass cover is respectively, 35 mm and 18 mm. The height of the teflon block, silicon plate and glass cover is equal to heights of the model which is used to describe the exponential temperature increase.
The 2D axis symmetric model is also described with the heat equation (4.7), where Q is equal to A(z) denoted in equation (4.5). The term I_o in equation (4.5) is replaced by equation (4.11), to simulate the pulsating laser at the silicon surface during a pulse cycle. When one the logical conditions between the brackets in equation 4.11 hold, it gets the value one which means that A(z) is prescribed.

$$I_o(t) = I_o(t_{p_{start}} \leq t \leq t_{p_{end}}) + I_o(t_{p2_{start}} \leq t \leq t_{p2_{end}}) \tag{4.11}$$

where I_o is equal to equation (4.4), $t_{p_{start}}$ is the time instant at which the laser pulses for the first time during one time increment [1 nsec], $t_{p_{end}}$ is the time increment at which the first

laser pulse ends [5 nsec], $t_{p2_{start}}$ is the time instant at which the laser pulses for the second time during one time increment [5 μsec + 6 nsec], $t_{p2_{end}}$ is the time increment at which the second laser pulse ends [5 μsec + 10 nsec]. In figure 4.8 is given an overview of the time, where A(z) is prescribed in time according to equation (4.11).

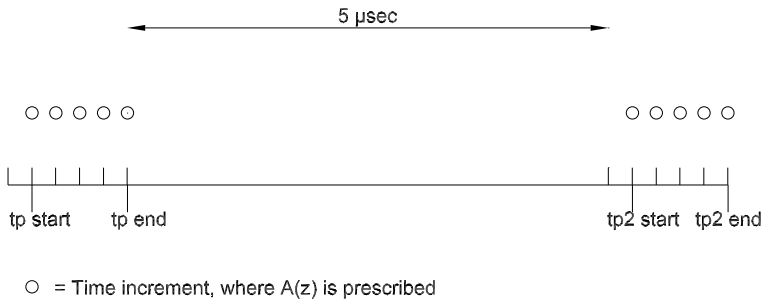

Figure 4.8: Overview of the time increments where the heat input A(z) is prescribed, to simulate the temperature peaks of two successive pulses.

The following conditions are prescribed for 2D axis symmetric model (see section 4.4.3 for the corresponding equations):

1. Natural boundary condition describing radiation and convection on boundary 1 to 4 inclusive
2. Natural boundary condition describing z-axis symmetry
3. Essential boundary condition describing constant temperature at boundary 5
4. Initial boundary condition on surface 1 to 4 inclusive

The heat transfer coefficient, emission coefficient, ambient and initial temperature are all equal to the model which is used to describe the exponential temperature increase (section 4.4.3). The heat equation (4.7), with the initial and boundary condition are solved by the finite element package COMSOL, making use of rectangular quadratic La grange elements. The direct linear system solver UMFPACK is used for the time iteration process.

4.5.4 Results

First the stationary temperature distribution of the model A and B, are compared to each other. When the stationary temperature distribution of both models is equal, it is possible to validate the model A. This validation of model B is performed by a simulation of the temperature peaks during a laserpulse cycle. Finally the influence of the laserspot diameter on the temperature peak is investigated.

2D stationary result compared with 3D model

In order to compare the stationary temperature distribution of model A and B, a constant heat source $Q(z)_{constant}$ is described at surface 1 in model B.

$$Q(z)_{constant} = \alpha_{si}\ \alpha_{coeff_{si}}\ I_{3D}\ e^{(-\alpha_{coeff_{si}}\ z)} \tag{4.12}$$

In figure 4.9, the stationary temperature distribution is plotted model A and B. In the left graph of figure 4.9 the temperature curve is plotted along the z-axis and line a, defined in figure 4.3 and figure 4.7 respectively. In the right graph of figure 4.9 the temperature curve is plotted along line c and line b defined in figure 4.3 and figure 4.7 respectively.

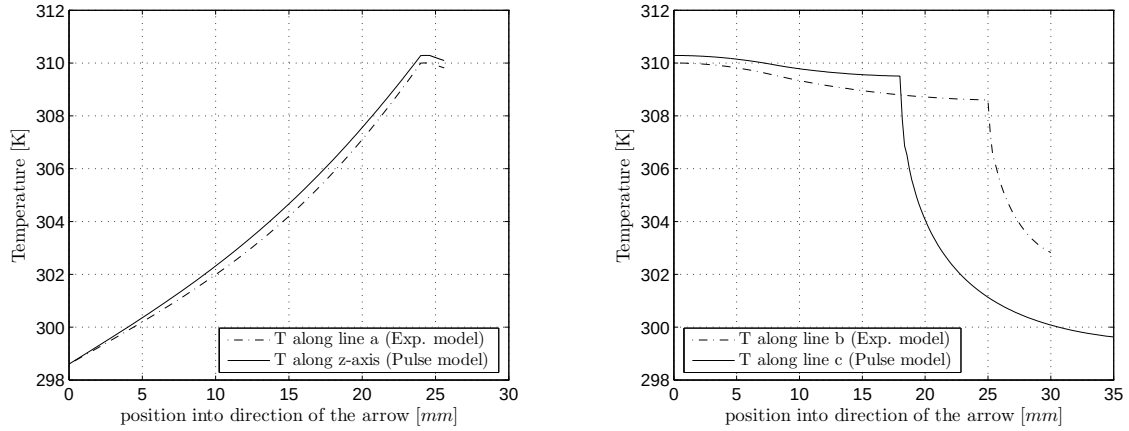

Figure 4.9: Stationary temperature distribution along line a and z-axis defined in figure 4.3 and 4.7 respectively (left). Stationary temperature distribution along line b and line c defined in figure 4.3 and 4.7 respectively (right).

From the left and right graph in figure 4.9, it is obvious that the stationary temperature distribution for both models is almost equal.

Validation of 2D axis symmetric model

As a result of the small time scale of the laserpulse, it is almost impossible to validate the temperature during one laserpulse cycle experimentally. Simulating successive laserpulse cycles, in order to compare the resulting exponential temperature curve with the experimental determined temperature curve in figure 4.5, is because of the excessive computation time also not an option. In order to validate the model b, a closer look is taken to the situation when a stationair temperature distribution is achieved. When the temperature has become stationair in the model b, it means that the temperature after one pulse cycle is equal to the initial temperature of the pulse cycle. To investigate whether the initial temperature and temperature after a laser pulse are equal, a laser pulse cycle is simulated with an initial temperature distribution equal to the distribution presented in figure 4.9. The temperature at the location of the thermocouple during a laserpulse cycle is presented in the left graph of figure 4.10. The diameter of the laserspot is equal to 12 and 16 mm. The temperature difference $[\Delta T_{pulse}]$

between the temperature at t=0 sec and t=$\frac{1}{15}$ sec, for various laser diameters is presented in the right graph of figure 4.10.

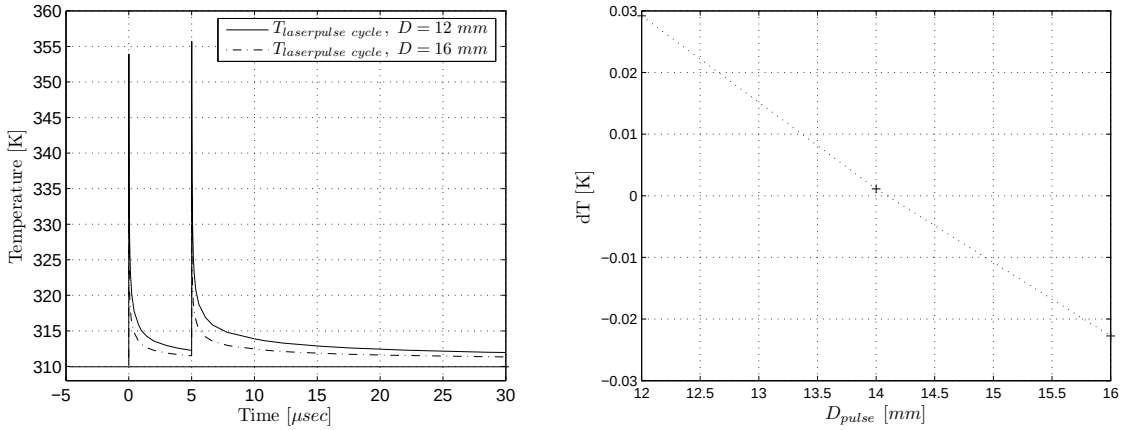

Figure 4.10: Plot of the temperature during a laserpulse cycle, predicted by the model b in which the laserspot diameter is equal to 12 and 16 mm (left). Plot of the temperature difference ΔT_{pulse}, for various laser spot diameters. (right)

As can been seen from the right graph of figure 4.10, the temperature difference ΔT_{pulse} is almost 0 for the laser diameter (16 mm) by which the silicon plate is illuminated in the temperature measurement (figure 4.2).

Influence laser spot on temperature peak

The influence of the laserspot diameter on the temperature increase ΔT_{peak} is investigated, by means of model b. Where ΔT_{peak} is the difference between the initial temperature (298 K) and maximum temperature after a laserpulse of 5nsec. In figure 4.11 the temperature [T(z,t)] is presented, along the z-axis of surface 1 (figure 4.7).

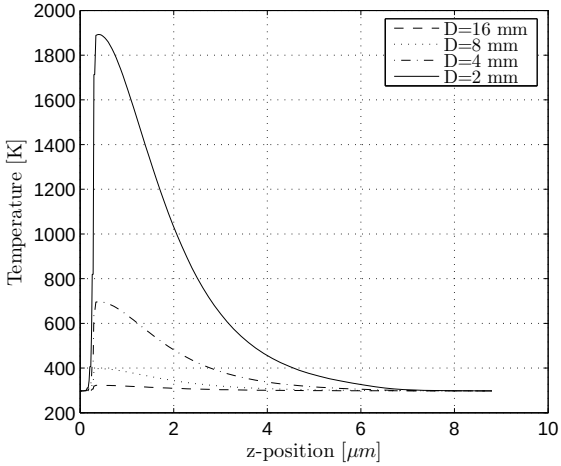

Figure 4.11: Temperature plotted along the z-axis of surface 1 (figure 4.7) for an different laserspot diameters, after a laserpulse of 5 nsec.

When the laserspot diameter is decreased from 16 mm, 8 mm, 4 mm to finally 2 mm, the temperature difference ΔT_{peak} increases from 25 K, 100 K, 400 K, 1600 K. Just like the negligible conduction model, model b predicts a opposite proportional relation between the laserspot surface and the temperature increase. Only the maximum temperature predicted by model b, is lower compared the results of the negligible conduction model. This lower maximum temperature is caused by the fact that heat transfer by thermal diffusion is incorporated in model b.

Discussion of the results

Both the negligible conduction model as model b prove that the peak temperature in the first 6 μm of the silicon surface, can rise to values far above 1000 K when all laser intensity is concentrated in a small laserspot. Such high temperature's lead to melting of the silicon top layer (silicon melt point is 1683 K). Even temperature peaks below the melt temperature will damage the microchannel device as a result of high internal stress initiated by the high temperature gradient. Because of the predicted excessive temperature peak when a laserpulse of 16 mJ is projected on a spot with a diameter of 2 mm, it is recommended to enhance first the visualization part of the experimental set up.

Chapter 5

Experiments

5.1 Introduction

In order to estimate the accuracy and reliability of the developed μPIV-system, the measured velocity field is compared to an analytic and numerical determined solution. To determine the equations for a typical microflow problem, the flow regime is determined by means of the Reynolds number. The measured velocity field in a rectangular microchannel is compared with the analytic solution for a Poiseuille flow between two parallel plates. Subsequently a μPIV measurement is done with a sinusoidal channel. The velocity field resulted from this measurement, is compared to a numerical determined flow field. Finally a discussion of the results is given with recommendations to increase the accuracy of the μPIV measurements in the future.

5.2 Flow regime

In order to determine a solution to a given flow field, it is important to use the appropriate describing equations. Therefore the flow problem is characterized by means of the Reynolds number (Re):

$$\mathrm{Re} = \frac{\text{inertia forces}}{\text{viscous forces}} = \frac{\rho \mathrm{U_{mean}} \mathrm{L_w}}{\mu} \tag{5.1}$$

Where the mean velocity $\mathrm{U_{mean}}$ is of the order $1 \cdot 10^{-2}$ m/sec , the width of the microchannel $\mathrm{L_w}$ is $1 \cdot 10^{-4}$ m, the dynamic viscosity μ is $1 \cdot 10^{-3}$ $\mathrm{kgm^{-1}sec^{-1}}$ and the density ρ is equal to $1 \cdot 10^{3} \mathrm{kg/m^3}$. The Reynolds number is of the order 1. Therefore the viscous forces and inertia forces are in balance. This means that incompressible flow inside the micro channel is governed with the complete Navier Stokes and Continuity equation:

$$\rho(\frac{\partial \underline{u}}{\partial t} + \underline{u}.\nabla \underline{u}) = -\nabla \underline{p} + \rho \underline{g} + \mu \nabla^2 \underline{u} \tag{5.2}$$

$$\nabla.\underline{u} = 0 \tag{5.3}$$

Where $\underline{u}$ is the velocity vector with the velocity U(y) in x direction and V(y) in y direction (for a definition of the x and y direction see figure 5.1), t the time, p the pressure, g the gravity constant, μ the dynamic viscosity. For flow fields with Re << 1 or Re >> 1, the Navier Stokes equation reduces respectively to the Stokes or Euler equation. A Reynolds number of the order 1 means, that the flow inside the microchannel is laminar. The transition from a laminar to a turbulent flow in a microchannel, takes place at a Reynolds number of 1800 [16].

5.3 Micro flow in a rectangular channel

In this section attention is given to the μPIV measurement performed with the rectangular channel. First the analytic solution to the Navier Stokes equation for a Poiseuille flow between two parallel plates is given. Subsequently the measurement method and experimental results are shown.

5.3.1 Analytic solution

For a steady and fully developed flow field sufficient far away from the bottom and top wall of the microchannel, the analytic velocity in the x,y plane [$U_a(y)$] is calculated by equation (5.4). Equation (5.4) is the exact solution to the Navier Stokes equation, for a Poiseuille flow between two parallel plates [15].

$$U_a(y) = 4\ U_{max}\ \frac{y}{L_w}\ (1 - \frac{y}{L_w}) \tag{5.4}$$

With U_{max} the maximum velocity at $y = L_w/2$.

5.3.2 Measurement method

To create a fluid flow through the microchannel device (figure 2.4), a fluid system is set up. This fluid system consists of a Harvard PHD2000 syringe pump, stiff tubing which connects the pump to the microchannel device, the microchannel device and a reservoir where the water with seeding is preserved. A T-connection made out of glass is positioned between the pump and microchannel device, which ventilates the tubing to prevent air bubbles reach the microchannel device. At the inlet of the fluid system a constant volume flux of 100 ml/hr is delivered by the syringe pump. For a schematic of the flow system, see figure 5.1 (a). The microchannel device is placed on a teflon block, and carefully positioned by x, y and z translation stages (appendix D.2).
The exact field of view of 460 x 460 μm is determined, before the measurement is performed (see section 3.4.5). The distance from the field of view to the inlet of the microchannel is about 8 cm. For the visualization of the (deionized) water flow, fluorescent particles with a diameter of 2μm (Duke scientific) are used. The software package PIV VIEW 3.4 with an interrogation window of 32x32 pixels and an overlap of 50 % is used, to calculate velocity vectors out of the particle displacement. With a field of view of 460x460 μm and an interrogation window of 32x32 pixels with 50 % overlap, an in plane spatial resolution of 7.36x7.36 μm (section 2.4.5) is realized. When particles with a diameter of 2 μm are used, the out of plane resolution

($2z_{corr}$) becomes 18 μm (equation (2.5)). Multi-grid interrogation with Gaussian sub pixel interpolation is used to determine the correlation peak of two subsequent images. The velocity U and V are measured for a period of 30 seconds, corresponding with 450 image pairs.

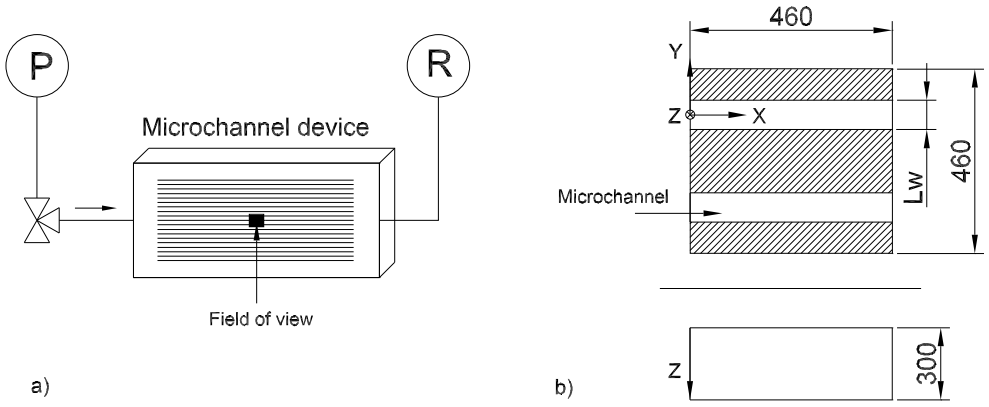

Figure 5.1: Overview of the fluid network by which a flow is generated in the microchannel (a). Where P stands for pump and R for reservoir. Further is zoomed in at the field of view with the dimensions 460 x 460 μm (b). The velocity [U(y)] in the microchannel is measured in the x,y plane at certain depths z. The centerline of the upper microchannel is at y=0 and the depth z is measured from the top of the microchannel.

5.3.3 Experimental results

Flow field

In figure 5.2 a contour plot of $\overline{\mathrm{v(y)}}$ is presented. The velocity field $\overline{\mathrm{v(y)}}$ is fully developed and is therefore undependable of the x-direction. The vectors plotted inside the microchannels represent the measured velocity with a value $|\overline{\mathrm{v(y)}}|$ and direction $\overrightarrow{v(y)}$ in the x,y plane. The origin of the x,y coordinate axis is positioned at the centerline of the upper microchannel (figure 5.1 and 5.2). Where $|\overline{\mathrm{v(y)}}|$ with a direction equal to $\overrightarrow{v(y)}$ is calculated according to:

$$\overline{\mathrm{v(y)}} = \sqrt{\overline{\mathrm{U(y)}}^2 + \overline{\mathrm{V(y)}}^2} \quad ; \quad \overrightarrow{v(y)} = \overline{\mathrm{U(y)}}\,\overrightarrow{e}_{\mathrm{x}} + \overline{\mathrm{V(y)}}\,\overrightarrow{e}_{\mathrm{y}} \tag{5.5}$$

The overline in the terms $\overline{\mathrm{U(y)}}$, $\overline{\mathrm{V(y)}}$ and $\overline{\mathrm{v(y)}}$ indicates that the mean is calculated over instantaneous velocity measurements during the stationary period of the experiment (last 20 seconds of the experiment). The terms $\overrightarrow{e_x}$ and $\overrightarrow{e_y}$ are the unity vectors in x and y direction. Regarding the vector and contourplot of the velocity $\overline{\mathrm{v(y)}}$ in figure 5.2, it is obvious that the velocity decreases gradually from the centerline of the microchannel to the boundary. No irregularities such as agglomerated particles and dust disturb the flow. The maximum $\overline{\mathrm{U_{max}}}$ and mean velocity $\overline{\mathrm{U_{mean}}}$ in x direction is 3.4 cm/sec and 2.4 cm/sec. The maximum $\overline{\mathrm{V_{max}}}$ and mean velocity $\overline{\mathrm{V_{mean}}}$ in y direction is 0.02 cm/sec and 2 $\cdot 10^{-3}$ cm/sec. These velocities are calculated over the total velocity field of the upper microchannel in figure 5.2.

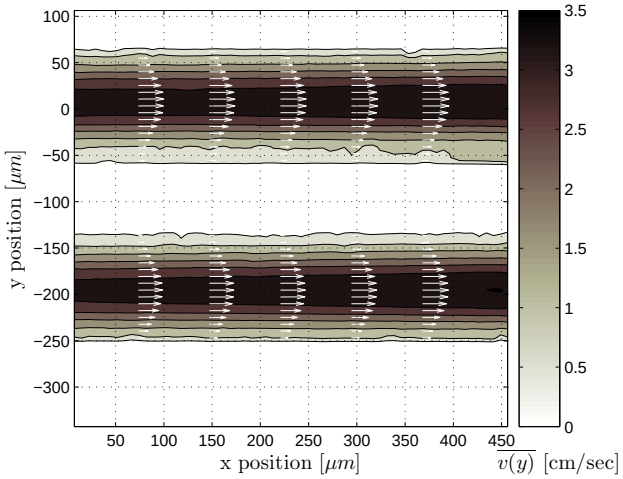

Figure 5.2: Contourplot of the velocity $\overline{\mathrm{v(y)}}$ through two microchannels, calculated by equation (5.5). The vectors inside the microchannels represent the velocity $\overline{\mathrm{v(y)}}$ measured in the x,y plane. The velocity $\overline{\mathrm{v(y)}}$ is measured at z=25 μm.

Stationary and fully developed flow

In figure 5.3 (a) and (b) the velocity $\overline{\mathrm{U(y=0)}}$ along the centerline of the channel and the instantaneous velocity U(0,230,t) over the total time span of the experiment are plotted respectively.

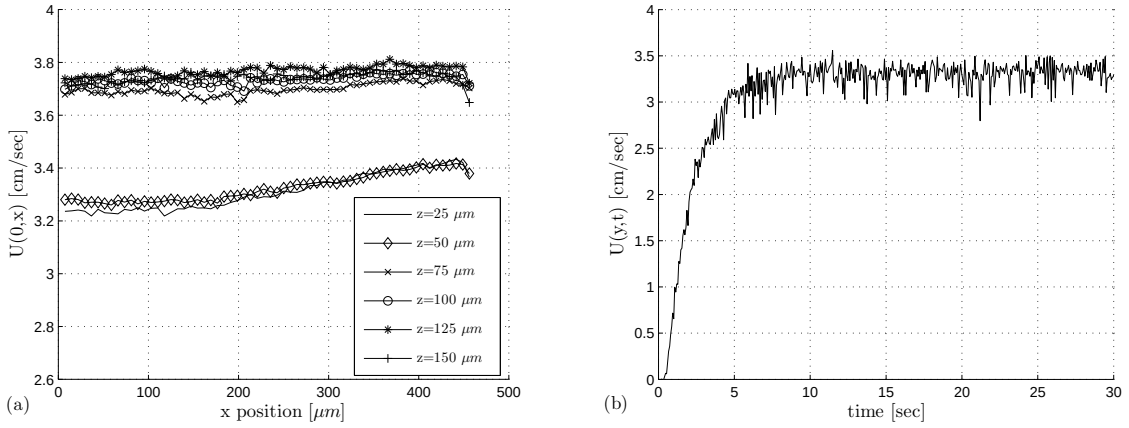

Figure 5.3: Plot of $\overline{\mathrm{U(y)}}$ along the centerline y=0 of the upper microchannel (a). Plot of the instantaneous velocity U(y,t) at the point with position y=0 and x= 230 μm in the upper microchannel (b). The velocity $\overline{\mathrm{U(y)}}$ is measured from z= 25 μm to 150 μm. The velocity U(y,t) is measured at z= 50 μm.

The flow in the microchannel is fully developed when $\frac{\partial \overline{U(x)}}{\partial x} = 0$. Regarding figure 5.3, it is obvious that the velocity $\overline{U(y)}$ at z=75 to 150 μm is fully developed. Only the the velocity at z= 25 and 50 slightly increases with 0.1 cm/sec. Because the distance of the measurement position to the inlet (8 cm) is much larger as the hydrodynamic entrance length, it is unlikely that the flow is still developing. The velocity increase of 0.1 cm/sec could be caused by a small clockwise rotation around the y-axis, depicted in figure 5.1 (b). In this case the velocity in the x,y plane is measured at an increasing depth along the length of the microchannel, which results in a gradually higher measured velocity. By figure 5.3 (b), it is clear that the velocity stops increasing after a period of 10 seconds. This means that the flow has become stationair.

Accuracy of μPIV

The accuracy of the μPIV measurement is evaluated, by comparing the measured velocity $\overline{U(y)}$ with the analytic velocity profile $U_a(y)$ presented in subsection 5.3.1. Where U_{max} in equation (5.4) is replaced by the measured $\overline{U_{max}}$. In figure 5.4 (a) the measured and analytic derived velocity profile are plotted. For this velocity measurement, the first and second correlation peak are plotted in figure 5.4 (b). The velocity $\overline{U(y)}$ is measured at a depth of 50 μm.

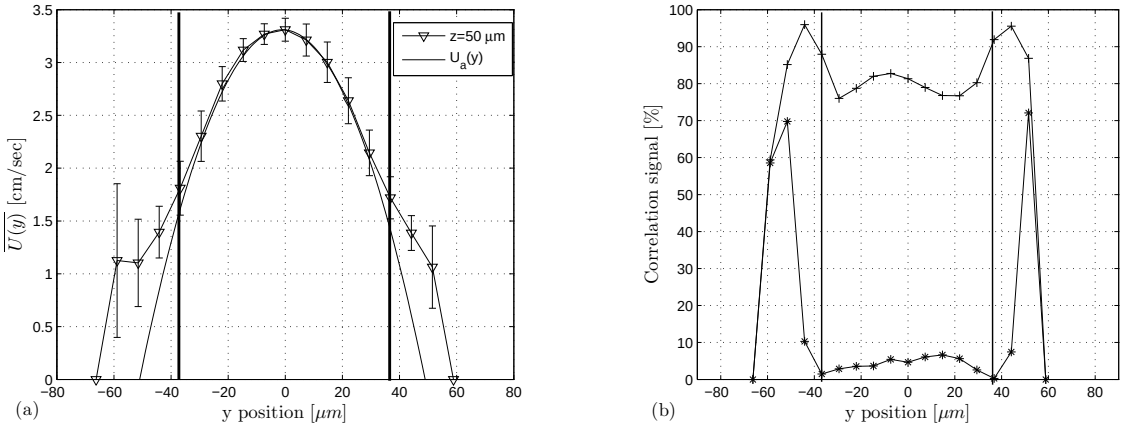

Figure 5.4: The analytic $U_a(y)$ and measured velocity profile $\overline{U(y)}$ (a) are plotted next to the first and second correlation peak of the measurement (b). The presented profile of correlation peak 1 and 2 is the mean correlation of 350 image pairs. Where -+ represents the course of the first correlation peak and -* the course of the second correlation peak.

In the mid domain, the domain between the two vertical lines in figure 5.4 (a), the measured and analytic velocity profile match very well. This mid domain with a width of 74 μm corresponds with the area in figure 5.5, where the particles can be clearly recognized. In the region outside the two vertical lines, the outside domain, the analytic and measured velocity deviate. This deviation can be subscribed to the low visibility of the particles in the outside domain and interrogation windows with a center near or at the boundary of the microchannel geometry. A certain part of these interrogation windows overlaps an area where particles are overshadowed by background noise or even not present.

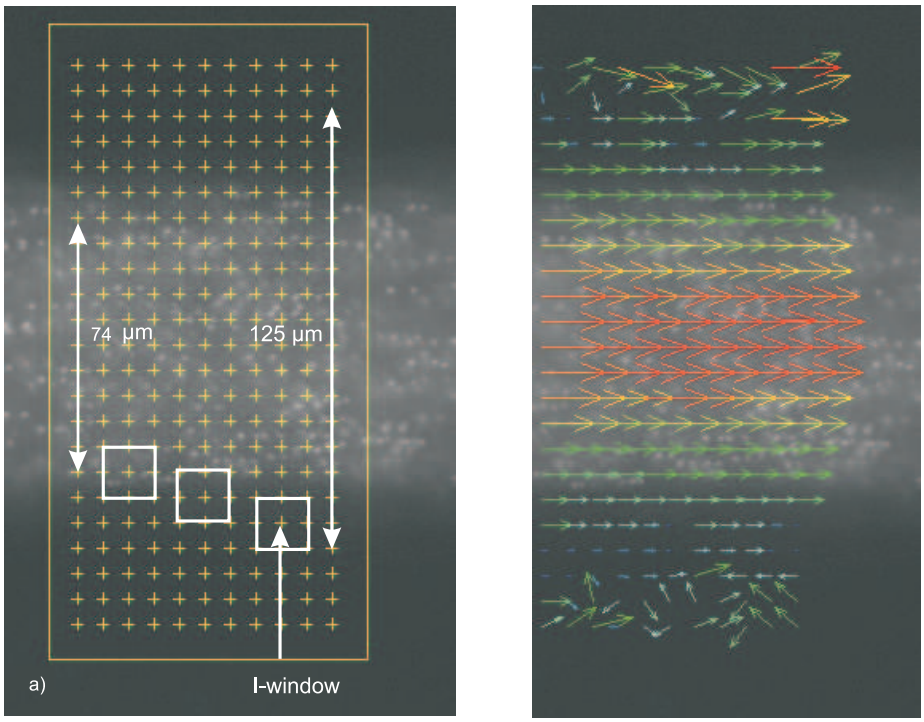

Figure 5.5: Interrogation grid where '+' indicates the center of an interrogation window (a). At each interrogation window center is calculated a velocity vector (b)

Because the particles can not be detected over the background noise of out of focus particles, the cross correlation algorithm becomes inaccurate in the outside region. This inaccurate cross correlation algorithm leads to inaccurate velocity vectors (figure 5.5(b)). The accuracy of the correlation algorithm can be tested by calculating the detectability [ϵ], defined in section 2.5.2. In case of bad correlation statistics, the signal strength of the second correlation peak will lie close to the signal strength of the first correlation peak. For the outside domain, this is indeed the case (see figure 5.4 (b)). The detectability ϵ in the outside domain decreases from from 10 to 1 at the last three non-zero data points. Inside the mid domain the detectability lies between the values 60 and 12. The standard deviation of $\overline{U(y)}$ indicated by the errorbars in figure 5.4, is in the outside domain (0.7 cm/sec) also much larger compared to the standard deviation in the mid domain (0.2 cm/sec).
To filter out outliers caused by interrogation windows with a center near or at the boundary of the microchannel is important to determine the exact location of the microchannel device. With the exact location of the microchannel geometry is known, it is possible to cover the region outside the microchannel device. On this way outliers caused by interrogation windows which overlap an area outside the microchannel geometry are filtered out.

Influence top wall on velocity profile

To investigate the influence of the top wall on the velocity profile in the x,y plane, $\overline{U(y)}$ is measured from z= 25 to 150 μm (figure 5.6 (a) and (b)).

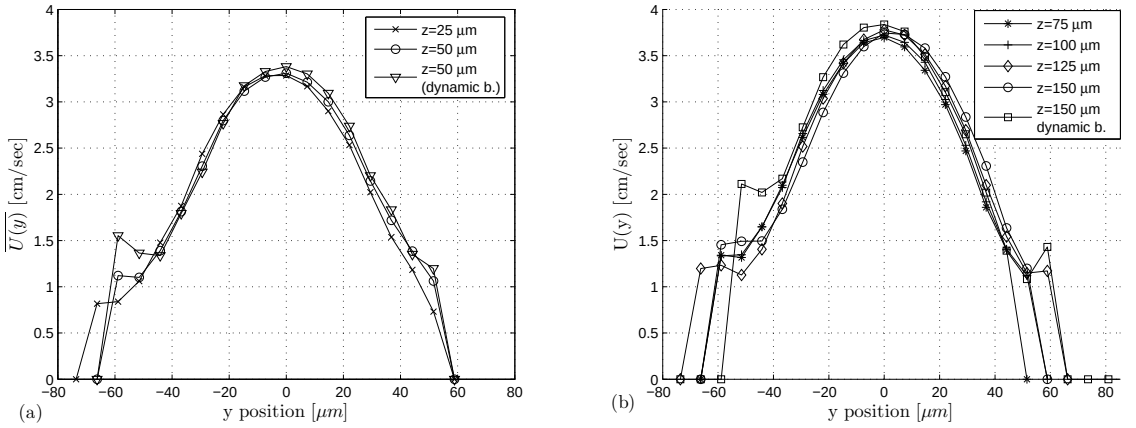

Figure 5.6: Plot of the velocity profile $\overline{U(y)}$ for z=25 and 50 μm (a) and for z=75 to 150 μm (b). Also the velocity profile at z=50 (a) and z=150 μm (b) are plotted, from which the particle images are filtered by a dynamic background filter

As can be seen from figure 5.6 (a) and (b) the shape of the in plane velocity profile is not influenced by the top wall of the microchannel. However the quantity of the in plane velocity measurement, is influenced slightly by the top wall. The maximum velocity $\overline{U_{max}}$ is equal to 3.3 cm/sec for the measurements at z=25 and 50 μm, and equal to 3.75 cm/sec at z=75 to 150 μm. When the velocity profile in z-direction is approximated by a Poiseuille velocity profile, a gradual velocity increase is expected when the measurement depth z is increased. In order to get an impression of the Poiseuille velocity profile as function of z, equation (5.4) is used where L_w is replaced by the depth of the channel L_z (U_{max}= 3.75 cm/sec). According to the Poiseuille equation the velocity U(y=0) should increase from 1.15, 2.1, 2.8, 3.3, 3.65, 3.75 cm/sec when z is increased from 25 μm to 150 μm (with increments of 25 μm).
The background light of 50 image pairs is removed by the dynamic background filter (section 2.5.1) for the velocity measurements at z=50 μm and 150 μm. This is done to investigate if background light caused by out of focus particles results in a decrease of the out of plane resolution and therefore causes this deviation. All light intensity of particle images with an out of focus particle image diameter $d_{p_{\infty_{of}}}$ twice as large as an in focus particle image diameter ($d_{p_\infty} = 6$ pixels) are filtered out. According to equation (2.5), this ensures a correlation depth z_{corr} of 5 μm (ε= $6.25 \cdot 10^{-2}$). As can be seen from figure 5.6 (a) and (b) the removal of the background light for the measurement at z=50 μm and z=150 μm does not result in a quantitatively change of the velocity profiles. In order to determine z_{corr} experimentally, it is recommended to record the particle image diameter $d_{p_{\infty_{of}}}$ of a particle sticked to a microscope glass at an increasing distance z_a to the object plane. On this way can be determined whether z_{corr} corresponds with equation (2.5) and that the calculated out of plane resolution is correct. Most likely this deviation is caused by a measurement error. Therefore is recommended to repeat the measurement.

5.4 Micro Flow in a sinusoidal channel

Next to the μPIV measurement with the rectangular channel a measurement with a sinusoidal channel is carried out. The measured velocity profile is compared with a numerical solution to the micro flow field. First of all the numerical model is described. Subsequently the measurement method and experimental results are given and compared to the numerical determined flow field.

5.4.1 Numerical model

To validate the measurements on the sinusoidal channel, a stationairy numerical model is set up in de the finite element package "COMSOL". The number of elements is reduced, by approximating the 3D sinusoidal microchannel by a 2D geometrie. By means of the 2D geometry, the velocity $\overline{U(y)}$ and $\overline{V(y)}$ in the x,y plane are computed. Therefore is assumed that the bottom and top wall have no big influence on the fluid flow. This is not fully correct because the depth of the microchannel (100 μm) is smaller than the width of the microchannel (200 μm). Due to computational limitations of the 32 bit platform and excessive calculation times for a 3D model, it is chosen to model the microchannel by a 2D geometry. The geometry of the 2D numerical model is determined by an image taken from the sinusoidal microchannel at the measurement depth (between z =25 and 50 μm). In figure 5.7 the geometry of the sinusoidal microchannel model is presented, together with the numbering of the subdomains (indicated by S) and boundary's (indicated by B).

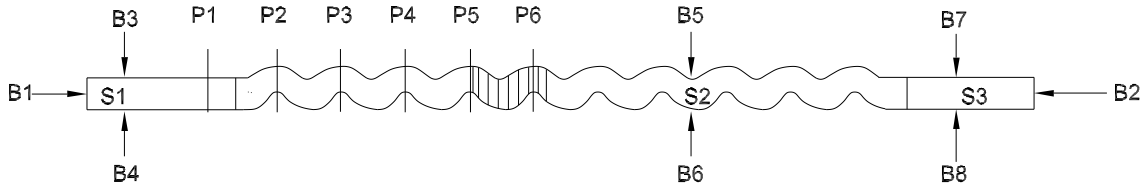

Figure 5.7: Geometry of the sinusoidal microchannel, where the boundary's are indicated by B and the subdomains by S. The lines P1 to P6 indicate the position at which $\overline{v(y)}$ is plotted in figure 5.11. The velocity field $\overline{v(y)}$ of the hatched area is plotted in figure 5.10.

.

The flow in subdomain 1 to 3 inclusive, is described by the Continuity equation and Navier Stokes equation presented in section 5.3.1. The following conditions are prescribed at the boundary's of the microchannel:

1. The inlet velocity at B1, $\underline{u} = u_o$
2. Normal flow or pressure at B2, $p = p_o$
3. No slip condition at B3 to B8 inclusive, $\underline{u} = 0$

The Navier Stokes equation and Continuity equation are solved with "La grange p2-p1" element type.

5.4.2 Measurement method

The deionized water flow through the sinusoidal microchannel, is also generated with the fluid system described in section 5.3.2. At the inlet of the fluid system a constant volume flux of 10 ml/hr is delivered. The sinusoidal microchannel device consists of 1 channel, instead of 75 channels for the rectangular channel. The sinusoidal section of the microchannel consists of 10 periods with each a length of 400 μm. For an overview of the sinusoidal microchannel device, see figure 5.8.

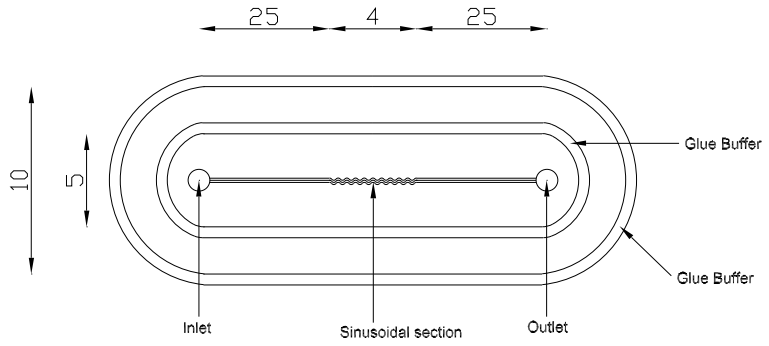

Figure 5.8: Overview of the sinusoidal microchannel with a straight inlet channel and a sinusoidal section in the mid. Around the microchannel are milled two glue buffers, to prevent that glue from the outside reaches the microchannels. The dimensions are in millimeters.

The fluid flows in at the straight section of the microchannel, where it reaches the sinusoidal geometric channel after 25 mm. Due to the milling process the sinusoidal microchannel deviates from a real sinus. On top of the polycarbonate substrate a glass plate is glued. The two channels around the microchannel prevent that glue reaches the microchannels. The microchannels are v-shaped in z-direction due to the v-shaped milling tool. The velocity vectors are also calculated with the software package PIV VIEW 3.4 and an interrogation window of 32x32 pixels with an overlap of 50 %. Particles of the manufacturer Duke scientific with a diameter of 2 μm, are used to visualize the flow. The velocity U(y) and V(y) is measured during a period of 30 seconds, which corresponds with 450 image pairs. The mean velocity in time $\overline{U(y)}$ and $\overline{V(y)}$ is also calculated over the last 20 seconds of the experiment.

5.4.3 Results

Inlet velocity

By a μPIV measurement at position P1 (see figure 5.7), the velocity $\overline{U(y)}$ at the straight inlet of the microchannel is determined. The uniform velocity u_o at boundary B1, is calculated by using conservation of mass together with the mean velocity $\overline{U_{mean}}$ measured at position P1.

$$\rho u_o W = \rho \overline{U_{mean}} W \quad ; \quad u_o = \overline{U_{mean}} \quad ; \quad \overline{U_{mean}} = 0.85 \text{ cm/sec} \tag{5.6}$$

Where the mean velocity $\overline{U_{mean}}$ is calculated according to equation (5.7).

$$\overline{U_{mean}} = \frac{1}{y} \int_0^{L_w} \overline{U(y)} dy \tag{5.7}$$

With L_w the width of the sinusoidal microchannel (200 μm). In figure 5.9 the measured and numerical determined velocity profiles $\overline{U(y)}$ are plotted, along the line at position P1 (see figure 5.7). The numerical and measured velocity profile's U(y) are fully developed, at position P1. As is seen from figure 5.9, the measured and numerical determined velocity profile match well.

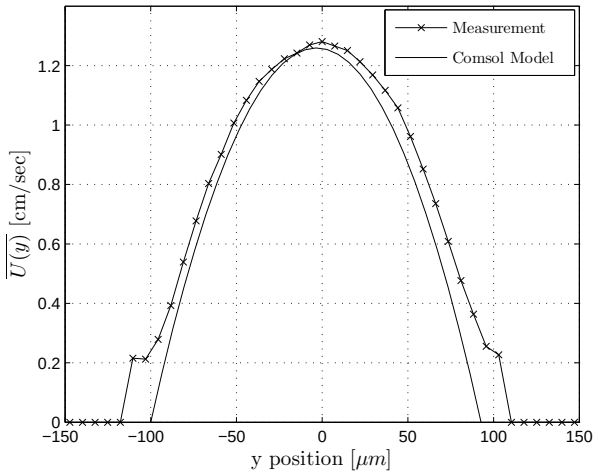

Figure 5.9: Fully developed velocity profile $\overline{U(y)}$, determined by a μPIV measurement and numerical model at position P1 (see figure 5.7).

Numerical and measured velocity field

In figure 5.10 (a) and (b), the measured and numerical determined velocity field $\overline{\mathrm{v(y)}}$ are presented for the hatched area in figure 5.7.

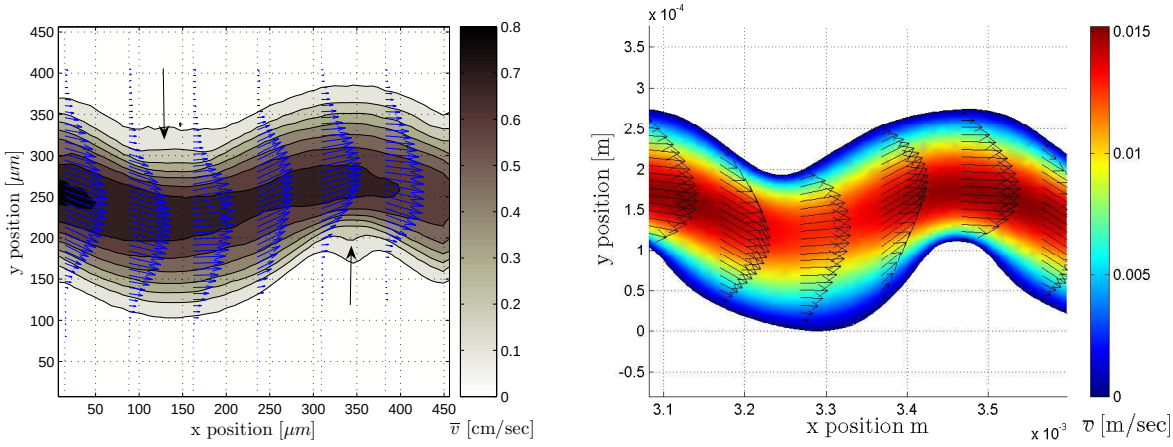

Figure 5.10: Numerical and measured contourplot combined with a vectorplot of the velocity field $\overline{\mathrm{v(y)}}$ in the hatched area depicted in figure 5.7.

The vectors plotted inside the channel show that the shape of the numerical and measured velocity profile $\overline{v(y)}$ match qualitatively well along the channel geometry. However the width of the contourplot and the magnitude of the measured velocity field $\overline{v(y)}$ deviate. The width of contourplot especially deviates at the positions depicted by the leaders in figure 5.10. At these positions the flow of blurred particles outside the microchannel (between the polycarbonate substrate and glass cover) results in outliers.

Velocity decrease

In figure 5.11 the velocity $\overline{\mathrm{v(y)}}$ along the lines marked with P2 to P6 (see figure 5.7) is plotted, in order to investigate the cause of the decreased magnitude of the measured velocity.
Considering the velocity profile computed by the numerical model for line P2 to P6, it is obvious that the velocity profile stays equal and therefore mass is conserved. For the measured velocity $\overline{v(y)}$ however, the maximum velocity decreases gradually from 1.2 to 0.7 cm/sec. An explanation for this decrease in velocity, is that fluid partially flows out the sinusoidal microchannel and fills up the space between the polycarbonate substrate and glass cover which is created by the thickness of the glue layer (figure 5.11(b)). Which means that mass inside the sinusoidal microchannel is not conserved, resulting in a decreased velocity. By taking the coefficient of the constant delivered volume flux and the cross sectional area of the microchannel, the expected bulk velocity at the inlet the microchannel (0.18 m/sec) is calculated. The expected bulk velocity is approximately 20 times higher compared to the mean velocity measured at P1. This subscribes that a large part of the fluid flows out or even not enters the microchannels, during the experiment. Also during the experiments is observed, that the space between the polycarbonate substrate and glass plate (and even the glue buffers) was filled with fluorescent seeding. The height of this space is estimated during the experiment to be about 10 μm.

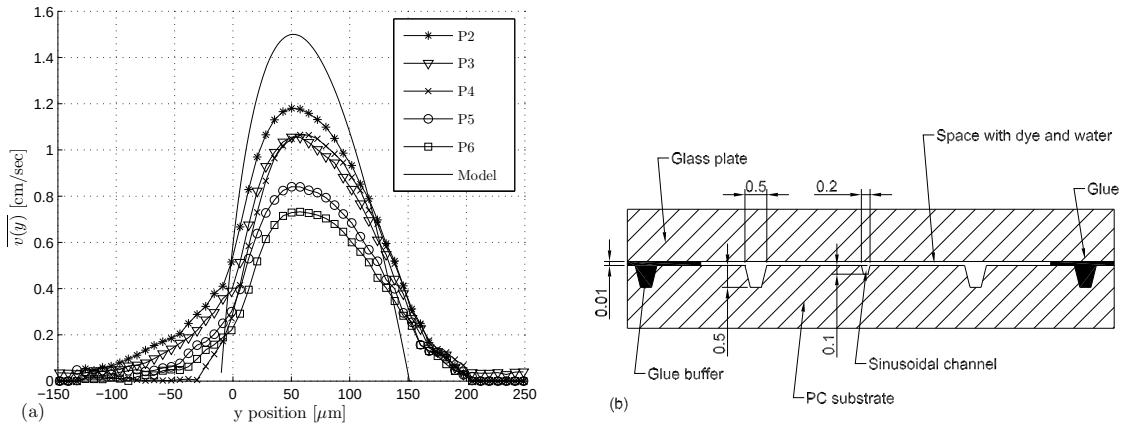

Figure 5.11: Plot of the numerical and measured velocity $\overline{v(y)}$ along the lines marked with P2 to P6 in figure 5.7(a). Cross section of the sinusoidal microchannel device, depicted in figure 5.8 (b). The dimensions are in millimeter.

Comparison of numerical and measured velocity

To determine the accuracy of the μPIV measurement, the measured and numerical determined velocity profiles along 4 lines in the hatched area are compared. An overview of the positions of line A1 to A4 is given in figure 5.12.

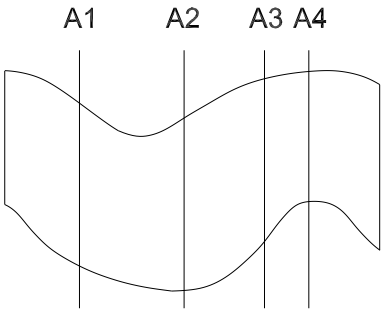

Figure 5.12: Position numbering of the 4 lines, from which the measured and numerical velocity $\overline{\mathrm{v(y)}}$ is compared in figure 5.13, 5.14 and 5.14.

.

When the velocity u_o at boundary B1 is adjusted from 0.85 cm/sec to 0.42 cm/sec, the magnitude of the numerical and measured velocity $\overline{\mathrm{v(y)}}$ at position A4 become equal. By decreasing the velocity u_o, the loss of mass in the measurement is compensated. The velocity profiles along the lines A1 to A4 are plotted in figure 5.13 to 5.15.

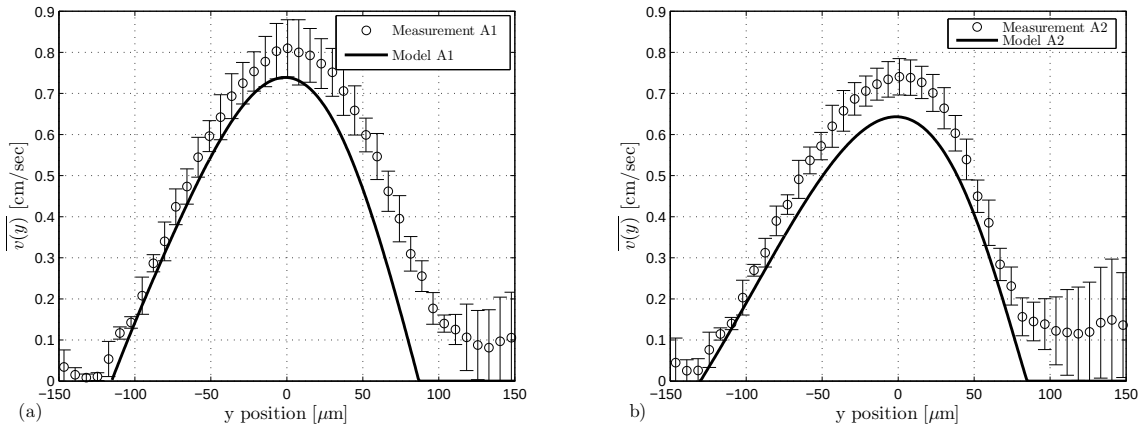

Figure 5.13: Plot of the numerical and measured velocity profile $\overline{\mathrm{v(y)}}$ along A1 and A2 in figure 5.12.

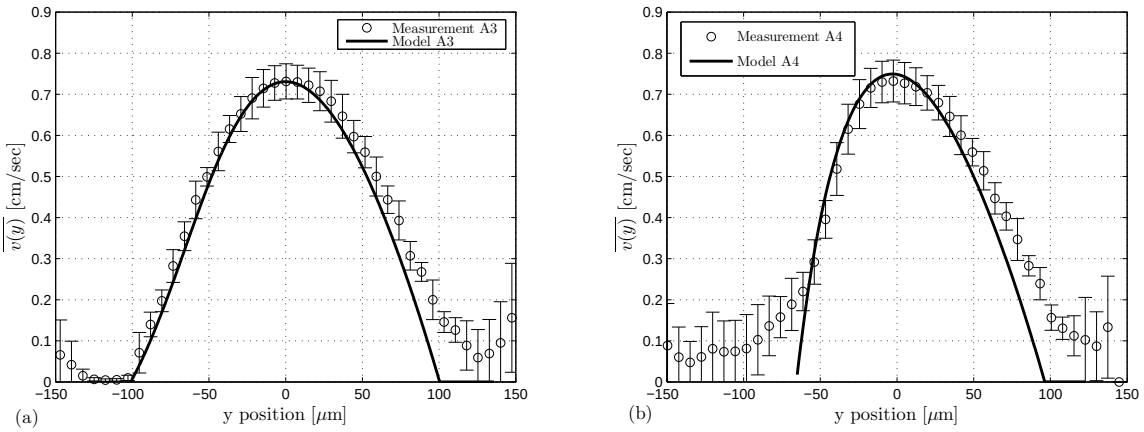

Figure 5.14: Plot of the numerical and measured velocity profile $\overline{\mathrm{v(y)}}$ along A3 and A4 in figure 5.12.

From figure 5.13 and 5.14 it is clear that the numerical and measured velocity profile $\overline{\mathrm{v(y)}}$ match well for the inner region. In the outside region mostly outliers are calculated, just like the rectangular channel. The standard deviation depicted by the errorbars, is again the largest at the outside of the velocity profile. Also it is visible that the measured velocity becomes equal or smaller than the numerical determined velocity profiles $\overline{\mathrm{v(y)}}$ in figure 5.14 (a) and (b). Because mass is conserved in the numerical simulation, it can be concluded that fluid flows out the microchannel along the trajectory of the sinus.
To investigate if the numerical and measured velocity in x and y-direction match, the velocity $\overline{\mathrm{U(y)}}$ and $\overline{V(y)}$ are plotted along the line with position A3 in figure 5.12. Due to the steep wall at position A3, the flow is forced to move upwards. This results according to the numerical model and measurement in a maximum velocity in y-direction of 0.3 cm/sec.

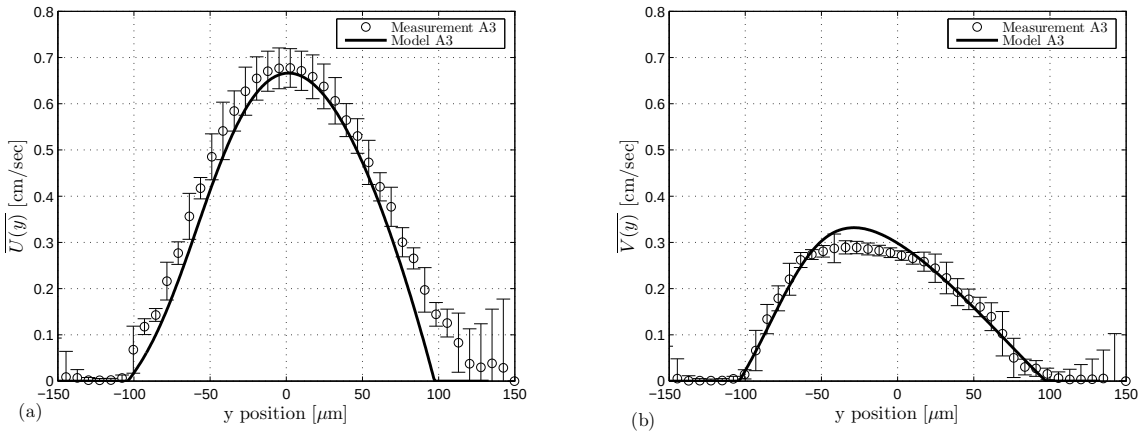

Figure 5.15: Plot of the numerical and measured velocity profile $\overline{\mathrm{U(y)}}$ (a) and $\overline{\mathrm{V(y)}}$ (b) along the line A3 in figure 5.12.

5.5 Conclusions

The μPIV experiments with a rectangular channel show an accurate measured velocity field in the mid domain. The measured velocity in this region, matches perfectly with the analytic solution for a Poiseuille flow between two infinite plates. At the boundary of the measured velocity profile are observed inaccurate velocity vectors. These inaccurate vectors are caused by the low visibility of particles in this region and interrogation windows which overlap an area outside the microchannel device with no particles. Both effects finally lead to bad correlation statistics near the wall. The detectability near the wall (ϵ=1) is therefore much lower than the mid domain (ϵ= 12-61). Before a μPIV is started, it is recommended to record an image of the microchannel geometry. By overlapping the area outside the microchannel geometry by means of a mask, outliers can be removed.
From the in plane velocity measurement with an increasing depth from 25 to 150 μm, it is shown that the velocity profile qualitatively hardly changes for increasing measurement depths. According to the analytic Poiseuille equation, a gradual increase of the velocity is expected when the measurement depth is increased. The background light of the velocity measurements at z=50 and z=150 μm is removed, to investigate if the background light influences the velocity profile $\overline{\mathrm{U(y)}}$. The velocity profile calculated on the basis of the dynamic background filtered images was almost equal to the velocity profile calculated from original images. This means that the background light of out of focus particles hardly influences the in plane velocity measurement. In order to determine the real value of the correlation depth z_{corr}, it is recommended to determine the particle image diameter as function of the out of focus distance. Most likely the deviation between measurement and Poiseuille profile is caused by a measurement error.
The measured velocity field in a sinusoidal geometry matches qualitatively well with the numerically determined velocity field. The magnitude of the measured and numerical determined velocity field deviate due to the loss of fluid in the sinusoidal microchannel. Also outliers are observed in the outer region of the velocity field.

Chapter 6

Conclusions and Recommendations

6.1 Conclusions

A μPIV system based on fluorescence microscopy is developed, to measure flow fields in a microchannel of the order 100 μm with a spatial resolution of 7.36x7.36 μm. The μPIV system is designed to resolve particles with a diameter of 0.86 μm by 4 pixels. The out of plane resolution is 13 and 18 μm, for particles with a diameter of 0.86 and 2 μm respectively. The maximum velocity that can be measured is 3.6 m/sec. For a microchannel with a width of 100 μm, the μPIV system is able to record particle images with a constant visibility to a depth of 150 μm, measured from the top of the microchannel.

The mean gray value of the particle image is risen from 17 to 22, due to the application of particles with a diameter of 2 in stead of 0.86 μm. As a result of the higher gray value, the particle image of the 2 μm particle is better recognizable over the electronic noise of the camera with a mean gray value of 14.
The loss of laser and fluorescent light is investigated, in order to improve the illumination and visualization of the fluorescent particles. Along the optical path of the laser beam, maximum 35 % of the laser light is lost by the diffusor and 20 % by the dichroic mirror. From the emitted fluorescent light by the particles, is lost 40 % by dichroic mirror. A homogeneous laser illumination with a standard deviation of 17 and a mean intensity of 142 in gray values, is achieved. Image distortions as field curvature, pincushion and barrel distortion, vignetting are not present.
As a result of the buoyancy force working on the particle, the particle experiences a velocity of $1.1 \cdot 10^{-5}$ cm/sec in the direction of the gravity. For a relative velocity between the particle and fluid equal to 1 % of the mean fluid velocity in x-direction, the Saffman lift force introduces a velocity towards the middle of the microchannel equal to $3 \cdot 10^{-4}$ cm/sec. Compared to the mean fluid velocity of 2.5 cm/sec, these velocities are negligible. The time constant of the particle respons to a step in the fluid velocity is of the order 10^{-7} sec.

The thermal analysis in which the temperature increase is investigated as a result of the laser illumination on a timescale of 1000 sec, shows that the temperature of the microchannel device increases with 10 K. The temperature peak as a result of a laserpulse with a width of 5 nsec and an energy of 16 mJ, can increase to values far above 1000 K in the first 6 μm of the silicon substrate.

The velocity measurement in a straight and sinusoidal microchannel match qualitatively well with the analytic Poiseuille velocity profile for a flow between two parallel plates and a numerical model. However in the region near the wall of the microchannels the measured velocity profile deviates from the analytic or numerical determined velocity profile. This deviation is caused by, the low particle visibility near the microchannel boundary and interrogation windows which overlap an area outside the microchannel device with no particles. The in plane velocity is measured at a depth of 25, 50, 75, 100, 125, 150 μm in order to investigate the influence of the top wall of the microchannel on the in plane velocity measurement. The measured velocity profiles at the different depths quantitatively deviate from a Poiseuille velocity profile over the depth of the microchannel. The cause of this deviation is most likely a measurement error.

6.2 Recommendations

According the analysis of the μPIV set up and the thermal analysis of the laser, the following items are recommended:

- To improve the image quality, it is recommended to first enhance the visualization part of the μPIV set up. Because of the excessive temperature peaks of the order 1000 K, the microchannel device gets damaged when all laser intensity (16 mJ) is focussed on a small spot of 2 mm.
- In order to optimize the visualization part of the experimental set up, it is recommended to replace the dichroic mirror with a mirror which transmits a higher percentage of the fluorescence intensity. Also it is recommended to purchase a camera with a higher quantum efficiency at the wavelength of the fluorescent particles. The illumination part can be enhanced by choosing a filter which reflects a higher percentage of laser light.
- The best option to obtain a higher visibility, is to decrease the depth of the microchannel from 300 to 150 μm or lower. When the illumination and visualization part of the experimental set up is optimized, it is recommended to decrease the particle diameter to obtain a higher visibility.

According the μPIV measurements, the following items are recommended:

- Before a μPIV experiment is started, it is recommended to record an image of the geometry of the microchannel. The vectors with an error caused by interrogations with a center near or at the microchannel geometry can be removed by overlapping the area outside the microchannel with a mask.
- To determine the out of plane resolution of the μPIV system, it is advised to determine the particle image diameter as function of the distance to the object plane.

Bibliography

[1] Comsol Multhiphysics 3.2, Comsol material library menu

[2] www.dukescientific.com

[3] Eummelen E, Single and two phase microscale cooling, Afstudeerverslag WET 2004-17, Technische Universiteit Eindhoven, 2004

[4] Frijns A.J.H, Rindt C.C.M and van Steenhoven A.A., Micro Heat Transfer, Technische Universiteit Eindhoven, 2006

[5] Gabler J., Modeling temperature measurement of solar cells, WET 2005.20, Technische Universiteit Eindhoven 2005

[6] Hecht E, Optics, fourth edition, Addison Wesley Longman, 2002

[7] Janna W.S., Engineering heat transfer, second edition 2000

[8] Device performance specification KODAK KAI 1010, KODAK KAI 1010M, KODAK KAI 1010CM Image sensors, 2005

[9] Green M.A and Keevers M.J., Optical properties of Intrinsic Silicon at 300K, 1995

[10] Liang-Shih Fan and Chao Zhu, Principles of Gas Solid Flows, The Ohio State University 1998

[11] Olsen M.J. and Adrian R.J., Out of focus effects on particle image visibility and correlation in microscopic particle image velocimetry, Exp. in Fluids vo.29 S166-174, 2000

[12] van der Plas G.A.J., PIV, PTV and HPV user's guide 1.1, Technische Universiteit Eindhoven, 2003

[13] van der Plas G.A.J. and Bastiaans R.J.M., Single and two phase microscale cooling, The FPTVWIZ-algorithm and its validation with synthetic data, Technische Universiteit Eindhoven, 2000

[14] Probstein RF, Physicochemical Hydrodynamics, New York, 1994

[15] Schram P.P.J.M., van Heijst G.J.F., van Dongen M.E.H., Fysische Transportverschijnselen voor Werktuigbouwkunde, 1994

[16] Sharp, K.V. Adian,R.J., Transition from laminar to turbulent flow in liquid filled microtubes, Exp. in Fluids vol.36, (p 741-747), 2004

[17] Siegel R, Net Radiation Method for Transmission Through Partially Transparent Plates, Solar Energy Vol.15 (p. 273-276), 1973

[18] van Steenhoven A.A. and Schreel K.R.A.M., Fysische Meetmethoden, Technische Universiteit Eindhoven, 2002

[19] Sunil Kumar and Kunal Mitra, Microscale Aspects of Thermal Radiation Transport and Laser apllications, Advances in heat transfer 33 (p 187-295) , 1999

[20] Tzou DY, Macro to Microscale Heat Transfer, Missouri, 1997

[21] VDI-Gesellschaft verfahrenstechnik und chemie ingenieursweisen (HRSG), VDI Wärmatlas, Karlsruhe und Düsseldorf 2002

[22] Vedavarz A. and Sunil Kamar M. Karim Moallemi, Significance of Non-Fourier Heat Waves in Conduction, Journal of Heat Transfer 116 (p221-223), 1994

[23] Wereley and Meinhart, Micron-Resolution Particle Image Velocimetry, 2005

[24] Wereley and Meinhart, The theory of diffraction limited resolution in micro particle image velocimetry, Measurements and Science Technology 14 (p. 1047-1053), 2003

Appendix A

Tables

Table A.1: Properties of Selected Materials [7]

Material	Density kg/m^3	Specific heat J/kgK	Thermal conductivity W/mK	Emissivity	Thermal diffusivity m^2/s	Refractive index [-]
Silicon [5]	2330	703	153	0.55	9.34 $\times 10^{-5}$	4.12
Glass [7, 21]	2500	800	0.8	0.88	4 $\times 10^{-7}$	1.5
Teflon [1]	2330	703	153	0.55	9.34 $\times 10^{-5}$	-

Table A.2: Thermal Properties of Air at Atmospheric Pressure (from [7])

Temperature K	Density kg/m^3	Specific heat J/kgK	Kinematic viscosity m^2/s	Thermal conductivity W/mK	Thermal diffusivity m^2/s	Prandtl number Pr
300	1.177	1005.7	15.68×10^{-6}	0.02624	0.22160×10^{-4}	0.708
350	0.998	1009.0	20.76×10^{-6}	0.03003	0.2983×10^{-4}	0.697
307	1.152	1006.16	16.39×10^{-6}	0.02677	0.2323e-4$\times 10^{-4}$	0.706

Table A.3: Experimental parameters

Parameter	Value	Unit	description
λ	612	nm	wavelength of emitting particle
n_{air}	1	[-]	refraction index of air
d_p	0.86 or 2	μm	particle diameter
NA	0.4	[-]	NA of objective lens
M	20	[-]	Magnification optical system
f_o	8	mm	Focal distance of the objective lens
ε	0.01	[-]	relative contribution of out of focus particle ($\varepsilon = 0.01$ means that $d_e(z_{corr}) \approx 3d_e(0)$)
Pixel size	9	μm	
Image array	1000x1000	pixels	
CCD area	9x9	mm	
Inter. window	32x32	pixels	
$L_w x L_z x L_x$	100x300x1500	μm	Dimensions of the microchannel
V_{fr}	0.533	%	Particle volume fraction

Appendix B

List of Symbols

Table B.1: Symbols and Units

symbol	Definition	Unit
A1	Incident angle between perpendicular plane and laser ray	^{o}
A2	Refracted angle between perpendicular plane and laser ray	^{o}
A_v	Area of field of view	m^2
c	Speed of light in silicon	sec
C	Particle concentration	particles/m^3
c_p	Heat capacity	J/kgK
D_a	Aperture of the objective lens	mm
d_p	Particle diameter	μm
d_{e_∞}	Particle image diameter	pixels
$d_{e_{\infty_{of}}}$	Out of focus particle image diameter	pixels
d_{pulse}	Diameter of the laserspot	mm
d_s	Diffraction limited diameter	μm
E_{pulse}	Energy of a single laser pulse	mJ
f_i	Focal distance relay lens	mm
f_k	Gray value distribution of an interrogation window	[-]
f_{laser}	Frequency laser	Hz
f_o	Focal distance objective	mm
fov	Field of view	μm
g	Gravity constant	m/sec^2
I	Intensity of a particle image/laser beam	W/m^2
I_{3D}	Average heat flux pulsating laser	W/m^2
I_b	Intensity of background light	W/m^2
J	Total flux of a particle	W
k	Conductivity	W/mK
L	Characteristic length model	m
L_b	Lower bound gray value distribution	[-]

Symbol	Definition	Unit
L_x	Length microchannel	μm
L_{max}	Maximum in plane particle displacement	μm
L_y	Width microchannel	μm
L_z	Depth microchannel	μm
M	Magnification	[-]
m_f	Mass of fluid displaced by a particle	kg
m_p	Mass of a particle	kg
n_{air}	Refractive index air	[-]
n_{glass}	Refractive index glass	[-]
$n_{particle}$	Refractive index particle	[-]
n_{pulses}	Number of pulses	[-]
n_{water}	Refractive index water	[-]
n_{si}	Refractive index silicon	[-]
$\underline{Q}$	Heat source	W/m^3
$\overline{R\parallel}$	Average reflection for parallel electromagnetic light wave	%
$\overline{R\perp}$	Average reflection for perpendicular electromagnetic light wave	%
s_i	Image distance	mm
s_o	Object distance	mm
t	Time	s
T	Temperature	K
t_c	Propagation time scale	sec
t_d	Diffusion time scale	sec
t_p	Process time scale	sec
dt_{delay}	Time between two laser pulses	μsec
dt_{pulse}	Width of a laserpulse	nsec
U	Fluid velocity in x direction	cm/sec
U_b	Upper bound gray value distribution	[-]
U_p	Particle velocity in x-direction	cm/sec
v	Combined velocity	m/sec
V	Visibility or fluid velocity in Y-direction	[-]
V_{fr}	Particle volume fraction	%
V_p	Particle velocity in y direction	cm/sec
v_{phonon}	Speed of a phonon	m/sec
z	Distance from top of the microchannel to the object plane	μm
z_a	Out of focus distance	μm
z_{corr}	Correlation depth	μm
z_{un}	Unrestricted measurement depth	μm

Table B.2: Greek symbols

Symbol	Definition	Unit
α	Thermal diffusivity	m^2sec
$\alpha_{\text{coeff}_{\text{si}}}$	Absorption coefficient silicon	[-]
α_{silicon}	Absorption factor silicon	[-]
β	Parameters which defines edge particle image	[-]
δ	Thickness object plane	μm
ϵ	Detectability / emission coefficient	[-]
ε	Relative contribution of an out of focus particle	[-]
θ	Angle to optical axis	^{o}
θ_{NA}	Angle to optical axis restricted by NA	^{o}
θ_{k}	Correlation signal or dimensionless temperature	%
ν	Kinematic viscosity water	m^2/sec
λ	Wavelength	nm
μ	Dynamic viscosity water	kg/msec
σ	Stefan Boltzman constant	$\text{W/m}^2\text{K}^4$
ρ	Density water	kg/m^3
ρ_{p}	Density particle	kg/m^3
τ	Time constant or relaxation time	sec
τ_{phonon}	Relaxation time phonon scattering	sec

Table B.3: Vectors

Symbol	Definition
$\underline{\text{u}_{\text{p}}}$	Particle velocity in x and y direction
$\underline{\text{u}}$	Fluid velocity in x and y direction
$\underline{\text{X}}$	Physical coordinates
$\underline{\text{x}}$	Pixel coordinates

Table B.4: Abbrevations

Symbol	Definition
CCD	Charged Coupled Device
LASER	Light Amplification by Stimulated Emission of Radiation
NA	Numerical Aperture
PIV	Particle Image Velocimetry
PTV	Particle Tracking Velocimetry

Appendix C

PIV and PTV

For quantitative whole field velocity measurements on macro scale there are two techniques available: Particle Image Velocity [PIV] and Particle Tracking Velocity [PTV]. Both techniques make use of a laser sheet which illuminates particles seeded in the flow (figure C.1). Particles flowing inside this laser sheet reflect light which is gathered by optics and finally imaged by a Camera. By capturing two images of the seeded particles, the displacement in x and y direction is respectively determined. From the coefficient of the displacement and the time interval between two images, the velocity is finally determined.

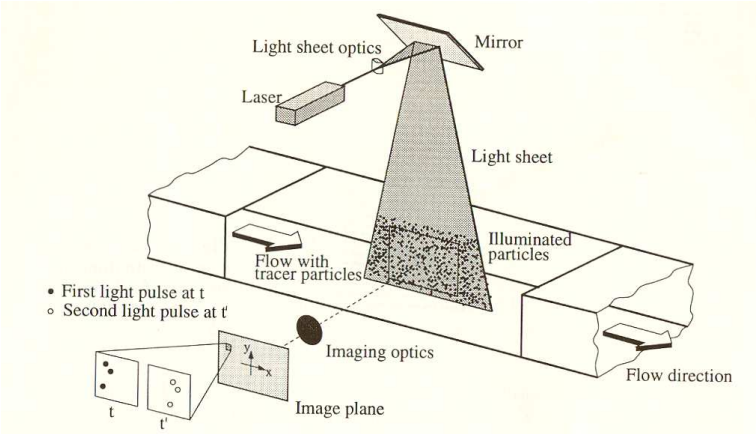

Figure C.1: Experimental set up to perform PIV or PTV in a channel

Main difference between PTV and PIV is the sequence by which the particle images are captured and the way a velocity vector is calculated out of the particle displacement between two images. When PTV is used, particle images are captured with an equidistant time delay between the images (figure C.2 (a)). With PIV, two images are captured within a very short time where another image pair is captured after a longer delay. By means of the two correlating images with a very short time delay, the PIV algorithm calculates over a sector of particles the mean particle displacement (figure C.2 (b)).

The velocity measurement technique PTV, calculates the displacement of each particle individually.

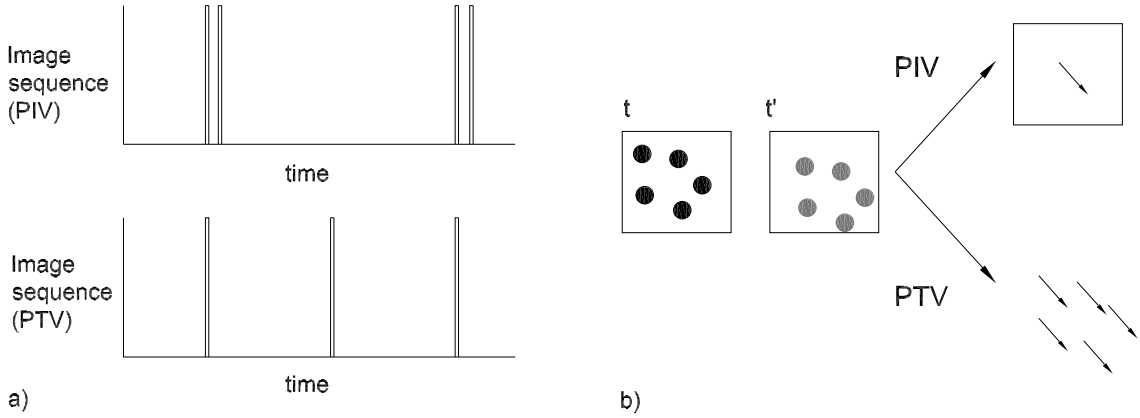

Figure C.2: Difference between PTV and PIV with respect to the sequence by which the particle images are captured (a) and the way velocity vectors are calculated (b)

Because PTV calculates the velocity of each particle individually it reaches a higher spatial resolution with respect to PIV. To compute the velocity of each particle individually the particle at time step t, is matched with the corresponding particle at time step t'. For the matching process a predictor is used, which requires a low particle density and a pixel displacement of about 3 pixels/timestep [18]. The largest error source for PTV, are particle mismatches between two images. With PIV the mean velocity is computed at the midpoint of each sector (interrogation window). This interrogation window therefore determines the spatial resolution. The mean displacement of the particles inside an interrogation window is determined, by using a correlation algorithm described in section 2.5.2.
For measuring velocity profiles on small scale, PIV is the most suited measurement technique. When PIV is used, a velocity vector can be determined out of two images with a intermediate delay of upto 1 μsec. With PTV this short delay between two images is not possible. This technique is limited to a frequency of 30 Hz and a maximum displacement of about 3 pixels between two images. Both the low frequency and small displacement together with the sub-mm measurement plane, leads to a very low dynamic range when PTV is used to measure velocity fields in a microchannel.

Appendix D

Specifications experimental components

D.1 Laser pulse and camera sequence

In order to capture two images with a time delay down to 1 μsec, the Kodak ES 1.0 camera is put in the triggered double exposure mode. The camera signal and laser pulse related to time in triggered double exposure mode, are presented in figure D.1.

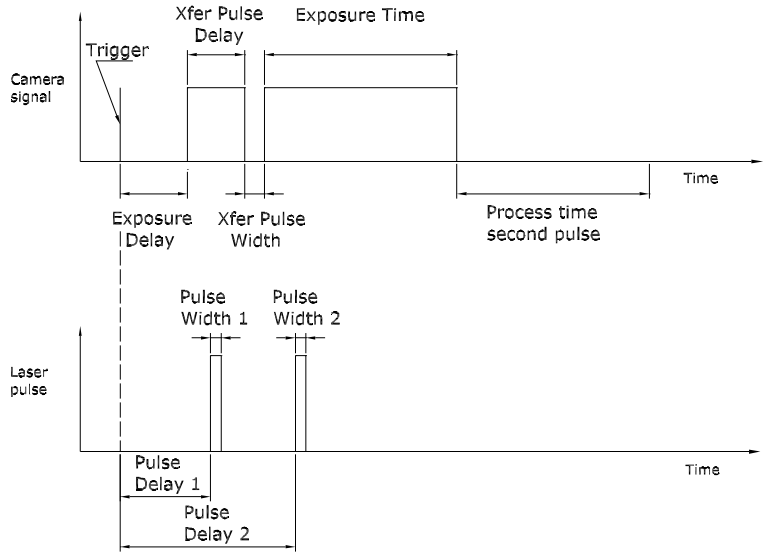

Figure D.1: Camera signal and laser pulse related to time for a triggered double exposure mode.

By activating the triggered double exposure mode, the camera waits for an external signal on the trigger input at the back of the camera. If there is a signal at the trigger input, the camera shutter opens after a fixed "exposure delay time" of 20 μsec. The exposure of the first image, named "Xfer pulse delay" is free adjustable between 1 μsec and 255 μsec in increments of 1 μsec. During this first exposure, a laser pulse of 5 nsec illuminates the object. The amount of time between the exposure of the first and second image is represented by the "Xfer pulse width". This delay can be decreased to 1 μsec. During the second exposure, a laserpulse of 5

nsec illuminates the object again. Due to the same pulse width, the illumination intensity of both images is equal. The exposure time of the second image is always 30 msec. Subsequently, data is processed for a period of 30 msec. After data processing, the camera is able to capture a new pair of images according to the cyclus described above. The time delay of laser pulse 1 and 2 to the external trigger signal, is programmed by the quantity pulse delay 1 and 2 (figure D.1). Each laser pulse can be generated with a maximum frequency of 15 Hz.

D.2 Positioning system

The back of the microchannel device is clamped against a teflon block, which is connected to a μm positioning system (figure D.2 (a) and (b)). This μm positioning system consists out a translation table with an accuracy of 1 μm in z-direction (PT1/M with high precision micro head, THORLABS) and 10 μm in x,y direction (PT1/M with standard micro head, THORLABS). The particles seeded in the flow are illuminated and imaged from the front side by the experimental set. A goniometer (GNL10/M with standard micro head, THORLABS) is used to align the x,y plane perpendicular to the optical axis of the experimental set up.

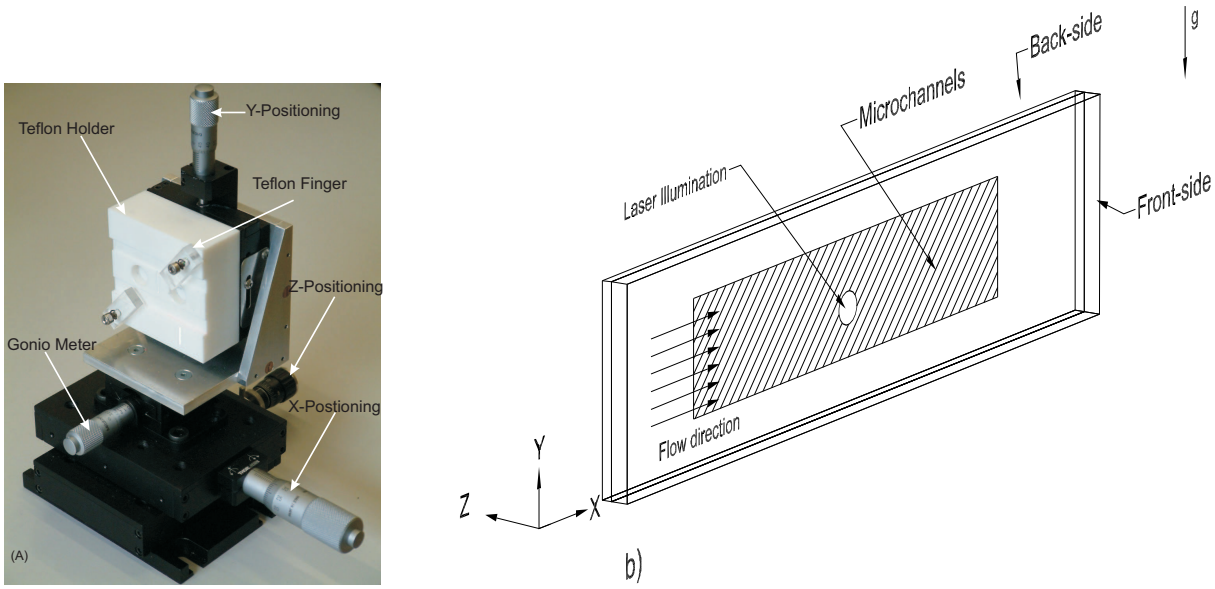

Figure D.2: Picture of the x,y,z stages, goniometer, teflon holder and teflon fingers (a). Schematic of the microchannel device, with a definition of the coordinate system (b). The x,y and z coordinate direction correspond with the x,y,z translation of the positioning tables.

D.3 Seeding

The fluorescent particles exhibit peak sensitivity at a wavelength of 542 nm and a peak emission at 612 nm. The fluorescent particles are excitated at 97 % of their peak excitation by the laser with a wavelength of 532 nm. The density of the particles (1.05 g/cm^3) is almost equal as the density of working fluid water (1 g/cm^3). In figure D.3 the excitation and emission spectra of the fluorescent particles is given.

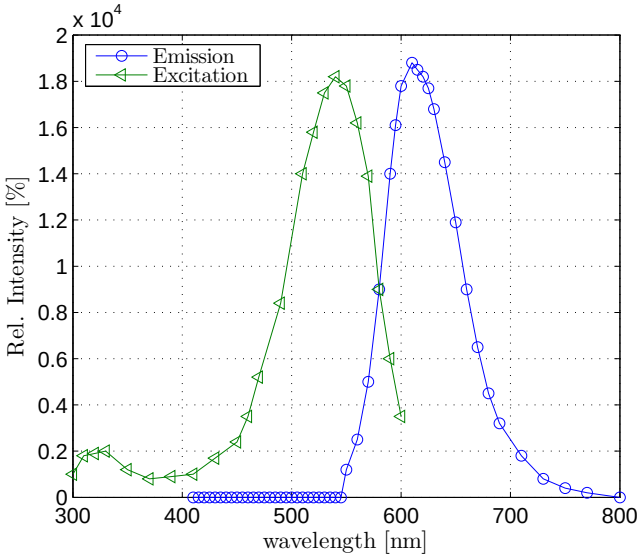

Figure D.3: Excitation and sensitivity peak of Duke scientific's fluorescent particles, used for visualizing velocity profile in micro channels [2].

Other properties of the fluorescent particles are given in table D.1.

Table D.1: Properties of fluorescent particles

Manufacturer	rho kg/m^3	n	d_p μm
Duke-scientific [R900]	1.05	1.59	0.86
Duke-scientific [R200]	1.05	1.59	2

D.4 Calibration grid

To correct sufficiently for image distortions, mapping functions D.1 and D.2 with third order 1D terms [n_o] and third order cross-terms [n_c] can be used.

$$X(x,y) = a + \sum_{i=1}^{n_o}(b_i x^i + c_i y^i) + \sum_{i=1}^{n_c-1}\sum_{j=1}^{n_c-i} d_{ij} x^i y^i \tag{D.1}$$

$$Y(x,y) = a + \sum_{i=1}^{n_o}(b_i x^i + c_i y^i) + \sum_{i=1}^{n_c-1}\sum_{j=1}^{n_c-i} d_{ij} x^i y^i \tag{D.2}$$

With the help of the physical coordinates and the corresponding pixel coordinates of N reference points, it is possible to calculate the M calibration coefficients of the third order mapping functions D.1 and D.2. When least square fitting is used to determine the M calibration coefficients, the condition $M < 2N$ must hold. For third order mapping functions, in total 20 calibration coefficients have to be determined. Considering the condition $M < 2N$, it is needed that a minimum of 10 reference points must lie inside the field of view. The dimensions of the field of view are calculated in subsection 2.4.2. A possible grid which can be used for a calibration with third order mapping functions is presented in figure D.4

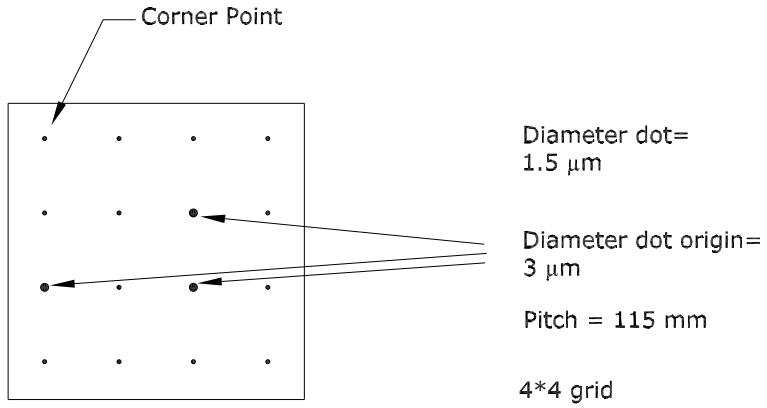

Figure D.4: Appropriate calibration grid for calibration with third order mapping functions.

The grid consists of 16 points which lie inside the field of view, depicted by the frame. Close to the center of the field of view are positioned three larger calibration points with a diameter of 3 μm, which function as reference for the x and y-axis. To clearly recognize a calibration point on the CCD, it must be imaged on 3x3 pixels. For a calibration point with a diameter of 1.5 μm, the effective image diameter becomes according equation (E.7) equal to 45.5 μm. By dividing this effective image diameter with the pixel size of 9 μm, it is easy to see that the calibration point is imaged on 5x5 pixels. The grid can be fabricated by coating a substrate with fluorescent dye with equal excitation and emission properties as the fluorescent particles. At the position of the preferred 16 reference points, the coating can locally be removed with an excimer laser. The exact physical position of these reference points can be determined by electron microscopy.

Appendix E

Particle image diameter and out of plane resolution

In this appendix, equations are derived to calculate the particle image diameter of in focus and out of focus particle. By combining both of these equations an equation is derived for the out of plane resolution of the experimental set up. For the derivation of all these equations the analysis of Wereley and Meinhart [23] is followed.

E.1 Derivation

In the case a point source is imaged through a pinhole, diffraction plays an important role. The diffraction limited spot size of a point source, such as a light emitting particle, can be calculated according to equation (E.1).

$$d_s = 2.44 s_i \frac{\lambda}{D_a} \tag{E.1}$$

where d_s is the diffraction limited spot size, s_i the image distance, λ the wavelength of the emitting particle, D_a the diameter of the pinhole. The particles in the microchannels are imaged by an infinity corrected lens system, see figure E.1.

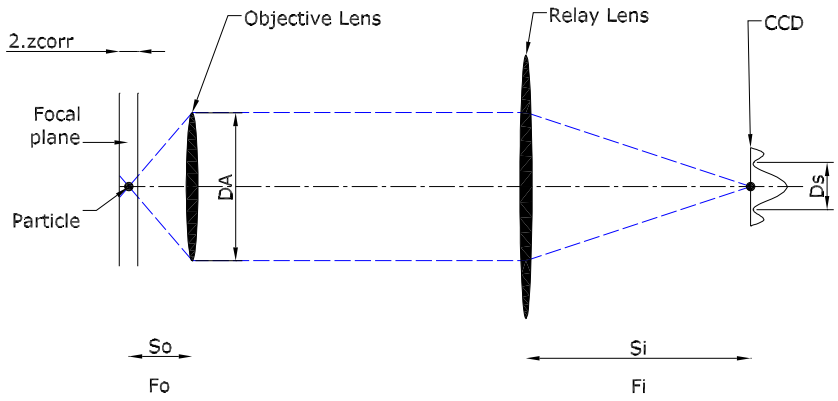

Figure E.1: Schematic of the infinity corrected lens system, with the used parameters for the spatial resolution calculation.

In order to calculate the diffraction limited spot size, resulting from imaging a particle with an infinity corrected optical system, equation (E.1) has to be adapted. This is done by making use of equation (E.2), which holds for an infinity corrected optical system [24].

$$M = \frac{s_i}{s_o} = \frac{f_i}{f_o} \tag{E.2}$$

with s_o the object distance, f_i focal length of the relay lens, f_o focal length of the objective and M the magnification. Substituting equation (E.2) in equation (E.1) yields:

$$d_{s_\infty} = 2.44 M \lambda \frac{f_o}{D_a} \tag{E.3}$$

with D_a the aperture diameter of the lens and d_{s_∞} the diffraction limited spot size for an infinity corrected optical system. Most of the lenses are classified by the numerical aperture [NA], which is a quantity to denote the light gathering abilities of a lens. Higher numerical aperture, means a better ability to resolve fine details and a smaller depth of focus. The numerical aperture is calculated by equation (E.4).

$$NA = n_{air} \sin(\theta_{NA}) \tag{E.4}$$

where n_{air} is the refractive index of the medium between the object and the objective lens, θ_{NA} defined as half the light collecting angle of the lens (see figure E.2).

Equation (E.3) however contains the focal number [f* – number] defined as $f^* = \frac{f_o}{D_a}$. Therefore a relationship between the f^* – number and NA is needed [24].

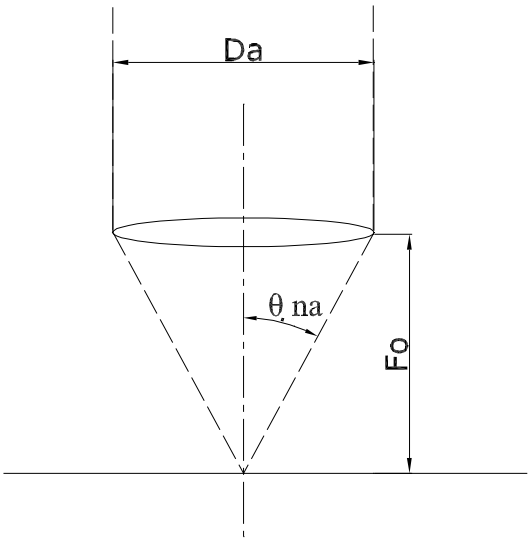

Figure E.2: Definition of θ_{NA} and a schematic of the light gathering cone used in equation (E.4).

$$f^{*} = \frac{1}{2}[(\frac{n_{air}}{NA})^2 - 1]^{\frac{1}{2}} \tag{E.5}$$

With the help of relationship E.5, equation (E.3) can be written in the following form.

$$d_{s_\infty} = 1.22M\lambda[(\frac{n_{air}}{NA})^2 - 1]^{\frac{1}{2}} \tag{E.6}$$

In order to calculate the image diameter, d_e, equation (E.7) is used [23].

$$d_e = \sqrt{M^2 d_p^2 + d_{s_\infty}^2} \tag{E.7}$$

Combining equation (E.6) and (E.7), yields to equation (E.8) which can be used for the calculation of the image diameter for an infinity corrected optical lens system.

$$d_{e_\infty} = [1.49M^2\lambda^2((\frac{n_{air}}{NA})^2 - 1) + M^2 d_p^2]^{\frac{1}{2}} \tag{E.8}$$

To account for the geometric spreading for a slightly out of focus particle [23] a third term is added. So the image diameter for a particle which is slightly out of focus, can be written as.

$$d_{e_{\infty_{of}}} = [1.49M^2\lambda^2((\frac{n_{air}}{NA})^2 - 1) + M^2 d_p^2 + \frac{M^2 D_a^2 z_a^2}{(f_o + z)^2}]^{\frac{1}{2}} \tag{E.9}$$

where z_a is the axial distance of the particle to the object plane. To determine the out of plane resolution, the term z_{corr} is defined. This is the axial distance to the focal plane in which a particle is out of focus and no longer contributes to the peak detection of the correlation function (see figure E.1). The relative contribution, ε, of a particle which is out of focus can be defined as [23].

$$\varepsilon = \frac{d_{e_{\infty_{of}}}(z_a = 0)^4}{d_{e_{\infty_{of}}}(z_a = z_{corr})^4} \tag{E.10}$$

With the assumption $z_a << f_o$ it is valid to say that, $\frac{D_a^2}{(f_o+z_a)^2} \approx \frac{D_a^2}{f_o^2} = 4[\frac{n_{air}^2}{NA^2} - 1]^{-1}$. By combining equation (E.10) and (E.9), expression (E.11) is derived.

$$z_{corr} = \frac{1}{2}[\frac{1-\sqrt{\varepsilon}}{\sqrt{\varepsilon}}(\frac{n_{air}^2}{NA^2} - 1)(d_p^2 + 1.49\lambda^2(\frac{n_o^2}{NA^2} - 1))]^{1/2} \tag{E.11}$$

Appendix F

Influence preprocess techniques

F.1 Effect dynamic threshold and contrast enhancement

The influence of dynamic thresholding and contrast enhancement on the gray value distribution of an in focus particle image is investigated. When the grey value distribution of the image particle is changed due to dynamic thresholding or contrast enhancement, it will influence the calculation of the mean displacement according to cross correlation. The contourplot of particle image and a contrast enhanced particle image is given in figure F.1. The particle diameter is 2 μm.

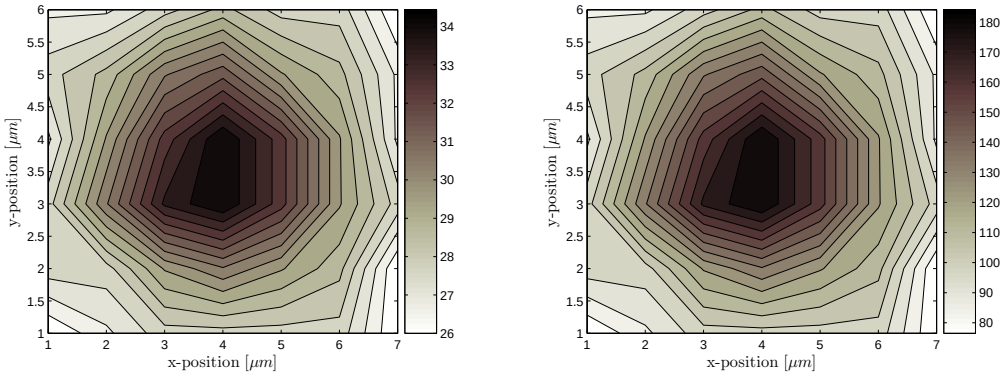

Figure F.1: Contourplot of a particle image with the original (a) and enhanced grey value contrast distribution (b) .

The contrast of the original particle image is enhanced with Ub and Lb of 40 and 20 respectively. As can be see from figure F.1 (a) and (b), the shape of the particle image is not influenced by contrast enhancement. Therefore contrast enhancement will not affect the displacement calculation by means of cross correlation.

The influence of dynamic thresholding is illustrated by means of figure F.2. In this figure the gray value distribution along the diameter of a particle image is plotted, for an original and dynamic thresholded particle image. In the original particle image a mean background intensity of 25 is present, due to out of focus particles.

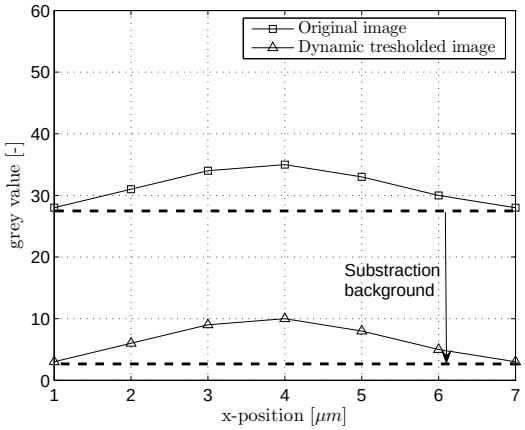

Figure F.2: Grey value along the diameter of a original particle image and a particle image from which the background light is removed by a dynamic background filter.

Due to the dynamic background filter the gray values of the original particle image are decreased with 25. The shape of both particle images is equal and therefore the displacement calculated by cross correlation is not influenced.

Appendix G

Visibility

In this appendix the equation is derived to determine the visibility of particles imaged by an infinite corrected lens system. The derivation is carried out according to the analysis of Wereley, Meinhart [23] and Olsen, Adrian [11].
The flux of a particle which reaches the image plane can calculated according to equation (G.1).

$$J(z_a) = \frac{J_p D a^2}{16(f_o + z_a)^2} \tag{G.1}$$

where J_p is the total flux emitted by a particle and is dependent on the illumination intensity, D_a is the aperture of the object lens, f_o the focal distance of the object lens, z_a the axial distance of the particle to the object plane. The light intensity of a particle image can be approximated as a gaussian function:

$$I(r) = I_o exp(\frac{-4\beta^2 r^2}{d_e^2}) \tag{G.2}$$

where the r is the radial distance to the center, d_e the particle image diameter, β the parameter which defines the edge of the particle image. According to Adrian and Yoa [], the gaussian equation (G.2) approximates the best an airy distribution with β^2=3.67. The total light flux of the particle image can be calculated by equation.

$$J = \int I(r) dA \tag{G.3}$$

At an axial distance z_a from the object plane must hold that the total light flux $J(z_a)$ is equal to the total flux of the particle image J. By this equality the parameter I_o in equation (G.2) is determined, which yields:

$$I_{r,z_a} = \frac{J_p D_a^2 \beta^2}{4\pi d_e^2 (f_o + z_a)^2} exp(\frac{-4\beta^2 r^2}{d_e^2}) \tag{G.4}$$

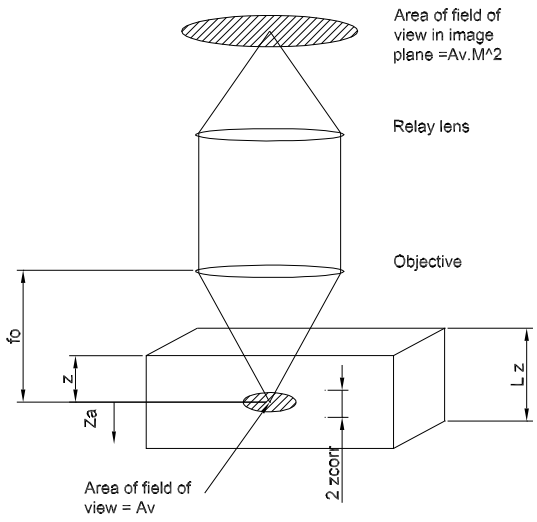

Figure G.1: Channel geometry used in the derivation of the visibility

By assuming that particles with a distance $z_a >> z_{corr}$ as out of focus and contributing homogeneously to the background intensity and particles between 2 z_{corr} as completely in focus, the total light flux of the background light, J_b, can be calculated by

$$J_b = A_v C\{\int_{-z}^{-z_{corr}} J(z_a)dz_a + \int_{z_{corr}}^{L_z - z} J(z_a)dz_a\} \quad ; \quad J_b = \frac{C J_p L_z D_a^2 A_v}{16(f_o - z)(f_0 - z + L_z)} \tag{G.5}$$

By dividing equation (G.5) through M^2 and A_v, the background intensity, I_b, at the image plane becomes:

$$I_b = \frac{C J_p L_z D_a^2}{16 M^2 (f_o - z)(f_0 - z + L_z)} \tag{G.6}$$

where C is the number of particles per unit volume, L_z is the depth of the microchannel, A_v is the field of view area and M is the magnification. The particle visibility can be derived by dividing the intensity of an in focus particle $I(0,0)$ through the background intensity I_b and replacing d_e with equation (E.8).

$$V = \frac{I(0,0)}{I_b} = \frac{4M^2\beta^2(f_o - z)(f_o - z + L_z)}{\pi C L_z f_o^2 (M^2 d_p^2 + 1.49 M^2 \lambda^2((\frac{n_{air}}{NA})^2 - 1))} \tag{G.7}$$

By multiplying equation with the volume of a particle, the visibility V can be calculated as function of the volume fraction V_{fr} by

$$V = \frac{I(0,0)}{I_b} = \frac{2 d_p^3 M^2 \beta^2 (f_o - z)(f_o - z + L_z)}{3 V_{fr} L_z f_o^2 (M^2 d_p^2 + 1.49 M^2 \lambda^2((\frac{n_{air}}{NA})^2 - 1))} \tag{G.8}$$

Appendix H

Optical analysis

H.1 Refraction

Light rays emitted by the particles in the micro channels pass successively through water, glass and air. The light paths of an object with only air and air-glass-water as intermediate media are drawn in figure H.1.

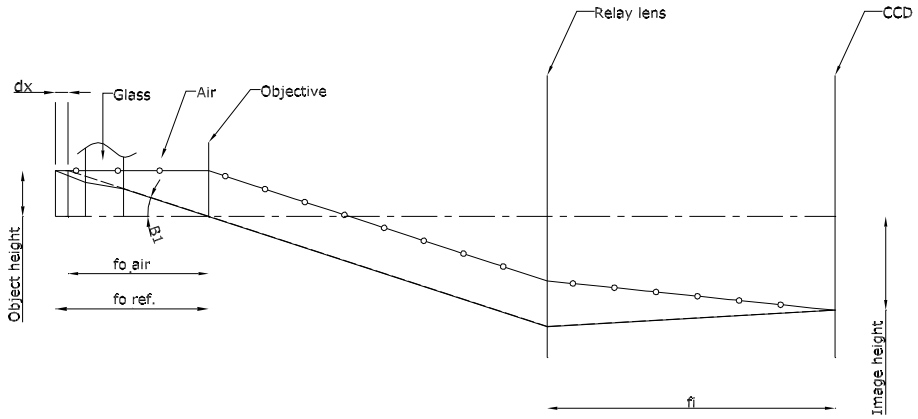

Figure H.1: Schematic ray tracing for an object imaged by an infinite corrected lens system. The dashed and solid line represent the light path for only air and air-glas-water as intermediate respectively. Both light rays start at the top of the object and cross the objective in the center.

Due to the refraction of glass and water, the focal distance (fo_{air}) increases with dx. Because the angle B1 does not change for both light paths, the image height and therefore the magnification is not influenced by the refraction of glass and water. Where the magnification in this case is defined as the coefficient of the object and image height.

H.2 Vignetting

Vignetting is the difference of light intensity for points with difference distances to the optical axis. From the top of the micro channel only light with a small angle Θ_2 compared to an angle Θ_3 reaches the CCD. This is shown in figure H.2, in which the light ray paths of the top and center of the micro channel are drawn.

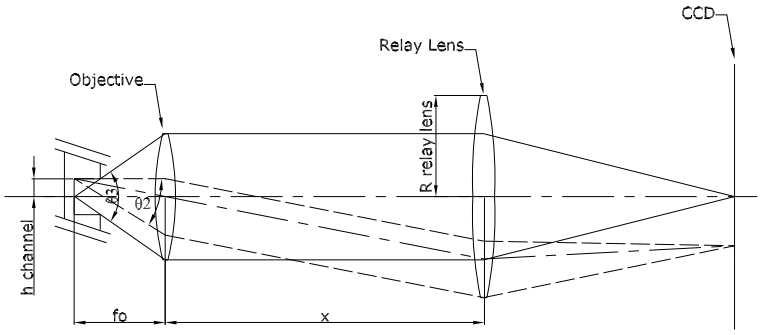

Figure H.2: The effect of vignetting on the light intensity of the image.

The smaller angle of light gathered from the outsides of the micro channel is caused by two factors:

1. The top and bottom edge of the micro channel restrict light rays paths going towards the objective lens.
2. Light rays coming from the outside of the micro channels who reach the outside of the objective lens, are not gathered by the relay lens. This factor can be minimized by decreasing the distance between the objective lens and relay lens as far as possible or by increasing the diameter of the relay lens in such way, that all light rays coming from the outside of the objective lens are gathered.

As can be seen from figure 3.6, the particle images at the outside of the image are not lowered in intensity.

H.3 Perspective error

As a result of an out of plane velocity component, an perspective error is introduced in the in plane velocity measurement. Regarding the μPIV experiment, an out of plane velocity component is especially present in the boundary layer of the top and bottom wall of the microchannel. The perspective error is explained by means of figure H.3.

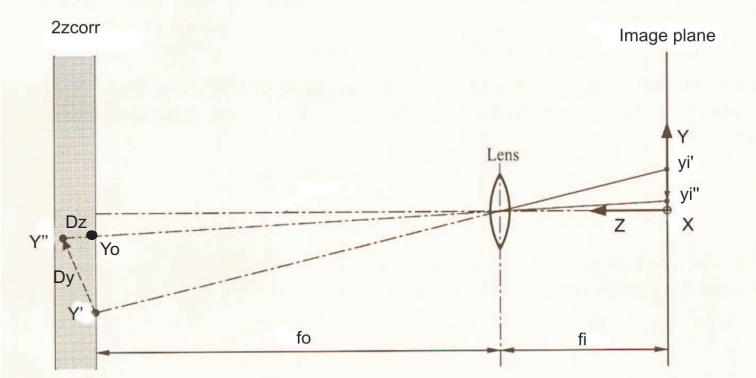

Figure H.3: Schematic depicting the effect of perspective error on the in plane velocity measurement.

As can be seen in figure H.3, is the displacement of a particle with an out of focus velocity component detected as a displacement $Y_0 - Y'$ instead of the real displacement dY. When the out of plane displacement (Dz) is for example limited to 1/4 of L_{max}, the relative in plane velocity error (ε_p) caused by perspective is

$$\varepsilon_p = (1 - \frac{Yo - Y'}{dY})100 = 3\% \tag{H.1}$$

H.4 Positive and negative image distortion

Positive and negative distortion can be recognized as curvature deformation of the image. Positive distortion (figure H.4 (a)), is caused by a higher magnification on the optical axis as on the off axis. When the magnification off axis is larger than on the optical axis, the image curvature is called negative distortion (figure H.4 (b)).

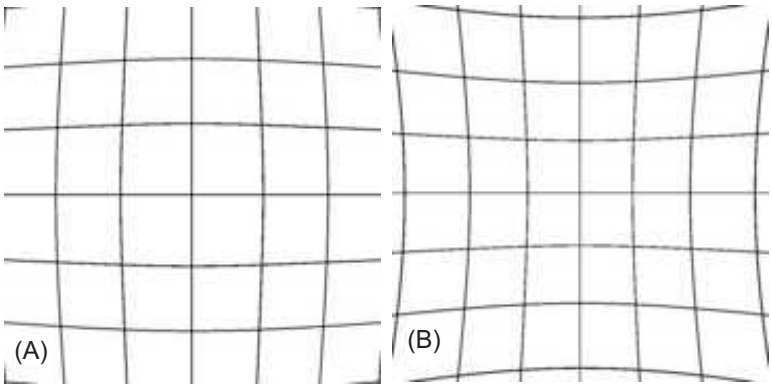

Figure H.4: Effect of positive (a) and negative (b) distortion on an image.

Appendix I

Macro- to Microscale Heat Transfer

I.1 Introduction

The following models to describe heat transfer on micro or macro scale are studied:

- Diffusion model:

$$\frac{\partial \mathrm{T}}{\partial \mathrm{t}} = \alpha \nabla^2 \mathrm{T} \tag{I.1}$$

- Catteneo and Vernotte [CV] wave model:

$$\frac{1}{\alpha}\frac{\partial \mathrm{T}}{\partial \mathrm{t}} + \frac{1}{\mathrm{C}^2}\frac{\partial^2 \mathrm{T}}{\partial \mathrm{t}^2} = \nabla^2 \mathrm{T} \quad ; \quad \text{with } \mathrm{C} = \sqrt{\frac{\alpha}{\tau_\mathrm{r}}} \tag{I.2}$$

- Phonon scattering model:

$$\nabla^2 \mathrm{T} + \frac{9\tau_\mathrm{n}}{5}\frac{\partial}{\partial \mathrm{t}}(\nabla^2 \mathrm{T}) = \frac{3}{\tau_\mathrm{r} \mathrm{c}^2}\frac{\partial \mathrm{T}}{\partial \mathrm{t}} + \frac{3}{\mathrm{c}^2}\frac{\partial^2 \mathrm{T}}{\partial \mathrm{t}^2} \tag{I.3}$$

Where heat transfer by diffusion, is the classical theorie to describe heat transfer on macro time and length scales. The solution of the diffusion equation is parabolic.
The CV wave model, predicts the temperature on small time scales of the order equal to relaxation time [τ_r] of the material. For silicon the relaxation time is of the order femtoseconds and smaller [22]. The wave equation, depicts that a temperature disturbance propagates as a thermal wave, with a finite wave speed [C]. Wave damping in time is described, by the thermal diffusivity [α].
For the semiconductor silicon (which absorbs all the laser energy) phonon scattering is the dominant heat transfer mechanism. To describe heat transfer on micro length and time scales by phonon scattering, the phonon scattering model can be used. Where τ_n is the relaxation

time in which momentum is conserved in the phonon system, τ_r the relaxation time in which is momentum is lost from the phonon system and c the speed of phonons in matter. Due to the presence of a mixed derivative term, $\frac{\partial}{\partial t}(\nabla^2 T)$, the solution of the phonon scattering model is of a parabolic nature. The thermal wave propagation induced by the wave term, $\frac{\partial^2 T}{\partial t^2}$, is destroyed by the mixed derivative term.

I.2 Lagging behavior

To make clear the differences between the three models, the term lagging behavior has to be explained. Lagging behavior, describes the presence of a heat flux and temperature gradient at different instants of times. To prescribe heat flux and temperature gradient in time, the time delay of the heat flux $[\tau_q]$ and the time delay of the temperature gradient $[\tau_T]$ are introduced. Where the delay of the heatflux describes thermal inertia in short time response and temperature gradient delay describes the delay caused by heat transfer mechanisms occuring on micro scales. In case the heat flux occurs before any temperature gradient $[\tau_q < \tau_T]$, the heat flux is the cause and the temperature gradient the effect. If the temperature gradient precedes the heat flux $[\tau_T < \tau_q]$, the temperature gradient is the cause and the heat flux the effect.
By making use of this lagging behavior, it's possible to derive a general equation, by which the classical theorie of diffusion, CV waves and phonon scattering can be captured [20]. This general equation, with τ_q and τ_T is given by equation (I.4).

$$\frac{1}{\alpha}\frac{\partial T}{\partial t} + \frac{\tau_q}{\alpha}\frac{\partial^2 T}{\partial t^2} = \nabla^2 T + \tau_T \frac{\partial}{\partial t}(\nabla^2 T) \tag{I.4}$$

By taking different value's for τ_q and τ_T, it's possible to capture the several models presented in section I.1.

- In case the two delays are equal, $\tau_q = \tau_T$, equation (I.4) reduces to the equation which describes heat transfer by diffusion I.1. In other words, the classical theorie of diffusion implies that the heat flux and temperature gradient occur simultaneously. For heat transfer in metals and semiconductors on small length and time scales this assumption is not correct, $\tau_q < \tau_T$.
- In the absence of a delay for the temperature gradient and a heat flux delay equal to the relaxation time of the heat transport mechanism, $\tau_T = 0$; $\tau_q = \tau_r$, equation (I.4) reduces to the thermal wave equation (I.2). According to the CV-wave model, the temperature gradient is always the cause ($\tau_T = 0 < \tau_q$) and the heat flux is always the effect. Because the temperature gradient delay is equal to zero ($\tau_T = 0$), this model is not appropriate for semiconductors and metals.
- The phonon scattering model (I.3) can be described, by equation (I.4), in case τ_q and τ_T are set to the following values.

$$\tau_T = \frac{9\tau_n}{5} \; ; \; \tau_q = \tau_r \; ; \; \tau_r = \frac{3\alpha}{c^2} \tag{I.5}$$

I.3 Temperature solutions for the different models

By making use of the results presented by Tzou [20], the behavior of classical diffusion, CV wave model and phase lag model is examined on a picosecond timescale. The pulse width of the heatsource used by Tzou, is even of the order femtoseconds. Although these timescales are much smaller compared to PIV-laserpulse cycle (O(nsec-msec)), it is interesting to depict the transient and spatial behavior between the different models.

I.3.1 Spatial temperature distribution

In figure I.1, is presented the spatial temperature solution at $t = 2\tau_q$ in a semi infinite solid after the left boundary [$\delta = 0$] is heated by a heatflux with a pulse width equal to $\frac{2}{5}\tau_q$. At the right boundary is prescribed a constant temperature equal to the initial temperature [T_0].

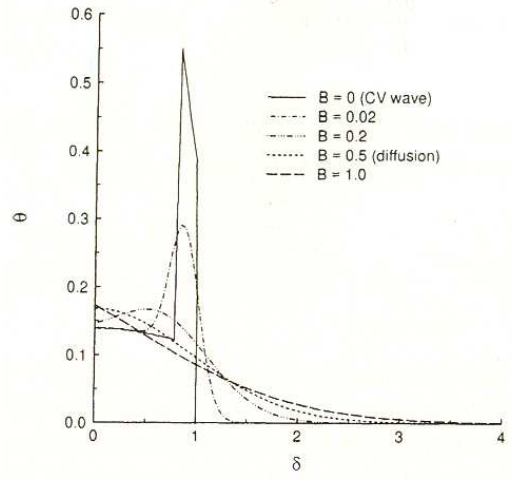

Figure I.1: Spatial distribution of lagging temperature in a semi infinite solid for B = 0 (CV wave), 0.02, 0.2, 0.5 (diffusion) and 1.0. The time, t, is equal to $2\tau_q$ and the laser pulse width is equal to $2/5\tau_q$. The solid is heated from the front, $\delta = 0$, by a heatflux.

The non dimensional parameter B, defined as $\frac{\tau_T}{2\tau_q}$, is varied to study the effect on the spatial temperature distribution. The dimensionless temperature [Θ] and dimensionless length [δ] are defined as:

$$\Theta(x,t) = \frac{T(x,t) - T_0}{T_0} \; ; \; \delta = \frac{x}{2\sqrt{\alpha\tau_q}}$$

For B equal to zero, which means equation (I.4) reduces to the CV model equation (I.2), a wave like temperature disturbance is predicted. When the value of B increases from zero, it's visible that the sharp and high temperature peak of the CV model reduces, due to the increasing presence of the mixed derivative term in equation (I.4). On the hand of the B-value for metals and semiconductors, which is $50 - 100$, it is sure that no wave like temperature disturbance propagates across the medium.

I.3.2 Transient temperature solutions

Tzou also evaluated the time response of equation (I.4), to variations of τ_T and τ_q. The mathematical solutions corresponding different values of τ_T and τ_q, are compared to experimental results presented by Qiu and Brorson.

1. In figure I.2 is presented the effect of τ_q and τ_T on the transient response of the reflectivity change (for definition reflectivity change, see y-axis of figure I.2).

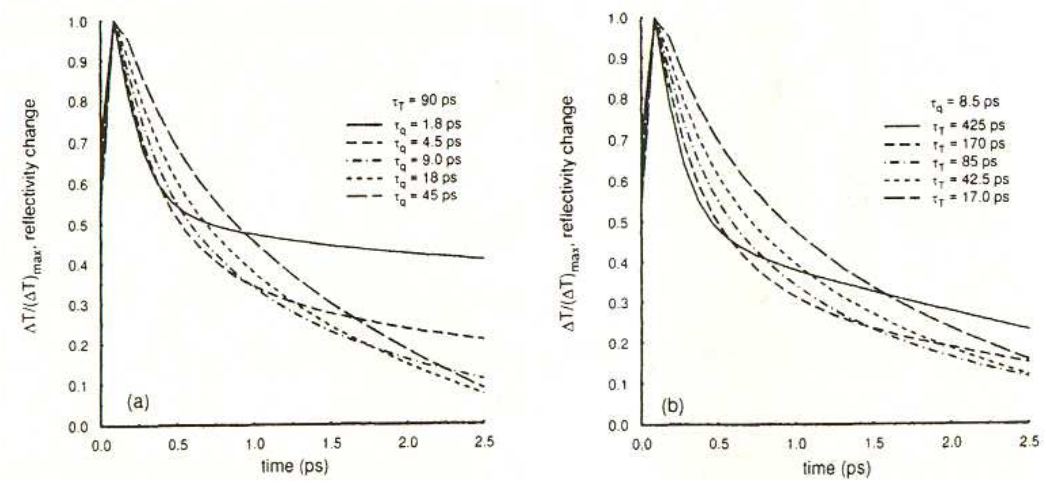

Figure I.2: Effect of (a) τ_q and (b) τ_T on the transient response of the reflectivity change

.

From the left figure (a) it is obvious that if τ_q increases while τ_t stays constant, that the temperature gradient increases during the first 0.5 picoseconds and that the temperature level later on declines. From the right figure (b) it's clear that if τ_t increases while τ_q stays constant, that the temperature gradient becomes more negative during the first 0.5 picoseconds and that the temperature level later on promotes.
This means that the ratio $\frac{\tau_q}{\tau_t}$, influences the temperature gradient during the first 0.5 seconds and the temperature level later on.

2. In figure I.3 is presented the transient response of reflectivity change under the same ratio of $\frac{\tau_T}{\tau_q}$.

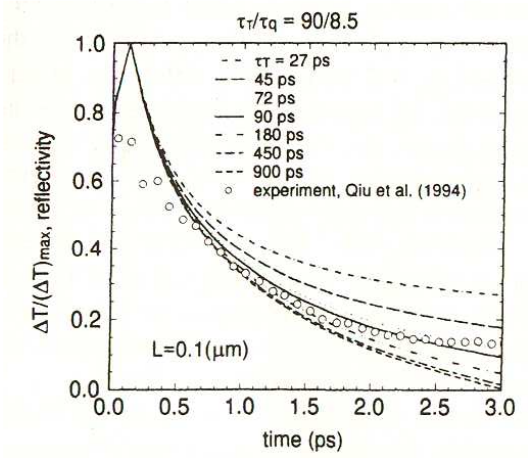

Figure I.3: Transient response of reflectivity change under the same ratio of $\frac{\tau_T}{\tau_q}$.

If the coefficient $\frac{\tau_T}{\tau_q}$ stays constant, and the value of τ_T and τ_q is raised with the same order, it's obvious from figure I.3 that the temperature level on longer times increases.

3. In figure is depicted the effect of τ_T and τ_q on the temperature response during the first 2.5 pico seconds.

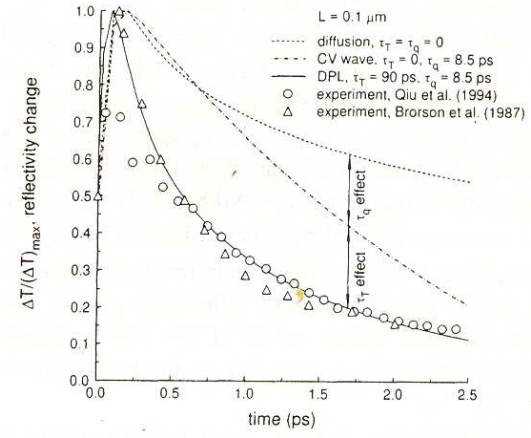

Figure I.4: Reflectivity change, comparison between the diffusion model, the CV wave model and the phase lagging model and the experimental results of Brorson and Qiu.

.

From figure I.4 it's clear that the diffusion model predicts the highest temperature during the first 2.5 picoseconds. If the delay of the heat flux is taken into account, which is the case for the CV wave model, the temperature distribution decreases for the first time towards the experimental measurements of Brorson and Qiu. Taking the temperature delay also in account, which is the case for the phase lagging model

(also phonon scattering model), results in a further temperature decrease towards the experimental determined values by Qui and Brorson.

I.4 Discussion

In the previous sections, the different models to describe heat transfer on macro and micro scales, are evaluated and compared to each other. The connection of the previous analysis with respect the to laserpulse cycle used to perform PIV can be summarized as:

- A wave like spatial temperature disturbance is not likely for metals and semiconductors with a typical B-value of 50-100, see figure I.1
- The size of the temperature peak during the femtosecond laserpulse, for the CV wave, diffusion and lagging model, are equal to each other. This means that the modelchoice only effects the cooling down period, after the medium is heated by the laserpulse.
- The temperature gradient during the first 0.5 picoseconds and temperature level later on, is influenced by the ratio $\frac{\tau_T}{\tau_q}$. The temperature level later on is beside the ratio $\frac{\tau_T}{\tau_q}$, also influended by the order of τ_q and τ_T. For silicon the ratio $\frac{\tau_T}{\tau_q}$, is of the order 10^2.
- Classical diffusion predicts the highest temperatures during the first picoseconds of the temperature respons to a heatflux pulse of the order femtoseconds. The CV wave model predicts temperatures closer the temperature measured by Brorson and Qiu. Temperatures predicted by the phase lagging model, match well with the experimental results of Brorson and Qiu.